# DEVELOPMENT OF A THREE-DIMENSIONAL EULERIAN MODEL OF DROPLET-WALL INTERACTION MECHANISMS

**Raimund Honsek**

Department of Mechanical Engineering

McGill University

Montreal, Québec

June, 2005

A Thesis Submitted to McGill University in

Partial Fulfillment of the Requirements of the Degree of Master of Engineering

*Your file Votre référence*
*ISBN: 978-0-494-22649-0*
*Our file Notre référence*
*ISBN: 978-0-494-22649-0*

# ABSTRACT

A wide variety of engineering applications involve the flow of particulate multiphase systems, featuring discrete liquid droplets dispersed in a continuous gas phase. Specific industrial examples range from fuel injection technologies over the optimization of multiphase segregation processes commonly encountered in petrochemical applications to aircraft in-flight icing control. A detailed understanding of dispersed phase characteristics such as local droplet velocity and volumetric fraction is required for design purposes and may be obtained from a numerical solution of the equations governing droplet motion.

A fundamental choice between Lagrangian and Eulerian reference frames presents itself in the formulation of the governing equations. While the physically intuitive Lagrangian approach treats the dispersed phase as a set of discrete particles that are individually tracked through the computational domain, the Eulerian formulation considers the dispersed phase as a continuum. The use of an Eulerian formulation to describe the evolution of discrete particles may appear counter-intuitive from a physical standpoint; however, advantages with respect to computational effort, numerical accuracy and accommodation of geometric complexity strongly suggest the use of an Eulerian formulation.

In order to accurately predict droplet behavior in the vicinity of a solid system boundary, droplet-wall interactions must be accounted for in the governing mathematical model. Due to current limitations in computational capacity, an industrially viable simulation is necessarily based on a semi-empirical description of the droplet-wall interaction process. Since empirical correlations are inherently Lagrangian in nature, the associated information must be transformed from a Lagrangian to an Eulerian frame of reference. This transformation, however, is not obvious and as a consequence no Eulerian impact models have been reported in the published scientific literature to date. A detailed derivation of an Eulerian model of the droplet-wall interaction process is presented along with a comparison of numerical and experimental results demonstrating the model's current simulation capabilities and suggested future improvements.

# RÉSUMÉ

Une vaste variété d'applications d'ingénierie implique des systèmes multiphasiques de particules, impliquant un nombre discret de gouttelettes liquides dispersées dans une phase gazeuse continue. Ces applications couvrent de la technologie d'injection de carburants, jusqu'à l'optimisation de procédés de ségrégation multiphasique d'applications pétrochimiques, en passant par le contrôle du givrage dans les avions en vol. Une connaissance détaillée des caractéristiques de la phase de dispersion, telles que la vitesse locale et la fraction volumétrique des gouttelettes, est nécessaire. Celles-ci peuvent être obtenues à partir d'une solution numérique des équations de l'écoulement de gouttelettes.

Un choix fondamental entre les repères lagrangien et eulérien doit être établi lors de la formulation des équations. L'approche lagrangienne traite la phase dispersée comme une série de particules discrètes qui sont tracées à travers le domaine. Quant à elle, la formulation eulérienne, considère la phase dispersée comme continue. L'utilisation d'une formulation eulérienne pourrait ne pas paraître physiquement intuitif, maisependant, ses avantages multiples vis-à-vis la formulation lagrangienne, notamment en terme de précision numérique et de potentiel pour géométries complexes suggèrent son utilisation.

Afin de prédire le comportement des gouttelettes dans le voisinage d'une frontière solide d'un système, les interactions gouttelette-paroi doivent être représentées dans le modèle mathématique. Une description semi-empirique de ces interactions est nécessaire pour une simulation industriellement viable. Les corrélations empiriques, de nature lagrangienne, suggèrent une transformation de l'information d'un repère lagrangien à un repère eulérien. Cette transformation n'est pas évidente puisque aucun modèle d'impact eulérien n'a pu être repéré dans la littérature scientifique publiée jusqu'à date. Cette Thèse propose donc une dérivation détaillée d'un modèle eulérien du procédé d'interaction gouttelette-paroi, une comparaison entre les résultats numériques et expérimentaux démontrant les capacités actuelles du modèle, ainsi que des suggestions pour améliorations futures.

# ACKNOWLEDGEMENTS

I would like to express my sincere gratitude to my thesis supervisor, Professor Wagdi G. Habashi, for his understanding mentorship and guidance and the opportunity to conduct challenging and rewarding research at McGill University's CFD Laboratory under his direction.

I am further indebted to Dr. François Morency and Dr. Claude Lepage for their many helpful discussions and encouraging suggestions regarding potential solution methodologies.

Many thanks are also due to my fellow colleagues at the CFD Laboratory, including Liang Kan Zheng, Farid Kachra, Peter Findlay, France Suerich-Gulick and Hongzhi Wang for creating and maintaining an amiable and thoroughly enjoyable as well as academically stimulating and productive working environment.

I would furthermore like to acknowledge the generous financial support of the National Sciences and Engineering Research Council of Canada in the form of an NSERC PGSA scholarship as well as a research grant provided under the NSERC J. Armand Bombardier Chair in Multi-Disciplinary CFD.

My sincerest thanks and appreciation go to Pablo H. Rousselin and Nabil Ben Abdallah for their dependable friendship and advice, for celebrating with me during good times and for carrying me through hardship, and most importantly for reminding me that there exists meaningful life outside of work.

Above all, I would like to thank my parents Siegfried and Gerda along with my siblings Christine, Gerlinde, Burkhard, Roland and Dietmar for their unconditional love and unwavering confidence in me, for supporting and encouraging me over all these years. I dedicate this thesis in their honour.

# TABLE OF CONTENTS

# LIST OF FIGURES

# LIST OF TABLES

# LIST OF SYMBOLS

## Latin Alphabet

| | | |
|---|---|---|
| $C_f$ | Skin Friction Coefficient | (-) |
| $d$ | Droplet Diameter | (μm) |
| $D_{max}$ | Maximum Spread Diameter | (μm) |
| $E_k$ | Kinetic Energy | (J) |
| $f$ | Impingement Frequency | (Hz) |
| $\vec{F}_B$ | Buoyancy Force | (N) |
| $\vec{F}_D$ | Drag Force | (N) |
| $\vec{F}_G$ | Gravitational Force | (N) |
| $\vec{F}_S$ | Splashing or Bouncing Force | (N) |
| $\vec{g}$ | Gravitational Acceleration Vector | ($m/s^2$) |
| $\hat{g}$ | Gravitational Acceleration Unit Vector | (-) |
| $H_n$ | Normalized Surface Normal Distance | (-) |
| $I_M$ | Impingement Module Activity | (-) |
| $(\hat{i},\hat{j},\hat{k})$ | Global Cartesian Unit Vectors | (-) |
| $L$ | Characteristic Length | (m) |
| $LWC$ | Liquid Water Content | ($kg/m^3$) |
| $m$ | Mass | (kg) |
| $\dot{m}$ | Mass Flux | (kg/s) |
| $(\hat{n},\hat{t}_1,\hat{t}_2)$ | Local Trajectoral Unit Vectors | (-) |
| $N$ | Number of Droplets | (-) |
| $N_R[n_1,n_2]$ | Random Number on $[n_1,n_2]$ | (-) |
| $p$ | Pressure | (Pa) |
| $P_i$ | Volumetric fraction of $i^{th}$ droplet size class | (-) |
| $\dot{Q}$ | Energy Flux | (W) |

| | | |
|---|---|---|
| $r$ | Surface Roughness | (μm) |
| $t$ | Normalized Time | (-) |
| $T_0$ | Freezing Point | (K) |
| $T_\infty$ | Free Stream Temperature | (K) |
| $\Delta T_S$ | Collision Contact Time | (-) |
| $\vec{u}_a$ | Normalized Air Velocity | (-) |
| $\vec{u}_d$ | Normalized Droplet Velocity | (-) |
| $\vec{u}_t$ | Normalized Terminal Velocity | (-) |
| $\vec{U}_\infty$ | Free Stream Velocity | (m/s) |
| $V$ | Volume | ($m^3$) |
| $(x, y, z)$ | Global Cartesian Coordinates | (m) |

## Greek Alphabet

| | | |
|---|---|---|
| $\alpha$ | Normalized Volume Fraction | (-) |
| $\Lambda$ | Volume Fraction | (-) |
| $\beta$ | Collection Efficiency | (-) |
| $\delta$ | Film Thickness | (μm) |
| $\phi$ | Surface Contact Angle | (°) |
| $\mu$ | Dynamic Viscosity | (Pa·s) |
| $\theta$ | Incidence Angle $\hat{n} \rightarrow \hat{t}_1$ | (°) |
| $\rho$ | Density | ($kg/m^3$) |
| $\sigma$ | Surface Tension | (N/m) |
| $\varphi$ | Azimuthal Angle $\hat{t}_1 \rightarrow \hat{t}_2$ | (°) |

## Dimensionless Groups

| | | |
|---|---|---|
| $C_D$ | Drag Coefficient | $C_D = \frac{8}{\pi} \frac{\left\|\vec{F}_D\right\|}{\rho_a U_\infty^2 \left\|\vec{u}_a - \vec{u}_d\right\|^2 d^2}$ |
| $C_P$ | Pressure Coefficient | $C_P = \frac{p - p_\infty}{\frac{1}{2}\rho_\infty U_\infty^2}$ |
| $Fr$ | Froude Number | $Fr = \frac{U_\infty}{\sqrt{Lg}}$ |
| $Ga$ | Galileo Number | $Ga = \frac{g\rho_a(\rho_d - \rho_a)d^3}{\mu_a^2} = \frac{3}{4} C_D \mathrm{Re}_d^2$ |
| $H$ | Film Thickness | $H = \frac{\delta}{d_o}$ |
| $K$ | Inertial Parameter | $K = \frac{\rho_d d^2 U_\infty}{18 L \mu_a}$ |
| $K_C$ | Cossali Parameter | $K_C = \left[\frac{\rho_d^6 d_o^6 u_{n,o}^{10} U_\infty^{10}}{\sigma^4 \mu_d^2}\right]^{\frac{1}{5}} = Oh^{-\frac{2}{5}} We_s$ |
| $K_M$ | Mundo Parameter | $K_M = \left[\frac{\rho_d^3 d_o^3 u_{n,o}^5 U_\infty^5}{\sigma^2 \mu_d}\right]^{\frac{1}{4}} = \left(Oh^{-\frac{2}{5}} We_s\right)^{\frac{5}{8}}$ |
| $K_Y$ | Yarin Parameter | $K_Y = u_{n,o} U_\infty \left[\left(\frac{\rho}{\sigma}\right)^2 \left(\frac{\mu}{\rho}\right)^{-1} f^{-3}\right]^{\frac{1}{8}}$ |
| $La$ | Laplace Number | $La = \frac{\rho_d \sigma d_o}{\mu_d^2}$ |
| $Oh$ | Ohnesorge Number | $Oh = \frac{\mu_d}{\sqrt{d_o \rho_d \sigma}}$ |

| | | |
|---|---|---|
| $R$ | Surface Roughness | $R = \frac{r}{d_o}$ |
| $Re_d$ | Droplet Reynolds Number | $\mathrm{Re}_d = \frac{\rho_a d U_\infty \lvert\vec{u}_a - \vec{u}_d\rvert}{\mu_a}$ |
| $Re_s$ | Impact Reynolds Number | $\mathrm{Re}_s = \frac{\rho_d d_o U_\infty u_{n,o}}{\mu_d}$ |
| $Re_t$ | Terminal Reynolds Number | $\mathrm{Re}_t = \frac{\rho_a d U_\infty \lvert\vec{u}_t\rvert}{\mu_a}$ |
| $S_c$ | Schmehl Parameter | $S_c = \frac{1}{24}\mathrm{Re}_s \, La^{-0.419}$ |
| $T$ | Total Breakup Time | $T = t' \frac{U_\infty \lvert\vec{u}_a - \vec{u}_d\rvert}{d} \sqrt{\frac{\rho_a}{\rho_d}}$ |
| $We_b$ | Breakup Weber Number | $We_b = \frac{\rho_a d U_\infty^2 \lvert\vec{u}_a - \vec{u}_d\rvert^2}{\sigma}$ |
| $We_s$ | Impact Weber Number | $We_s = \frac{\rho_d d_o U_\infty^2 u_{n,o}^{\ 2}}{\sigma}$ |

## Subscripts

| | | | |
|---|---|---|---|
| *a* | Air | *o* | Pre-Impact, Pre-Breakup |
| *c* | Critical | *rad* | Radiation |
| *con* | Convection | *s* | Post-Impact, Post-Breakup |
| *CV* | Control Volume | *stab* | Stable |
| *d* | Droplet | *t* | Tangential |
| *evap* | Evaporation | *tot* | Total |
| *ice* | Ice | *0* | Initial |
| *n* | Normal | ∞ | Free-stream |

# 1 INTRODUCTION

Aircraft lift and control surfaces exposed to meteorological conditions featuring liquid water content in the form of supercooled droplets at temperatures below the freezing point are subject to ice accretion and an inherent deterioration of performance characteristics. In order to demonstrate continued airworthiness during flight into known icing conditions, new aircraft have to comply with Appendix C of the Federal Aviation Administration (FAA) FAR 25 regulations, which defines the current envelope of meteorological conditions adopted by the FAA for icing certification of aircraft. The range of droplet sizes considered by Appendix C regulations is limited to droplet distributions featuring a mean volumetric diameter (MVD) of 40 μm as continuous maximum and 50 μm as intermittent maximum.

As a typical supercooled droplet impinges on an aircraft surface, it has the potential to freeze. Depending on liquid properties and surface temperatures as well as the surrounding aerodynamic flow field, the impinging droplet mass is either deposited at the impingement location in its entirety leading to the formation of rime ice, or a fraction of the impinging droplet mass moves downstream of the impingement location in the form of a shear-driven liquid film leading to the formation of glaze ice. While rime ice shapes are characterized by a relatively smooth profile approximating that of the clean airfoil, glaze ice shapes are defined by irregular ridges and horns, which lead to a significant degradation in the aerodynamic performance of iced lift and control surfaces. Figure 1-1 presents a schematic representation of these characteristic ice shapes and Figure 1-2 gives an indication of locations typically prone to accretion [1]. In order to control the ice accretion process on aircraft, active anti-icing measures comprised of chemical, mechanical or thermo-electrical devices are employed within the impingement limits of critical aircraft lift and control surfaces. An accurate prediction of these impingement limits as a function of aerodynamic and meteorological conditions, and especially the droplet distribution's mean volumetric diameter, thus becomes a necessity. As may easily be appreciated, the impingement limits move further downstream with increasing droplet MVD due to increasingly ballistic droplet trajectories. Hence, the traditional

design of anti-icing measures is based on the extreme impingement limits corresponding to the maximum droplet MVD of 40 μm outlined in Appendix C of the FAR 25 regulations.

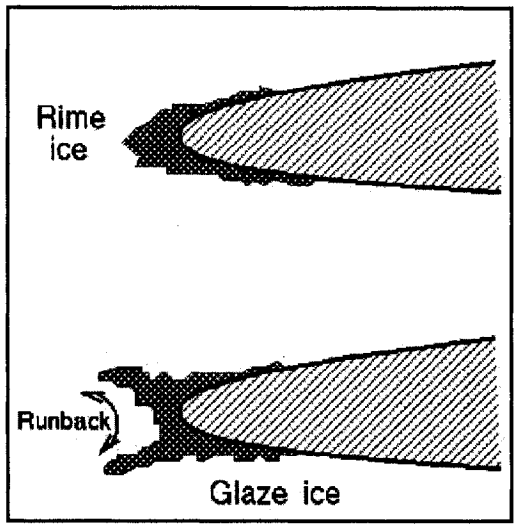


**Figure 1-1: Rime and Glaze Ice Shapes [1]**

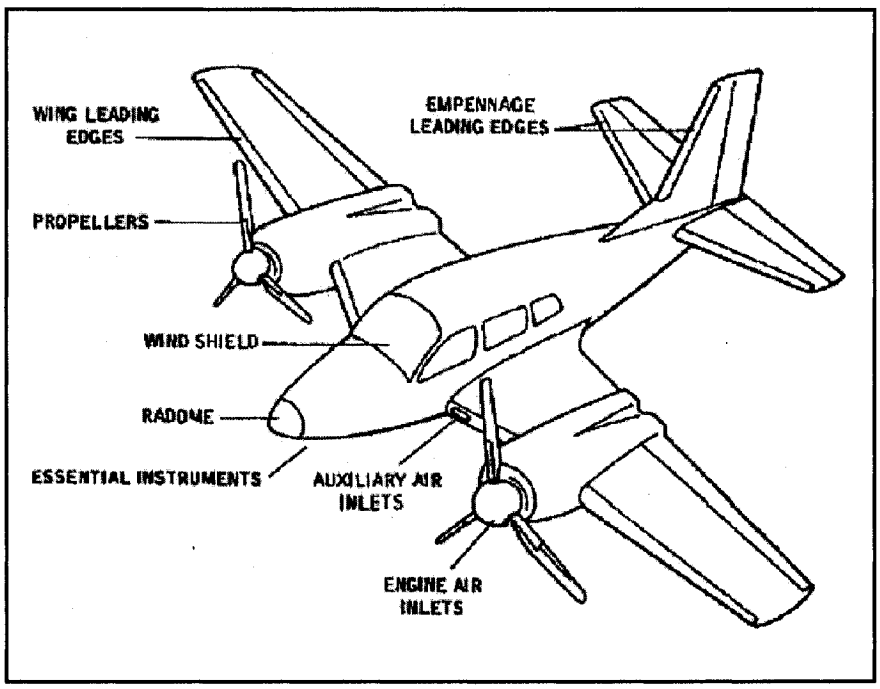


**Figure 1-2: Aircraft Lift and Control Surfaces Prone to Ice Accretion [1]**

However, in response to the icing-induced loss of control and subsequent crash of an ATR-72 commuter aircraft near Roselawn, Indiana on October 31, 1994, a renewed focus

on meteorological research has confirmed the existence of supercooled large droplets (SLD) featuring droplet MVDs up to 400 μm. Aircraft ice accretions due to SLD may result in extremely severe aircraft performance degradation, such as a reduction in stall angle accompanied by an increase in stall speed, a reduction in lift in excess of 60% and an increase in drag up to 200% as compared to the clean state in addition to the possibility of sudden aileron moment reversal. Furthermore, due to the large MVD of SLD droplets and their associated increasingly ballistic droplet trajectories, the corresponding ice accretions may be established downstream of the impingement regions protected by anti-icing measures, leading to an uncontrolled ice accretion process [2,3].

Clearly, the design of ice protection equipment based on the current maximum MVD of 40 μm specified in Appendix C of FAR 25 is insufficient and an extension of current ice accretion simulation techniques to include SLD droplet impingement is required. While principally feasible, such an extension is complicated by the fact that droplets in the SLD regime violate fundamental assumptions made in the development of both Lagrangian and Eulerian droplet impingement models regarding the physical impingement behavior of droplets within the envelope of Appendix C regulations. The most important of these violations pertain to the following simplifying assumptions:

- Droplets travel at the free stream velocity relative to the approaching airfoil
- Droplets maintain a spherical geometry along their impingement trajectories
- Droplets do not break up due to aerodynamic shear in the vicinity of the airfoil
- Droplets do not coalesce, bounce or splash upon impacting the airfoil

Due to their large MVD, SLD droplet distributions no longer enjoy the stable atmospheric stratification of droplet distributions within the Appendix C envelope but much rather resemble a droplet cloud falling at the terminal velocity corresponding to a given diameter. Hence, an additional vectorial component is introduced in the droplets' initial approach velocity, violating the assumption of an approach velocity equal to the free stream velocity and subsequently altering the resulting impingement trajectory [3-5].

Another effect of an increasing MVD is an increasing tendency for droplets to deform under the influence of aerodynamic shear forces, resulting in a decidedly non-spherical shape and hence increasing the effective drag over that corresponding to a spherical droplet. Furthermore, the effect of aerodynamic shear may become sufficiently manifest in the vicinity of aircraft surfaces to cause eventual droplet breakup resulting in a reduction of the droplet distribution's MVD prior to impingement. Both of these effects result in a more pronounced aerodynamic influence on droplet trajectories [3-5].

Depending on characteristic impingement surface conditions such as the non-dimensional surface roughness and surface film height and most importantly an approaching droplet's inertial component normal to the impingement surface, a droplet-wall collision may result in the complete or partial deposition of the impinging droplet mass in the form of an eventually freezing liquid film. For the case of droplet distributions featuring an MVD within the Appendix C envelope, an approaching droplet's inertia is sufficiently low to justify the assumption of negligible bouncing and splashing effects. However, empirical as well as computational studies have convincingly demonstrated the occurrence of droplet splash and rebound phenomena for droplet size distributions beyond the Appendix C limit. Under such circumstances, the approaching droplet mass is only partially deposited at the predicted impingement location, while the splashed or rebounded mass fractions are re-introduced into the flow field, potentially resulting in a net mass loss or more importantly leading to re-impingement on aircraft lift and control surfaces downstream of the actively protected impingement regions [5-8].

In order to address the aforementioned shortcomings of current numerical simulation capabilities within the SLD regime of droplet impingement, the contents of this thesis will demonstrate the formulation, calibration and validation of the necessary extensions of an existing three-dimensional Eulerian droplet impingement code, DROP3D$^{TM}$. A brief introduction to the current mathematical model will be presented, followed by the results of a rigorous review of published literature pertaining to droplet-wall interactions so as to establish a suitable context for the detailed derivation of a proposed mathematical model of droplet-wall interactions in an Eulerian frame of reference.

# 2 ORIGINAL MATHEMATICAL MODEL

The aim of any aircraft ice accretion simulation is to obtain an accurate prediction of the degradation of performance characteristics due to ice accretions resulting from a given combination of aerodynamic and meteorological operating conditions. A typical simulation may be decomposed into the following modules [1]:

- Prediction of the aerodynamic flow field surrounding an aircraft
- Prediction of the droplet impingement regions and local collection efficiencies
- Prediction of the corresponding ice accretion shapes on aircraft surfaces
- Prediction of the resulting degradation in aircraft performance characteristics

While this modular decomposition may lead to a degeneracy in numerical accuracy and computational efficiency in three-dimensional applications of common simulation codes such as the ONERA [9] and NASA LEWICE [10] codes, the above simulation modules are fully integrated in a three-dimensional, computational fluid dynamics (CFD) based in-flight icing methodology, FENSAP-ICE, within the scope of this thesis. As illustrated in Figure 2-1, the modules simulating airflow, droplet impingement and ice accretion interactively communicate the solutions of interdependent systems of partial differential equations formulated in an Eulerian frame of reference [1,11-15].

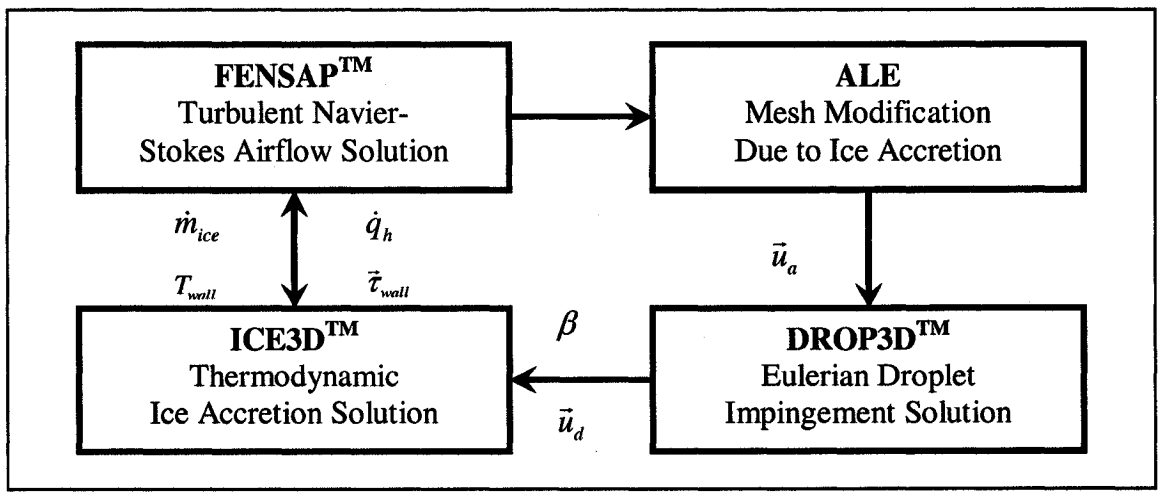


**Figure 2-1: Modular Simulation Methodology [1]**

## 2.1 Aerodynamics Module

FENSAP$^{TM}$ delivers the compressible, viscous aerodynamic flow field based on the solution of the Navier-Stokes equations in order to fully and directly account for the effects of three-dimensionality, turbulence and viscosity. These governing partial differential equations are discretized in space by means of a weak-Galerkin finite element method on structured as well as unstructured and hybrid grids, providing the geometric flexibility required for complex industrial applications. The resulting non-linear system of equations is iteratively solved by a Newton-generalized minimum residual (GMRES) algorithm.

Furthermore, the integrated Arbitrary Lagrangian-Eulerian (ALE) formulation in FENSAP$^{TM}$ allows for efficient and consistent modifications of the computational grid and a subsequent update of the aerodynamic flow field in order to account for surface augmentations due to the ice accretion process. As FENSAP$^{TM}$ is fully interfaced with an efficient anisotropic mesh adaptation module, OPTIMESH$^{TM}$, highly accurate user-, solver- and initial mesh-independent results may be obtained in two- and three-dimensional applications.

FENSAP$^{TM}$ facilitates the analysis of unsteady or steady compressible viscous flows featuring potential recirculation regions, while also providing the means for inviscid flow simulations if so desired. A similar flexibility exists with respect to dimensionality, as the solver's fully three-dimensional formulation provides the capability to simulate two- as well as three-dimensional flows [1,12,16].

As the ratio of bulk densities of the liquid and gas phases encountered in meteorological conditions representative of aircraft icing is of the order of $10^{-3}$, a one-way coupling of the two-phase flow is generally considered sufficient, hence the inertial effects of the droplets' presence on the airflow may be neglected and a modification of the Navier-Stokes equations is not necessary. This salient feature facilitates the use of dry flow solutions available from previous aerodynamic design efforts at the initial stage of the ice accretion simulation [17].

## 2.2 Droplet Impingement Module

A fundamental choice between Eulerian and Lagrangian reference frames presents itself in the derivation of the equations governing droplet motion. As the Lagrangian frame of reference may be considered attached to an individual droplet in motion, a description of a droplet's trajectory throughout the computational domain may be obtained by integration of its instantaneous velocity over time. An Eulerian frame of reference, however, treats the droplet phase as a continuum and considers the net flux of fluid through a fixed control volume rather than following the motion of a particular droplet. Hence, the Eulerian formulation provides information about average droplet properties at fixed points within the computational domain while the Lagrangian approach delivers individual droplet properties along an associated trajectory. As may be appreciated, both formulations exhibit strengths and weaknesses depending on a particular application.

In contrast to the Lagrangian formulation employed by traditional simulation systems such as the ONERA [9] and NASA LEWICE [10] ice accretion codes, DROP3D$^{TM}$ relies on a purely Eulerian model as the computation of the droplet impingement process by a Lagrangian approach introduces a numerical technique fundamentally different from the Eulerian formulation of the aerodynamic field solver, potentially resulting in the need for multiple grids. Furthermore, the Lagrangian tracking method requires a computationally intensive integration of droplet paths from the computational domain's inlet in order to determine if and where a particle may impact on an aircraft surface in an attempt to establish corresponding impingement limits.

For complex industrial geometries featuring intricate details as well as surfaces located in the aerodynamic shadow zones of other components, this tedious and somewhat ad-hoc approach requires the launching and tracking of a large number of individual droplets as the resolution of impingement limits is necessarily a function of the inter-droplet spacing. With respect to the computation of a local mass flux or collection efficiency distribution, the Lagrangian approach requires an averaging process based on previously computed

droplet impingement locations, which becomes difficult to define and implement for three-dimensional applications [9,11,12].

An Eulerian formulation, on the contrary, treats the dispersed liquid phase as a continuum, enabling the prediction of fully three-dimensional impingement limits and collection efficiency distributions in an automatic fashion at all locations within the computational domain, irrespective of geometric intricacies or aerodynamic interference patterns. The particular Eulerian formulation of the droplet impingement process employed by DROP3D$^{TM}$ yields a set of partial differential equations representing the continuity and momentum equations of the dispersed droplet phase.

These governing equations are spatially discretized according to a strong-Galerkin finite element formulation, which is fundamentally analogous to the spatial discretization scheme used in the aerodynamic field solver, thus facilitating the use of a single mesh for the simulation of both phases of the flow. Hence, droplet volume fractions and velocity components may be computed at the same nodes as the aerodynamic solution, avoiding the computationally intensive and interpolation based particle tracking process of the Lagrangian formulation [1,11-13].

While limited in computational elegance, the Lagrangian formulation lends itself well to the description of droplet-wall interaction processes. Droplet trajectories may be developed throughout the computational domain until a solid boundary is encountered at which point secondary droplet sizes and velocity components obtained from semi-empirical correlations may be imposed as initial conditions for the further time integration of droplet trajectories. However, as the notion of individual droplet trajectories no longer exists in an Eulerian formulation, an adequate mathematical description of the physical phenomena observed during droplet-wall collisions is not easily conceived. A detailed derivation of the equations governing droplet motion in the absence of droplet-wall interactions will be presented in an Eulerian reference frame in order to demonstrate the complexity associated with the formulation of an Eulerian description of an inherently Lagrangian process.

### 2.2.1 Simplifying Assumptions

The current mathematical formulation of DROP3D™ is based on the assumption that the droplets form a dispersed yet continuous medium, neglecting the following effects and phenomena for the sake of computational feasibility [1]:

- Inter-droplet collisions, coalescence and splashing upon impact
- Heat or mass exchange between the gas and liquid phases
- Aerodynamic turbulence effects on droplet surface properties

The negligence of inter-droplet collisions is inherently associated with a lack of a physical means of communication between droplets as the notion of pressure no longer exists. While this simplification is justifiable within most of the computational domain, the validity of this assumption becomes questionable in the vicinity of solid boundaries if the effects of droplet-wall collisions are to be taken into consideration.

### 2.2.2 Continuity Equation

Conservation principles stipulate that the total mass of liquid water contained in a given domain has to remain constant, yielding the well-known form of the continuity equation in an Eulerian frame of reference:

$$\frac{Dm_d}{Dt'} = \frac{\partial m_d}{\partial t'} + \nabla \cdot \left( m_d \vec{u}_d' \right) = 0 \tag{1}$$

An important parameter in the characterization of two-phase flows is the liquid water content (*LWC*) as it relates the volumetric proportions of the liquid and air phases, providing a measure of the dispersed liquid phase's bulk density. The *LWC* at a particular point may be defined as the mass of liquid water contained within a given two-phase fluid element per unit volume:

$$LWC = \frac{m_d}{V_{tot}} = \rho_d \frac{V_d}{V_{tot}} \tag{2}$$

Defining the quotient of the volume occupied by the liquid phase and the total volume of a given two-phase fluid element as the local volume fraction $\Lambda'$ of the droplet phase, the definition of *LWC* may be recast in the following form:

$$LWC = \frac{m_d}{V_{tot}} = \rho_d \Lambda' \tag{3}$$

The droplet continuity equation may be expressed in terms of *LWC* conservation by substituting Equations (2) and (3) into (1):

$$\frac{Dm_d}{Dt'} = \frac{\partial(V_{tot} LWC)}{\partial t'} + \nabla' \cdot (V_{tot} LWC \vec{u}_d') = \frac{\partial(V_{tot} \rho_d \Lambda')}{\partial t'} + \nabla' \cdot (V_{tot} \rho_d \Lambda' \vec{u}_d') = 0 \tag{4}$$

Considering that droplet density and total system volume remain constant, the droplet continuity equation may be reduced to the following form:

$$\frac{\partial \Lambda'}{\partial t'} + \nabla' \cdot (\Lambda' \vec{u}_d') = 0 \tag{5}$$

In order to non-dimensionalize Equation (5), the following relations are employed:

$$\Lambda = \frac{\Lambda'}{\Lambda_\infty'} = \Lambda' \left[ \frac{\rho_d}{LWC_\infty} \right] \qquad \vec{u} = \frac{\vec{u}'}{U_\infty} \qquad t = t' \left[ \frac{U_\infty}{L} \right] \qquad \nabla = \nabla' L \tag{6}$$

The droplet continuity equation may now be expressed in both non-dimensional and non-conservative form:

$$\frac{\partial \Lambda}{\partial t} \left[ \frac{\Lambda_\infty' U_\infty}{L} \right] + \nabla \cdot (\Lambda \vec{u}_d) \left[ \frac{\Lambda_\infty' U_\infty}{L} \right] = 0 \Rightarrow \frac{\partial \Lambda}{\partial t} + \vec{u}_d \cdot \nabla \Lambda + \Lambda (\nabla \cdot \vec{u}_d) = 0 \tag{7}$$

This form of the continuity equation lends itself to the use of a logarithmic formulation in order to ensure that the droplet volume fraction remains an always positive quantity:

$$\alpha = \ln \Lambda \Rightarrow e^\alpha \frac{\partial \alpha}{\partial t} + e^\alpha \vec{u}_d \cdot \nabla \alpha + e^\alpha (\nabla \cdot \vec{u}_d) = 0 \tag{8}$$

Following simplification, the droplet continuity equation may be recast in its final form [11,12]:

$$\frac{\partial \alpha}{\partial t} + \vec{u}_d \cdot \nabla \alpha + \nabla \cdot \vec{u}_d = 0 \tag{9}$$

## 2.2.3 Momentum Equations

Taking into account the aforementioned simplifying assumptions, the net force acting on a droplet is comprised of aerodynamic drag, in addition to gravity and buoyancy forces. A general expression for the aerodynamic drag may be made as a function of a non-dimensional drag coefficient $C_D$:

$$\vec{F}_D = \frac{1}{2}\rho_a u_r^2 A C_D = \frac{\pi}{8}\rho_a d^2 (\vec{u}_a' - \vec{u}_d')^2 C_D \tag{10}$$

Employing the definition of the droplet Reynolds number, the aerodynamic drag force may be recast as follows:

$$\vec{F}_D = \frac{\pi}{8}\mu_a d(\vec{u}_a' - \vec{u}_d')C_D \,\mathrm{Re}_d \tag{11}$$

Defining the magnitude of the buoyancy force acting on a droplet as the weight of the displaced volume of air, the effects of gravity and buoyancy may be expressed as follows:

$$\vec{F}_G = +m_d \vec{g} = +\frac{4}{3}\frac{\pi}{8} d^3 \rho_d \vec{g} \tag{12}$$

$$\vec{F}_B = -m_a \vec{g} = -\frac{4}{3}\frac{\pi}{8} d^3 \rho_a \vec{g} \tag{13}$$

Applying Newton's second law to a droplet in motion, the effect of aerodynamic drag, gravity and buoyancy forces on droplet trajectories may be evaluated:

$$m_d \frac{d\vec{u}_d'}{dt'} = \vec{F}_D + \vec{F}_G + \vec{F}_B \tag{14}$$

$$\frac{4}{3}\frac{\pi}{8} d^3 \rho_d \frac{d\vec{u}_d'}{dt'} = \frac{\pi}{8}\mu_a d(\vec{u}_a' - \vec{u}_d')C_D \,\mathrm{Re}_d + \frac{4}{3}\frac{\pi}{8} d^3 \rho_d \vec{g} - \frac{4}{3}\frac{\pi}{8} d^3 \rho_a \vec{g} \tag{15}$$

Employing the definition of the non-dimensional droplet inertia parameter $K$, the above expression may be reduced to the following form:

$$\frac{d\vec{u}_d'}{dt'} = \frac{C_D \mathrm{Re}_d}{24K}(\vec{u}_a' - \vec{u}_d')\frac{U_\infty}{L} + \left(1 - \frac{\rho_a}{\rho_d}\right)\vec{g} \tag{16}$$

In order to obtain an equivalent expression corresponding to an Eulerian formulation, the simple time derivative *d/dt* in Equation (16) is replaced by the substantial derivative *D/Dt*:

$$\frac{D\vec{u}_d'}{Dt'} = \frac{\partial \vec{u}_d'}{\partial t'} + \vec{u}_d' \cdot \nabla' \vec{u}_d' \tag{17}$$

Application of (17) along with the non-dimensionalization relations (6), yields the non-dimensional form of the droplet continuity equation in a Eulerian frame of reference:

$$\frac{D\vec{u}_d'}{Dt'} = \left[\frac{d\vec{u}_d}{dt} + \vec{u}_d \cdot \nabla \vec{u}_d\right]\left[\frac{U_\infty^2}{L}\right] = \left[\frac{C_D \mathrm{Re}_d}{24K}(\vec{u}_a - \vec{u}_d) + \left(1 - \frac{\rho_a}{\rho_d}\right)\frac{\vec{g}L}{U_\infty^2}\right]\left[\frac{U_\infty^2}{L}\right] \tag{18}$$

Simplifying the resulting expression and employing the definition of the Froude number $Fr$, the droplet momentum equations may be recast in their final form [11,12]:

$$\frac{D\vec{u}_d}{Dt} = \frac{\partial \vec{u}_d}{\partial t} + \vec{u}_d \cdot \nabla \vec{u}_d = \frac{C_D \mathrm{Re}_d}{24K}(\vec{u}_a - \vec{u}_d) + \left(1 - \frac{\rho_a}{\rho_d}\right)\frac{\hat{g}}{Fr^2} \tag{19}$$

## 2.2.4 Spatial Discretization

The spatial discretization of the continuity (9) and momentum equations (19) is accomplished by means of a strong-Galerkin finite element formulation. In this methodology, given a mesh over a computational domain $\Omega$ and a space $V_h$ of piecewise continuous linear functions, the volume fraction $\alpha^n \in V_h$ and the droplet velocity $u^n \in V_h^3$ at time $t^n$ are discrete solutions of Equations (20) and (21), respectively, for all $\varphi \in V_h$ and $\psi \in V_h^3$. In the following relations, $\vec{f}$ represents the forcing terms of the

momentum equations such as drag, gravity and buoyancy forces and thus depends on the air and droplet velocity field.

$$\int_{\Omega}\left[\frac{\alpha^n-\alpha^{n-1}}{\Delta t}+\nabla\cdot\left(\alpha^n\vec{u}^n\right)\right]\varphi dx+a_\alpha\left(\alpha^n,\varphi\right)=0 \tag{20}$$

$$\int_{\Omega}\left[\frac{\vec{u}^n-\vec{u}^{n-1}}{\Delta t}+\vec{u}^n\cdot\nabla\vec{u}^n\right]\cdot\psi dx+a_u\left(u^n,\psi\right)=\int_{\Omega}\vec{f}\cdot\psi dx \tag{21}$$

The terms $a_\alpha(\alpha,\varphi)$ and $a_u(u,\psi)$ represent streamline upwind Petrov-Galerkin (SUPG) stabilization terms, which are added to damp potential oscillations in the numerical solution of the governing partial differential equations and defined as follows:

$$a_\alpha(\alpha,\varphi)=c_\alpha\sum_k\int_k\left[\frac{\alpha^n-\alpha^{n-1}}{\Delta t}+\nabla\cdot\left(\alpha^n\vec{u}^n\right)\right]\tau_k\left(\vec{u}^n\cdot\nabla\right)\varphi dx \tag{22}$$

$$a_u(u,\psi)=c_u\sum_k\int_k\left[\frac{\vec{u}^n-\vec{u}^{n-1}}{\Delta t}+\vec{u}^n\cdot\nabla\vec{u}^n-\vec{f}\right]\tau_k\left(\vec{u}^n\cdot\nabla\right)\psi dx \tag{23}$$

$$\tau_k=h_k\Big/\sqrt{1+|\vec{u}|^2} \tag{24}$$

The parameter $h_k$ represents the minimal size of element $k$, while $c_\alpha$ and $c_u$ represent problem specific stabilization coefficients chosen by the user. Due to the highly non-linear nature of the Eulerian droplet convection model, the solution of the droplet volume fraction predominantly requires SUPG stabilization. Hence, $c_u$ is generally chosen within the range [0.1, 10] while $c_\alpha$ is chosen within the range [1, 100] for typical droplet impingement simulations [11,12].

## 2.2.5 Boundary Conditions

A detailed analysis of system characteristics performed by Bourgault [11] reveals that Dirichlet boundary conditions are required for both the droplet volume fraction and velocity components at the inflow boundary of the computational domain, while no specification of boundary conditions is required at solid system boundaries or outflow boundaries of the computational domain in order to uniquely determine the solution of the governing equations. Inflow and outflow boundaries associated with incoming and outgoing characteristics are respectively denoted by $\Gamma_+$ and $\Gamma_-$ in Figure 2-2.

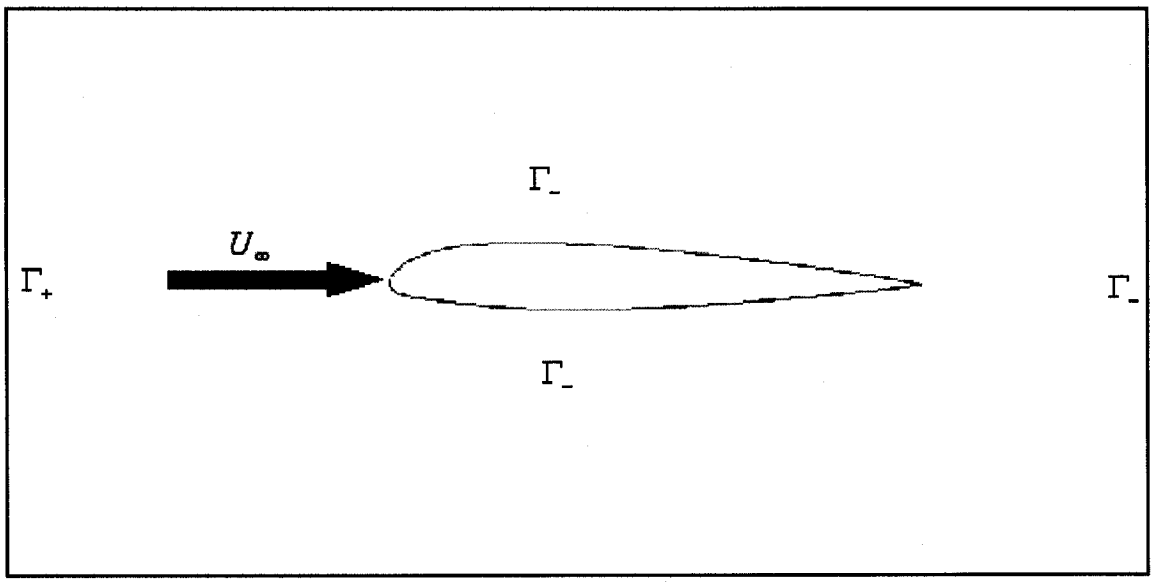


**Figure 2-2: Inflow and Outflow Boundaries of Computational Domain [11]**

A suitable initial solution respecting these boundary condition requirements is to set $\alpha = 1$ and $\vec{u}_d = [\cos(AoA), \sin(AoA), 0]$ throughout the computational domain. An exception applies to locations within the immediate vicinity of solid system boundaries where both the droplet volume fraction and velocity are initially set to zero as the velocity field of the gas phase satisfies the no slip condition inherent with the solution of the Navier–Stokes equations at solid surfaces [1,11].

## 2.2.6 Droplet Drag Coefficient

A commonly used empirical expression for the variation of the drag coefficient with the droplet Reynolds number is based on the measured drag on a spherical particle subject to a uniform flow field [18]:

$$C_D = \begin{cases} \frac{24}{\mathrm{Re}_d}\left(1+0.15\mathrm{Re}_d^{0.687}\right) & \mathrm{Re}_d \le 1300 \\ 0.40 & \mathrm{Re}_d > 1300 \end{cases} \tag{25}$$

However, droplets featuring a large diameter are prone to deformation under the influence of aerodynamic pressure forces, resulting in a decidedly non-spherical shape and hence increasing the effective drag coefficient over that given by Equation (25). In order to account for this increase in aerodynamic drag at SLD conditions, an extended drag model based on droplet eccentricity and vibrational distortion is employed [19]:

$$C_D = \begin{cases} (1.0-f)C_D' + fC_D'' & We_b \le 12 \\ C_D' & We_b > 12 \end{cases} \tag{26}$$

The eccentricity function $f$ is defined as a function of the breakup Weber number:

$$f = 1.0 - \left(1.0 + 0.07\sqrt{We_b}\right)^{-6} \tag{27}$$

The parameters $C_D'$ and $C_D''$ correspond to the drag coefficients of an oblate disk and a spherical particle, respectively. Hence, the effective drag coefficient of Equation (26) will approach that of a spherical particle at low Weber numbers while tending towards that of an oblate disk at elevated Weber numbers.

## 2.2.7 Droplet Breakup

Droplets may experience vibrational distortion eventually leading to acceleration-induced breakup under the influence of sufficiently pronounced aerodynamic shear. Five distinct breakup mechanisms are characterized by the initial droplet Weber number and the associated non-dimensional breakup time $T$ and may be identified as follows [20]:

$$T = \begin{Bmatrix} 6.000(We_b - 12)^{-0.25} & 1.2e+1 \le We_b \le 1.8e+1 \\ 2.450(We_b - 12)^{+0.25} & 1.8e+1 \le We_b \le 4.5e+1 \\ 14.10(We_b - 12)^{-0.25} & 4.5e+1 \le We_b \le 3.5e+2 \\ 0.766(We_b - 12)^{+0.25} & 3.5e+2 \le We_b \le 2.7e+3 \\ 5.500 & 2.7e+3 \le We_b \end{Bmatrix} \tag{28}$$

Based on the assumption that post-breakup droplet fragments eventually acquire sub-critical Weber numbers, the maximum stable droplet diameter at cessation of all breakup activities is based on the definition of the critical droplet breakup Weber number:

$$We_{b,crit} = 12 \Rightarrow d_{stab} = \frac{12\sigma}{\rho_a U_\infty^2 |\vec{u}_a - \vec{u}_d|^2} \tag{29}$$

The evolution of the local value of the droplet diameter under the influence of droplet breakup due to aerodynamic shear is thus governed by the following partial differential equation as proposed by Lodej [21]:

$$\frac{Dd}{Dt} = \frac{\partial d}{\partial t} + \vec{u}_d \cdot \nabla d = \frac{d_{stab} - d_o}{T} \tag{30}$$

## 2.2.8 Collection Efficiency

A non-dimensional parameter of interest that quantifies a given location's ice accretion potential is the local collection efficiency $\beta$, which represents the normalized influx of water at a solid boundary whose surface normal $\hat{n}$ is defined to point way from the surface and hence into the computational domain:

$$\beta = \left(\frac{\dot{m}_d}{A}\right) \Big/ \left(\frac{\dot{m}_d}{A}\right)_\infty = \frac{u_n' LWC}{U_\infty LWC_\infty} = -\frac{(\vec{u}_d' \cdot \hat{n})\Lambda' \rho_d}{U_\infty \Lambda_\infty' \rho_d} = -\left(\frac{\vec{u}_d'}{U_\infty} \cdot \hat{n}\right)\frac{\Lambda'}{\Lambda_\infty'} \tag{31}$$

Applying the normalization relations (6) to Equation (31), the local collection efficiency may be expressed in terms of the non-dimensional droplet volume fraction and droplet velocity [11,12]:

$$\beta = -\alpha \vec{u}_d \cdot \hat{n} \tag{32}$$

The dimensional expression for the water flux per unit surface may thus be recast as a function of the local collection efficiency:

$$\frac{\dot{m}_d}{A} = LWC_\infty U_\infty \beta \tag{33}$$

The system of Equations (9) and (19) models the evolution of mono-dispersed droplet size distributions featuring a common diameter. Hence, the co-existence of multiple classes of droplet diameters, commonly referred to as bins, in a typically multi-dispersed droplet size distribution must be accounted for by separately modeling the evolution of a given class of droplets and subsequently superimposing the individual simulation results. Thus, if the volumetric fraction of droplets in the $i^{th}$ class is taken as $P_i$, the amalgamated local collection efficiency may be obtained from a corresponding weighted summation over all droplet classes:

$$\beta = \sum_i P_i \beta_i \tag{34}$$

## 2.3 Ice Accretion Module

The three-dimensional simulation of the ice accretion process is performed by ICE3D™ based on the impingement locations and the associated distribution of the local collection efficiency as determined by DROP3D™ along with the aerodynamic flow field predicted by FENSAP™. The governing thermodynamic model accounts for energy and mass transfer at the solid/liquid/vapour interfaces and includes the relevant physics necessary to accurately model the formation of rime, glaze and mixed ice shapes.

The formation of the various types of ice accretions is predominantly governed by the local convective heat transfer and described by a set of partial differential equations based on the traditional Messinger [22] formulation, satisfying the first law of thermodynamics as applied to the conservation of mass and energy in a given control volume. The resulting Shallow Water Icing Model (SWIM) closely resembles the

shallow-water equations, modified to account for the simultaneous co-existence of solid, liquid and vapour phases [1,13-15].

As may be appreciated from an inspection of Equation (35), the mass of liquid water contained within a given control volume at a solid boundary is directly affected by the net flux of water droplets normal to the boundary. Furthermore, Equation (36) demonstrates that the net flux of water droplets is purely determined by the distribution of local collection efficiencies along the boundary as the free-stream values of velocity and liquid water content remain constant:

$$\dot{m}_{CV} = \dot{m}_d + \dot{m}_{evap} + \dot{m}_{ice} \tag{35}$$

$$\dot{m}_d = U_\infty LWC_\infty \int_A \beta(x,y,z,t)dxdydz \tag{36}$$

The strong dependence of an ice accretion simulation's accuracy on droplet impingement velocities in addition to the distribution of local collection efficiencies may be emphasized further by an investigation of the relations governing the conservation of energy within the control volume:

$$\dot{Q}_{CV} = \dot{Q}_d + \dot{Q}_{evap} + \dot{Q}_{ice} + \dot{Q}_{con} + \dot{Q}_{rad} \tag{37}$$

$$\dot{Q}_d = U_\infty LWC_\infty \int_A \beta(x,y,z,t)\left[ c_p(T_\infty - T_0) + \frac{|\vec{u}_d(x,y,z,t)|^2}{2} \right] dxdydz \tag{38}$$

Therefore, physically meaningful simulations of ice accretion processes under SLD conditions must necessarily be based on local collection efficiency distributions and droplet impingement velocities that are augmented to account for the effects of droplet-wall collisions. Previous attempts by Boulahya [23] to achieve this augmentation through mere post-processing of local collection efficiencies obtained in the absence of droplet-wall collisions may hence be considered insufficient, as this approach fails to address the effects of droplet-wall collisions on impingement velocities and resulting trajectories in the vicinity of solid boundaries.

# 3 LITERATURE REVIEW

As mentioned in the introduction to this thesis, the droplet impingement module's current mathematical formulation fails to account for the unique approach and impingement characteristics associated with droplets within the SLD regime, such as the initially terminal droplet velocity as well as droplet splash and rebound phenomena upon impact. In order to address these issues within the mathematical formulation of DROP3D$^{TM}$, a corresponding modification of the forcing terms in the equations governing momentum must be formulated and implemented. Thus, the results of a detailed review of published literature pertaining to dispersed liquid-gas flows and droplet-wall interactions reported in a variety of engineering applications will be presented in order to justify the particular mathematical formulation adopted in the course of this thesis.

## 3.1 Terminal Droplet Velocity

Due to their large diameter, SLD droplets no longer enjoy the stable atmospheric stratification of droplets within the Appendix C envelope but much rather resemble a droplet cloud falling at the terminal velocity corresponding to a given diameter. As the unknown droplet velocity appears in both the drag coefficient and the droplet Reynolds number, there is a general difficulty in establishing correlations expressing a droplet's terminal velocity in terms of the corresponding Reynolds number. Hence, a dimensionless group known as the Galileo number may be defined as a function of physical properties of the gas and liquid phase in order to eliminate the unknown terminal velocity. Khan and Richardson [24] derive a correlation expressing the Reynolds number over the range of $1.0e-2 \leq \mathrm{Re}_t \leq 3.0e+5$ as a function of the Galileo number:

$$\mathrm{Re}_t = \left(2.33Ga^{0.018} - 1.53Ga^{-0.016}\right)^{13.3} \tag{39}$$

Once the Reynolds number is evaluated, the corresponding terminal velocity may be obtained from the definition of the terminal Reynolds number:

$$\vec{u}_t = \frac{\mu_a}{\rho_a d U_\infty}\left(2.33Ga^{0.018} - 1.53Ga^{-0.016}\right)^{13.3} \tag{40}$$

## 3.2 Droplet-Wall Interactions

The three-dimensional fluid flow resulting from droplet-wall interactions may be extremely complex as it is influenced by a variety of factors including the surrounding aerodynamic flow field, the initial droplet characteristics as well as impact surface conditions. According to a comprehensive qualitative review of droplet impact phenomena by Rein [25], a droplet impacting on a surface may coalesce with a potentially existing surface water film, rebound off the impact surface without significant distortion or disintegrate into secondary droplet fragments in a splashing event. At sufficiently large impact energies, the impact of a drop on a surface covered by a liquid film may lead to the formation of a crater and the subsequent lateral ejection of a liquid sheet. While such liquid sheets may close over the impact crater leading to the entrainment of air and hence formation of bubbles, most liquid sheets tend to disintegrate due to vibrational surface instabilities, leading to the formation of a crown of secondary droplet fragments along the periphery of the sheet as illustrated in Figure 3-1.

**Figure 3-1: Droplet Impact Leading to Splash or Rebound**

### 3.2.1 Impact Regimes and Mechanisms

While generally deemed to be insufficiently efficient for the simulation of large scale multiphase flows, a detailed knowledge of single droplet impingement phenomena proves valuable in assessing the potential range of droplet-wall interaction mechanisms which may occur within the operational envelope of a particular industrial application. Bai and

Gosman [26] identify 7 discrete regimes of droplet impingement, each of which is characterized by a specific interaction mechanism:

- **Regime 1:** At sufficiently low impact velocities and surface temperatures, the impinging droplet sticks to the impact surface in approximately spherical form.
- **Regime 2:** At low impact velocities a film of air may be entrained between the impinging droplet and a wetted impact surface, causing the droplet to rebound off the surface following impact.
- **Regime 3:** At moderate impact velocities, the impinging droplet forms a liquid film on a dry impact surface or coalesces with the existing film on a wetted impact surface.
- **Regime 4:** At sufficiently high impact velocities, a liquid sheet is ejected from the impact surface, leading to the development of a crown and subsequent formation of droplet fragments along its periphery.
- **Regime 5:** At low impact velocities and sufficiently high impact surface temperatures, the impinging droplet rebounds off the surface following impact and disintegrates into several large fragments.
- **Regime 6:** At low impact velocities and sufficiently high impact surface temperatures, the impinging droplet disintegrates due to rapid boiling on the impact surface.
- **Regime 7:** At moderate impact velocities and sufficiently high surface temperatures, the impinging droplet forms a radial liquid film on the surface that is subsequently fragmented due to thermo-induced instabilities.

The mechanisms associated with Regimes 5 through 7 exclusively occur at impact surface temperatures in excess of the impinging droplet's boiling temperature and hence

are of no relevance to the simulation of droplet impingement on aircraft surfaces in icing conditions. The particular mechanisms of droplet-wall interactions pertaining to the operational envelope of aircraft ice accretion thus include stick, rebound, spread and splash mechanisms which are illustrated schematically in Figure 3-2.

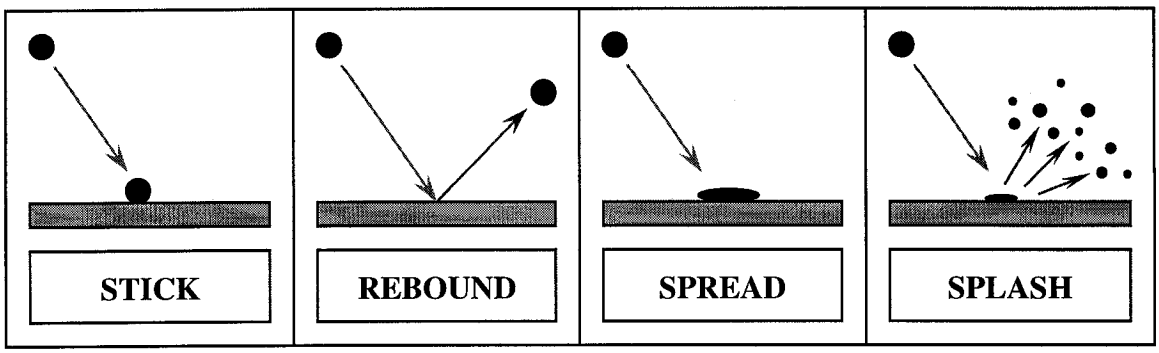


**Figure 3-2: Schematic Representation of Pertinent Droplet-Wall Interaction Mechanisms**

The transition between these characteristic mechanisms of droplet-wall interactions is largely a function of kinematic properties such as droplet impact velocity, size, shape and incidence angle, as well as thermodynamic droplet properties such as temperature, surface tension and viscosity. Furthermore, impact surface conditions such as surface roughness and curvature, as well as the height of a potentially existing liquid film, exhibit a large influence on the particular mechanism of a droplet-wall interaction. A number of dimensionless groups governing droplet-wall interactions may thus be identified, including the droplet impact Weber number $We_s$, as well as the normalized surface roughness $R$ and film thickness $H$. Experimental investigations have demonstrated that a droplet impinging on a wetted surface will undergo the interaction mechanisms of Figure 3-2 in the illustrated order as the impact Weber number is increased.

## 3.2.2 Semi-Empirical Modeling Requirements

As may be appreciated, the general mechanisms of droplet-wall interactions are governed by a large number of physical parameters, yet it is feasible to develop highly accurate numerical models of a single droplet impact by Volume of Fluid (VOF) methods such as the one proposed by Bussman, Chandra, and Mostaghimi [27]. However, due to their

inherently Lagrangian formulation, VOF methods become prohibitively expensive if applied to the simulation of dispersed multiphase flows as discrete droplets must necessarily be treated as computational sub-domains and hence individually meshed. Therefore, an industrially viable computational model of droplet-wall interactions must be based on a semi-empirical formulation of the droplet impingement process. In order to facilitate the simulation of droplet-wall interactions, a given semi-empirical impact model needs to satisfy several requirements:

- A regime transition criterion is required to enable the prediction of the particular interaction mechanism applicable to a given operating condition as a function of impinging droplet properties and surface characteristics.

- In the case of the rebound and splashing mechanisms, the prediction of post-impact droplet velocity components is required as a function of the incident droplet velocity.

- In the case of the splashing mechanism, the prediction of splashed and deposited mass fractions is required as a function of the incident droplet mass in addition to an estimate of secondary droplet sizes.

- The impact model must be applicable within the range of droplet sizes and impact velocities observed in aircraft icing at SLD conditions.

In order to enable an unambiguous definition of pertinent model parameters, Figure 3-3 illustrates physical droplet characteristics within the context of a typical droplet-wall interaction. Please note that the local $(\hat{n},\hat{t}_1,\hat{t}_2)$ coordinate system is defined along a given droplet's impingement trajectory. As merely the stick and spread mechanisms of droplet impact are accounted for in the current mathematical formulation of DROP3D$^{TM}$, semi-empirical impact models are required for the rebound and splashing mechanisms. A variety of pertinent droplet impact models exist in the literature, the most relevant of which will be introduced in the following sections and discussed with respect to physical comprehensiveness and applicability in SLD conditions.

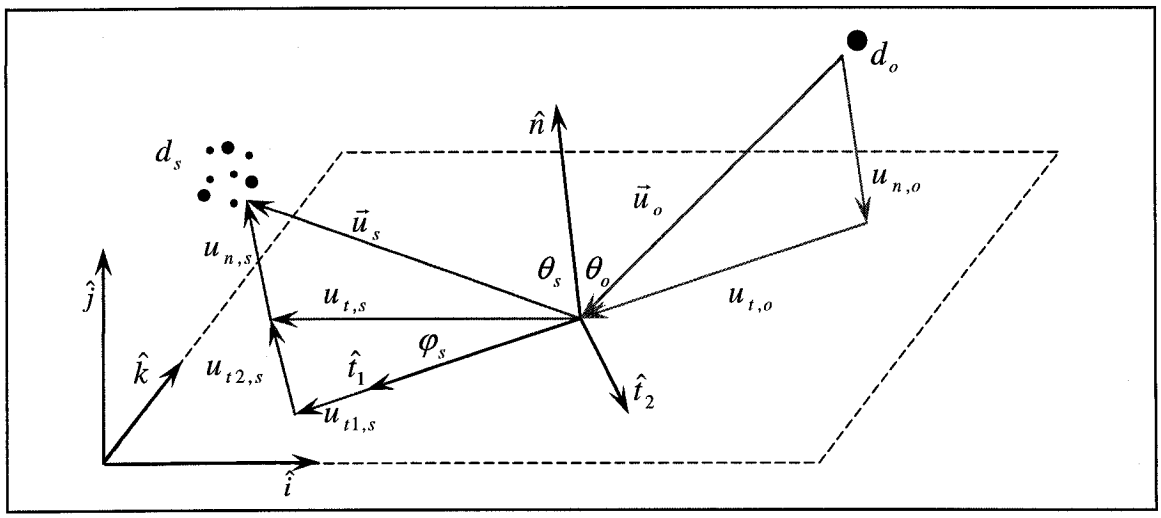


**Figure 3-3: Pertinent Model Parameters**

## 3.2.3 Jayaratne and Mason Impingement Model

One of the first dissertations on the phenomena of droplets rebounding off a liquid surface may be attributed to Jayaratne and Mason [28] who proposed an empirical relation between the kinetic energy loss during rebound and the droplet's incidence angle:

$$|\vec{u}_s| = |\vec{u}_o|\sqrt{1.00 - 0.95\cos^2(\theta_o)} \tag{41}$$

However, the depth of the liquid film considered in the corresponding experiment is significantly larger than that typically encountered on aircraft surfaces and hence the loss of kinetic energy may be considerably over-predicted in such applications.

## 3.2.4 Naber and Reitz Impingement Model

An early droplet impingement model proposed by Naber and Reitz [29] considers three potential interaction mechanisms consisting of complete droplet deposition, rebound or outflow, a basic flow structure analogous to a jet propagating tangentially along a given impact surface. In the case of droplet rebound, the tangential velocity component is assumed to remain constant while the normal velocity component is reversed without incurring any loss of kinetic energy:

$$u_{t,s} = u_{t,o} \tag{42}$$

$$u_{n,s} = -u_{n,o} \tag{43}$$

The assumption of conservation of kinetic energy is also applied to an impinging droplet experiencing outflow conditions following impact:

$$u_{t,s} = \sqrt{u_{t,o}^2 + u_{n,o}^2} \tag{44}$$

$$u_{n,s} = 0 \tag{45}$$

This model does not account for the partial deposition of the impinging droplet mass, the formation of droplet fragments due to splashing and any kinetic energy losses due to impact in addition to an apparent lack of clearly defined regime transition criteria and hence this mathematical model is considered overly simplistic and insufficiently detailed for the desired application.

## 3.2.5 Wang and Watkins Impingement Model

In an attempt to remedy some of the more severe shortcomings of the Naber and Reitz [29] model, Wang and Watkins [30] extend the original model to include the loss of kinetic energy incurred during impact as proposed by Jayaratne and Mason [28] as well as a simple regime transition criterion based on the droplet impact Weber number. The mechanism of droplet rebound is thought to be applicable at impact Weber numbers below 80, while the mechanism of jet flow is applied to collisions featuring Weber numbers in excess of that value:

$$u_{t,s} = \begin{Bmatrix} u_{t,o}\sqrt{1.00 - 0.95\cos^2(\theta_o)} & We_s < 80 \\ u_{t,o} & We_s > 80 \end{Bmatrix} \tag{46}$$

$$u_{n,s} = \begin{Bmatrix} -u_{n,o}\sqrt{1.00 - 0.95\cos^2(\theta_o)} & We_s < 80 \\ 0 & We_s > 80 \end{Bmatrix} \tag{47}$$

Furthermore, potential fragmentation of the tangentially propagating jet flow is considered by the modified empirical model:

$$d_s = \frac{1}{4} d_o \tag{48}$$

$$N_s = 64 \tag{49}$$

While Wang and Watkins [30] define a regime transition criterion and introduce kinetic energy losses, the resulting model does not account for impact surface conditions such as surface roughness and liquid film depth and even though droplet fragmentation is considered, the secondary droplet fragments are limited to a purely tangential propagation direction along the impact surface. Hence, the extension of the original Naber and Reitz [29] model as provided by Wang and Watkins [30] is still considered insufficiently detailed to satisfy the physical requirements of the intended application.

### 3.2.6 Bai and Gosman Impingement Model

The droplet-wall interaction model proposed by Bai and Gosman [26] is considerably more physically comprehensive than previous models as it considers both droplet rebound and splash mechanisms in addition to defining regime transition criteria based on droplet properties in the form of a critical Weber number as well as surface properties in the form of an empirical surface roughness dependent coefficient:

$$We_{s,c} = A(r) La^{-0.18} \tag{50}$$

In the case of an impact surface covered by a thin liquid film, the transition between droplet rebound and spreading regimes occurs at a critical Weber number of $We_{s,c} = 5$ while the transition between spreading and splashing regimes is based on a roughness dependent coefficient of $A(r) = 1320$.

Bai and Gosman reiterate the potential inapplicability of the droplet rebound model developed by Jayaratne and Mason [28] due to the relatively small depth of liquid films

encountered in spray impingement situations, and hence adopt the equations of motion pertaining to a solid particle rebounding off a solid impact surface:

$$u_{t,s} = \frac{5}{7} u_{t,o} \tag{51}$$

$$u_{n,s} = -u_{n,o}\left[0.9930 - 0.0307\left(90^\circ - \theta_o\right) + 0.0272\left(90^\circ - \theta_o\right)^2 - 0.0086\left(90^\circ - \theta_o\right)^3\right] \tag{52}$$

In the absence of a detailed knowledge of physical influences on the splashed to incident droplet mass ratio, Bai and Gosman [26] make a random approximation of an experimentally observed range of values:

$$\frac{m_s}{m_o} = \begin{Bmatrix} 0.2 + 0.6 N_R[0,1] & H = 0 \\ 0.2 + 0.9 N_R[0,1] & H > 0 \end{Bmatrix} \tag{53}$$

The remainder of the splashing model is based on the assumption that each droplet will produce a number of fragments whose diameter is either $d_{s,1}$ or $d_{s,2}$. The total number of secondary droplets is obtained from a correlation of experimental data:

$$N_s = 5.0\left(\frac{We_s}{We_{s,c}} - 1.0\right) \tag{54}$$

The number of droplet fragments of diameter $d_{s,1}$ is randomly chosen to be $N_{s,1}$ and the number of droplet fragments of diameter $d_{s,2}$ follows from the requirement that $N_{s,2} = N_s - N_{s,1}$. The values of the diameters $d_{s,1}$ and $d_{s,2}$ may then be obtained from conservation of the splashed mass fraction:

$$d_{s,1} = \left(\frac{1}{2N_{s,1}} \frac{m_s}{m_o}\right)^{\frac{1}{3}} d_o \tag{55}$$

$$d_{s,2} = \left(\frac{1}{2N_{s,2}} \frac{m_s}{m_o}\right)^{\frac{1}{3}} d_o \tag{56}$$

The velocity components of secondary droplet fragments are determined from the principle of conservation of the incident droplet's kinetic energy and the consideration that a certain amount of energy is expended in the formation of secondary droplet surfaces:

$$\frac{1}{4}m_s\left(u_{s,1}^2+u_{s,2}^2\right)+\pi\sigma\left(N_{s,1}d_{s,1}^2+N_{s,2}d_{s,2}^2\right)=\frac{1}{2}m_o u_o^2-E_{k,c} \tag{57}$$

The critical amount of energy expended on droplet deformation and film formation may be derived from the critical Weber number:

$$E_{k,c}=\frac{\pi d_o^2\sigma}{12}We_{s,c} \tag{58}$$

Furthermore, the secondary droplet velocities are related by the following approximation:

$$\frac{u_{s,1}}{u_{s,2}}=\ln\left(\frac{d_{s,1}}{d_o}\right)\Big/\ln\left(\frac{d_{s,2}}{d_o}\right) \tag{59}$$

Randomly designating the value of the reflection angle of fragments of diameter $d_{s,1}$ as $\theta_{s,1}$, the reflection angle of fragments of diameter $d_{s,1}$ may be determined from the conservation of tangential momentum:

$$\frac{1}{2}m_s u_{s,1}\cos\left(\theta_{s,1}\right)+\frac{1}{2}m_s u_{s,2}\cos\left(\theta_{s,2}\right)=C_f m_o u_o\cos\left(\theta_o\right) \tag{60}$$

Hence, the magnitude and direction of secondary droplet velocities may be obtained from Equations (57) through (60) with $0.6\le C_f\le 0.8$.

The rebound component of the droplet impingement model proposed by Bai and Gosman [26] provides a physically viable alternative to that proposed by Jayaratne and Mason [28] and is considered to be applicable to thin liquid films. However, while the model's splashing component principally satisfies the requirements delineated in Section 3.2.2 it is deemed unsatisfactory from a physical perspective as its formulation relies heavily on potentially unjustified assumptions regarding secondary droplet characteristics.

### 3.2.7 Mundo and Tropea Impingement Model

While the regime transition criteria proposed by Wang and Watkins [30], as well as Bai and Gosman [26], account for droplet inertia and surface tension in the form of a critical impact Weber number, Mundo and Tropea [31-33] consider the additional effects of droplet viscosity in deriving a splashing criterion based on impact Weber and Reynolds numbers:

$$K_M = \left[ We_s \, \mathrm{Re}_s^{\frac{1}{2}} \right]^{\frac{1}{2}} = \left[ \frac{\rho_d^3 d_o^3 u_{n,o}^5}{\sigma^2 \mu_d} \right]^{\frac{1}{4}} \Rightarrow \begin{Bmatrix} K_M \le 57.7 & Spread \\ K_M > 57.7 & Splash \end{Bmatrix} \tag{61}$$

It is important to realize that Equation (61) may only be applicable to impingement configurations featuring surface roughness and film depth values in the vicinity of the experimental conditions $R = H = 0.03$ as the definition of $K_M$ does not explicitly account for impact surface conditions. This deficiency may be considered important as much of the splashing model, including the number of secondary droplets and the value of secondary droplet diameters, is defined as a function of the splashing parameter:

$$N_s = \min\left(1.676 \cdot 10^{-5} K_M^{2.539}, 1000\right) N_o \tag{62}$$

$$d_s = \min\left(8.720 \cdot e^{-0.028 K_M}, 1.000\right) d_o \tag{63}$$

The splashed to incident droplet mass ratio may be obtained from the number and sizes of secondary droplets:

$$\frac{m_s}{m_o} = \frac{N_s}{N_o} \left( \frac{d_s}{d_o} \right)^3 \tag{64}$$

The tangential and normal components of the mean secondary droplet velocity are defined as a function of splashed to incident diameter ratios:

$$u_{t,s} = u_{t,o} \left[ 1.337 - 1.318 \left( \frac{d_s}{d_o} \right) + 2.339 \left( \frac{d_s}{d_o} \right)^2 \right] \tag{65}$$

$$u_{n,s} = u_{n,o} \left[ -0.249 - 2.959 \left( \frac{d_s}{d_o} \right) + 7.794 \left( \frac{d_s}{d_o} \right)^2 \right] \tag{66}$$

Even though the concise splashing model proposed by Mundo and Tropea [31-33] provides a comprehensive description of the droplet-wall interaction process, the model's heavy reliance on $K_M$ limits its applicability to impingement situations featuring surface conditions in the vicinity of $R = H = 0.03$. Furthermore, the range of experimental droplet diameters and velocities is limited to respectively 150 μm and 18 m/s and hence the model's applicability to droplet impingement at typical SLD conditions is doubtful.

### 3.2.8 Stanton and Rutland Impingement Model

The droplet rebound component of the impingement model proposed by Stanton and Rutland [34] adopts Equations (51) and (52) as presented by Bai and Gosman [26] while assuming a slight alteration with respect to the transition point between droplet rebound and spread regimes such that $5 \le We_{s,c} \le 10$ instead of $We_{s,c} = 5$. Furthermore, the rebound model is rendered three-dimensional by randomly designating the value of the azimuthal reflection angle $\varphi_s$ to lie in the interval [90°, 270°] measured with respect to the $\hat{t}_1$ axis of the incident droplet trajectory.

The transition criterion designating incipient splashing is based on the experimental observations of Yarin and Weiss [35] and expressed as a function of the droplet impingement frequency:

$$We_{s,c} = 324 d_o \left(\frac{\rho}{\sigma}\right)^{\frac{1}{2}} \left(\frac{\mu}{\rho}\right)^{\frac{1}{4}} f^{\frac{3}{4}} \tag{67}$$

The splashed to incident droplet mass ratio is defined in terms of a non-dimensional droplet impact parameter according to Yarin and Weiss [35]:

$$K_Y = u_{n,o} \left[ \left(\frac{\rho}{\sigma}\right)^2 \left(\frac{\mu}{\rho}\right)^{-1} f^{-3} \right]^{\frac{1}{8}} \tag{68}$$

$$\frac{m_s}{m_o} = -27.2000 + 3.1500 K_Y - 0.1160 K_Y^2 + 0.0014 K_Y^3 \tag{69}$$

Secondary droplet diameters are based on statistical sampling of a cumulative probability density function (*pdf*) of diameters provided by Mundo and Tropea [31]:

$$pdf\left(\frac{d_s}{d_o}\right)=\left[\frac{A}{B}\left(\frac{d_s/d_o}{B}\right)^{A-1}\right]\cdot e^{-\left(\frac{d_s/d_o}{B}\right)^{A}} \Rightarrow \begin{Bmatrix} A=2.71-9.25\cdot 10^{-4}We_s \\ B=0.21-7.69\cdot 10^{-5}We_s \end{Bmatrix} \tag{70}$$

Similarly, the normal component of secondary droplet velocities is obtained from statistical sampling of a *pdf* of velocities provided by Mundo and Tropea [31]:

$$pdf\left(\frac{u_{n,s}}{u_{n,o}}\right)=\left[\frac{A}{B}\left(\frac{u_{n,s}/u_{n,o}}{B}\right)^{A-1}\right]\cdot e^{-\left(\frac{u_{n,s}/u_{n,o}}{B}\right)^{A}} \tag{71}$$

$$A=\begin{Bmatrix} 1.10+0.02\left(90^\circ-\theta_o\right) & \theta_o \le 40^\circ \\ 2.10 & \theta_o > 40^\circ \end{Bmatrix}, B=0.158e^{0.017\left(90^\circ-\theta_o\right)} \tag{72}$$

The tangential component of secondary droplet velocities may be determined from an experimentally correlated distribution of droplet reflection angles:

$$\theta_s = 24.6-0.266\left(90^\circ-\theta_o\right) \tag{73}$$

$$u_{t,s}=\frac{u_{n,s}}{\tan(\theta_s)} \tag{74}$$

In order to compensate for a finite number of statistical samples $n$, Stanton and Rutland [34] propose a correction factor based on overall energy conservation principles:

$$K_{SR}=\frac{\frac{1}{2}m_o u_o^2+\pi\sigma N_o d_o^2-\frac{1}{2}m_o\left[18\left(\frac{\sigma}{\rho_d}\right)^{\frac{1}{4}}\left(\frac{\rho_d}{\sigma}\right)^{\frac{1}{8}}f^{\frac{3}{8}}\right]^2}{\frac{1}{2}\sum_{i=1}^{n}m_{s,i}u_{s,i}^2+\pi\sigma\sum_{i=1}^{n}N_{s,i}d_{s,i}^2} \tag{75}$$

The normal and tangential components of the secondary droplet velocity are to be multiplied by $\sqrt{K_{SR}}$.

The inclusion of a randomly varying azimuthal reflection angle makes the droplet rebound model proposed by Stanton and Rutland [34] a preferred alternative over the original model proposed by Bai and Gosman [26] as it provides a three-dimensional rebound model. The splashing component of the droplet impingement model satisfies the criteria of Section 3.2.2 with the exception that impact surface conditions are not accounted for in the definition of the regime transition criteria. Furthermore, the statistical nature of the model requires multiple sampling of diameter and velocity probability density functions in order to arrive at a reasonable representation of secondary droplet characteristics. While multiple sampling may easily be incorporated in a droplet impingement model based on a Lagrangian formulation, this process causes fundamental difficulties in the Eulerian formulation of DROP3D$^{TM}$.

## 3.2.9 Mao and Tran Impingement Model

Mao and Tran [36] propose a model predicting the tendency of an impinging droplet to rebound upon impact as a function of a normalized excess rebound energy parameter:

$$E_{ERE} = \frac{1}{4}\left(\frac{D_{\max}}{d_o}\right)^2(1-\cos\phi) - \frac{3}{25}\left(\frac{D_{\max}}{d_o}\right)^{2.3}(1-\cos\phi)^{0.63} + \frac{2}{3}\left(\frac{D_{\max}}{d_o}\right) - 1 \qquad (76)$$

Droplet rebound occurs for $E_{ERE} > 0$ and the maximum spread ratio $D_{max}/d_o$ is implicitly defined as a function of droplet impact Reynolds and Weber numbers as well as the static surface contact angle $\phi$:

$$\left[\frac{1}{4}(1-\cos\phi) + \frac{1}{5}\frac{We_s^{0.83}}{\mathrm{Re}_s^{0.33}}\right]\left(\frac{D_{\max}}{d_o}\right)^3 - \left(1+\frac{We_s}{12}\right)\left(\frac{D_{\max}}{d_o}\right) + \frac{2}{3} = 0 \qquad (77)$$

While the impact surface conditions such as surface film thickness and surface roughness are accounted for in the form of the surface contact angle, the impingement model proposed by Mao and Tran merely distinguishes between the droplet spread and rebound regimes, failing to provide any information regarding secondary droplet characteristics. Furthermore, the range of experimental impingement velocities considered $[u_n \leq 6 m/s]$

is not at all representative of typical impingement velocities encountered at SLD conditions $[u_n \approx 100 m/s]$ and hence this particular impingement model is of very limited use in the intended application.

### 3.2.10 Schmehl and Wittig Impingement Model

The droplet impingement model developed by Schmehl and Wittig [37] considers a range of target surface temperatures, some of which extend beyond the boiling point of the constituent liquid. At temperatures below the boiling point, possible droplet-wall interaction mechanisms are limited to complete deposition of the incident droplet mass or droplet splashing. The regime transition criterion is defined as a function of droplet impact Reynolds and Laplace numbers only, neglecting a direct dependence on impact surface roughness and film thickness:

$$S_c = \frac{1}{24}\mathrm{Re}_s\, La^{-0.419} = \frac{1}{24}\frac{\rho_d^{0.581}}{\mu_d^{0.162}\sigma^{0.419}} d_o^{0.581} U_\infty \left\|\vec{u}_o\right\| \sin^{0.630}\left(90^\circ - \theta_o\right) \tag{78}$$

$S_c$ classifies an impinging droplet's inertial properties with respect to the critical inertia required to initiate droplet fragmentation upon impact:

$$\begin{Bmatrix} S_c < 1 & Spread \\ S_c > 1 & Splash \end{Bmatrix} \tag{79}$$

The ratio of splashed to incident droplet mass is based on experimental results pertaining to the interaction of droplets with thin wavy films and expressed as a function of the splashing parameter:

$$\frac{m_s}{m_o} = 1 - S^{-0.6} \tag{80}$$

Secondary droplet diameters are assumed to follow an empirical correlation based on experiments by Samenfink [38] as well as Stow and Stainer [41]:

$$\frac{d_s}{d_o} = e^{-\left(2+\frac{d_o}{4066}+0.05S\right)} \tag{81}$$

While Schmehl and Wittig [37] base the expressions for secondary droplet diameters and the splashed mass ratio on credible experimental data, the expressions pertaining to the magnitude and direction of secondary droplet velocities are purely based on estimation, failing to account for the effects of varying incidence and inertia:

$$|\vec{u}_s| = 0.6|\vec{u}_o| \tag{82}$$

$$10^\circ \leq \theta_s \leq 15^\circ \tag{83}$$

The rather questionable assumption that splashed droplets immediately follow the main stream flow in the near wall region renders the impingement model proposed by Schmehl and Wittig insufficiently justified for the intended application.

### 3.2.11 Samenfink and Wittig Impingement Model

Samenfink and Wittig [38] propose a physically comprehensive droplet impingement model featuring a particular focus on the influence of the surface liquid film thickness on secondary droplet characteristics. However, as the regime transition criterion is based on Schmehl's [37] splashing parameter (78), the influence of surface conditions on the onset of splashing remains unresolved.

The splashed to incident droplet mass ratio is defined in terms of the impinging droplet's inertia and the normalized surface film thickness:

$$\frac{m_s}{m_o} = 0.0866(S_c - 1.0)^{0.3188}\left(90^\circ - \theta_o\right)^{0.1233} H^{-0.9585} \tag{84}$$

Secondary droplet velocities are defined in terms of magnitude and direction rather than normal and tangential components:

$$\left|\frac{\vec{u}_s}{\vec{u}_o}\right| = 0.0821 S_c^{-0.3348}\left(90^\circ - \theta_o\right)^{0.2938} H^{-0.0311} La^{0.1157} \tag{85}$$

$$\left(90^\circ - \theta_s\right) = 2.1540 S_c^{1.0946} H^{-0.1589}\left(90^\circ - \theta_o\right)^{0.0339} \tag{86}$$

The correlation for secondary droplet diameters exhibits a similar functionality as the velocity correlation as it is based on droplet inertia, incidence angle and Laplace number:

$$\frac{d_s}{d_o} = 1.0 - 0.0345 S_c^{0.1750} \left(90^\circ - \theta_o\right)^{0.1239} La^{0.2650} \tag{87}$$

Based on the experimental correlations' range of validity as stated by Samenfink and Wittig [38] the given impingement model may be considered applicable within the range of droplet sizes, impact velocities and film thicknesses encountered in typical SLD conditions as the governing equations exhibit a limiting behavior at elevated impact velocities:

$$\left\{\begin{matrix} 1.0e+0 \le S_c \le 5.0e+0 & 5.0e+3 \le La \le 2.0e+4 \\ 3.0e-1 \le H \le 3.0e+0 & 0^\circ \le \theta_o \le 85^\circ \end{matrix}\right\} \tag{88}$$

## 3.2.12 Trujillo and Lee Impingement Model

The droplet impingement model developed by Trujillo and Lee [39] may be considered the most physically comprehensive description of factors influencing the droplet fragmentation process to date. While the regime transition criteria proposed by Bai and Gosman [26], Mundo and Tropea [31-33], Stanton and Rutland [34], as well as Samenfink and Wittig [38], feature some functional combination of the impact Weber or Reynolds numbers as well as the surface roughness or film thickness, none of these models directly account for the combined effects of surface roughness and film thickness.

By correlating experimental data pertaining to incipient splashing as reported by Stow and Hadfield [40] as well as Mundo and Tropea [31], Trujillo and Lee [39] obtain a purely empirical expression for the critical Cossali parameter at the onset of splashing on dry impact surfaces as a function of the normalized surface roughness:

$$K_{C,dry} = 180 R^{-0.35} \tag{89}$$

In order to derive a critical value of the Cossali parameter corresponding to incipient splashing on wetted impact surfaces, Trujillo and Lee [39] apply experimental values of

droplet frequency and diameters as stated by Yarin and Weiss [35] to the definition of the Yarin parameter, facilitating a recast in the following form:

$$K_Y' = 0.45^{-\frac{3}{8}} \left( Oh^{-\frac{2}{5}} We_s \right)^{\frac{5}{16}} \tag{90}$$

The mathematical relationship between splashing on dry and wet impact surfaces is obtained from the ratio of critical Cossali parameters pertaining to each situation at an experimental surface roughness of $R = 0.005$, yielding an empirical expression for the critical Cossali parameter at the onset of splashing on wet impact surfaces:

$$K_{C,wet} \approx 3.0 K_{C,dry} = 540 R^{-0.35} \tag{91}$$

While the derivation of Equation (91) is based on a particular value of the normalized surface roughness, Trujillo and Lee [39] assume the relation to be a reasonably valid approximation over the range of surface roughness values encountered in engine intake manifolds at cold start conditions, which feature surface characteristics comparable to those of airfoil lift and control surfaces.

Expressions for the normal and tangential components of secondary droplet velocities are determined from cumulative probability density functions based on the experimental data reported by Mundo [31], whose mean values follow a simple functional relationship with the angle of incidence:

$$\frac{u_{t,s}}{u_{t,o}} = +\left(0.85 + 0.0025\theta_o\right) \tag{92}$$

$$\frac{u_{n,s}}{u_{n,o}} = -\left(0.12 + 0.0020\theta_o\right) \tag{93}$$

In order to render the splashing model three-dimensional, Trujillo and Lee [39] adopt a randomly varying distribution of the azimuthal reflection angle as originally proposed by Naber and Reitz [29]:

$$\varphi_s = -\frac{\pi}{\chi} \ln\left[1.0 - N_R[0,1]\left(1.0 - e^{-\chi}\right)\right] \tag{94}$$

The parameter $\chi$ may be obtained from its implicit definition in terms of a momentum balance:

$$\sin(\theta_o) = \left(\frac{e^{\chi}+1}{e^{\chi}-1}\right)\left(\frac{1}{1+(\pi/\chi)^2}\right) \tag{95}$$

The number of secondary droplet fragments is obtained from a curve fit of the experimental data reported by Stow and Stainer [41]:

$$N_s = \frac{1}{22}\left\{0.0437\left[K_C\left(\frac{|\vec{u}_o|}{u_{n,o}}\right)^2 - K_{C,dry}\right] - 44.92\right\} \tag{96}$$

The splashed to incident droplet mass ratio is based on the experimental data reported by Yarin and Weiss [35]:

$$\frac{m_s}{m_o} = 0.8\left[1.0 - e^{-0.85(K_Y'-17)}\right] \tag{97}$$

Finally, secondary droplet diameters may be determined based on knowledge of the number and mass of secondary particles, combined with the principle of mass conservation:

$$\frac{d_s}{d_o} = \left(\frac{m_s}{m_o}\frac{1}{N_s}\right)^{\frac{1}{3}} \tag{98}$$

Thus, the splashing component of the droplet impingement model proposed by Trujillo and Lee [39] satisfies all requirements delineated in Section 3.2.2 in addition to presenting the only regime transition criterion that directly accounts for both surface roughness and film thickness. Furthermore, the experimental range of incident droplet diameters and velocities justifies the application of this particular empirical model in SLD conditions:

$$[25\mu m \le d_o \le 880\mu m] \tag{99}$$

$$[0 m/s \le |\vec{u}_o| \le 43 m/s] \tag{100}$$

# 4 PROPOSED MATHEMATICAL MODEL

## 4.1 Terminal Droplet Velocity

The empirical correlation describing terminal droplet velocity as a function of droplet diameter as proposed by Khan and Richardson [24] is deemed suitable to account for the augmented approach velocity of SLD droplets. Once the terminal velocity corresponding to a given droplet diameter is obtained from Equations (39) and (40), the initial conditions prescribed in Section 2.2.5 may be changed accordingly:

$$\vec{u}_d = \begin{Bmatrix} u_d \\ v_d \\ w_d \end{Bmatrix} = \begin{Bmatrix} u_{d-t} + g_x|\vec{u}_t| \\ v_{d-t} + g_y|\vec{u}_t| \\ w_{d-t} + g_z|\vec{u}_t| \end{Bmatrix} \tag{101}$$

In Equation (101), $\{u_{d-t}, v_{d-t}, w_{d-t}\}$ denotes the initial droplet velocity vector in the absence of the terminal droplet velocity while $\{g_x, g_y, g_z\}$ represents the gravitational unit vector in the global Cartesian coordinate system.

## 4.2 Droplet-Wall Interactions

A detailed review of published literature pertaining to typical droplet-wall collisions reveals a variety of semi-empirical modeling approaches. Following a critical appraisal of these models with respect to physical comprehensiveness and applicability in SLD conditions, the droplet impingement model proposed by Trujillo and Lee [39] is deemed most suitable for the description of droplet splashing phenomena while the model developed by Bai and Gosman [26] is considered to entail the most representative description of droplet bouncing processes. Further model development will hence be based on these particular semi-empirical formulations. While the model developed by Samenfink and Wittig [38] presents a viable alternative, Wright and Potapczuk [42] have demonstrated the model's tendency to predict unreasonably large mass losses in a recent investigation of splashing effects based on the NASA LEWICE [10] code.

### 4.2.1 Conceptual Solution Methodologies

Having decided on a particular empirical description of the droplet-wall interaction process, a corresponding mathematical model may principally be formulated in an Eulerian context. However, an inspection of the functionality of the empirical correlations developed by Trujillo and Lee [39] as well as Bai and Gosman [26] reveals that any information regarding the droplet-wall interaction process is provided in terms of an individual droplet's pre- and post-impact properties:

$$\frac{u_s}{u_o} = f_u \qquad \frac{m_s}{m_o} = f_m \qquad \frac{d_s}{d_o} = f_d \qquad \frac{N_s}{N_o} = f_N \tag{102}$$

Since Equation (102) is expressed in a purely Lagrangian context, an adequate connection between the Lagrangian and Eulerian reference frames must be established in order to make the desired empirical information available in an Eulerian context. Several conceptual solution methodologies have been identified in pursuit of this objective and will be discussed with respect to feasibility and comprehensiveness.

#### 4.2.1.1 Modification of Collection Efficiency

A modification of the local collection efficiency $\beta_o$ obtained from the solution of the equations governing continuity and momentum in the absence of droplet-wall collisions may be facilitated by decomposing the net collection efficiency $\beta$ into pre- and post-impact components in a straightforward post-processing endeavor:

$$\beta = \beta_o - \beta_s = \left(\frac{\dot{m}_o - \dot{m}_s}{A}\right) \Big/ \left(\frac{\dot{m}_o}{A}\right)_\infty = \left(1 - \frac{\dot{m}_s}{\dot{m}_o}\right)\left(\frac{\dot{m}_o}{A}\right) \Big/ \left(\frac{\dot{m}_o}{A}\right)_\infty = (1 - f_m)\beta_o \tag{103}$$

While this approach may yield a sufficiently augmented distribution of local collection efficiencies to account for the mass redistribution incurred during droplet-wall collisions, the pronounced effect on droplet trajectories in the vicinity of solid boundaries is neglected. However, an analysis of the relations governing the ice accretion process presented in Section 2.3 stipulates that the droplet velocity field must be altered, in addition to the collection efficiency, in order to fully incorporate the effects of collisions.

### 4.2.1.2 Modification of Impingement Velocity

Instead of simply augmenting the distribution of local collection efficiencies, the impingement velocities obtained from the solution of the equations governing continuity and momentum in the absence of droplet-wall collisions may be modified in order to account for the effects of collisions on droplet trajectories and hence local collection efficiencies. This approach is based on an Eulerian interpretation of the collision process as illustrated schematically in Figure 4-1. Rather than establishing the individual impingement locations of an incident droplet and its associated secondary fragments, the splashing process is thought to result in a translation of the impingement location corresponding to the incident liquid mass.

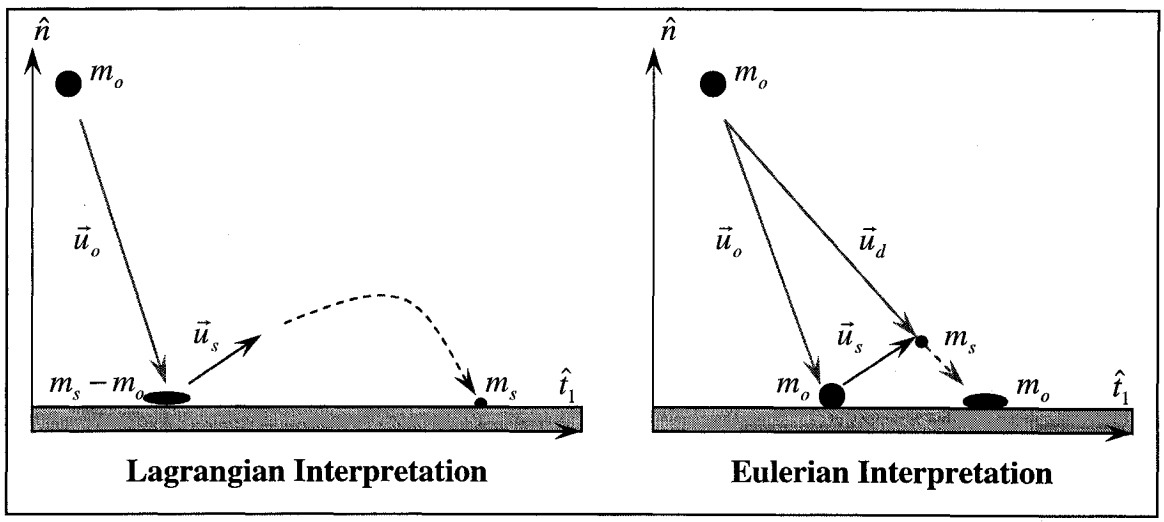


**Figure 4-1: Lagrangian and Eulerian Interpretations of Droplet-Wall Collisions**

Decomposing the net droplet momentum into pre- and post-impact components, the droplet impingement velocity may be modified in a simple post-processing endeavor:

$$m_o\vec{u}_d = m_o\vec{u}_{d,o} + m_s\vec{u}_{d,s} = m_o\vec{u}_{d,o}\left(1 + f_m f_u\right) \tag{104}$$

While this approach principally accounts for the effects of collisions on droplet trajectories and local collection efficiencies, it fails to accommodate further propagation of the liquid mass splashed during impact and hence neglects the effects of droplet-wall collisions on surfaces located downstream of the initial impingement location.

### 4.2.1.3 Modification of Boundary Conditions

A consideration of the insufficient physical comprehensiveness associated with simple post-processing methodologies suggests the inclusion of information pertaining to the droplet-wall collision process during the solution of the equations governing continuity and momentum rather than after. Hypothetically, the empirical information regarding secondary droplet properties may be introduced to an Eulerian formulation by modifying the boundary conditions applied at solid system boundaries. However, as outlined in Section 2.2.5 and illustrated in Figure 4-2, incident droplets consider a solid surface as part of the system's outflow boundary, while secondary droplet fragments would consider the same surface as an inflow boundary. As a consequence, incident droplets do not allow the specification of boundary conditions on an impact surface for reasons of system uniqueness and stability, while secondary fragments require the specification of Dirichlet boundary conditions at the same location.

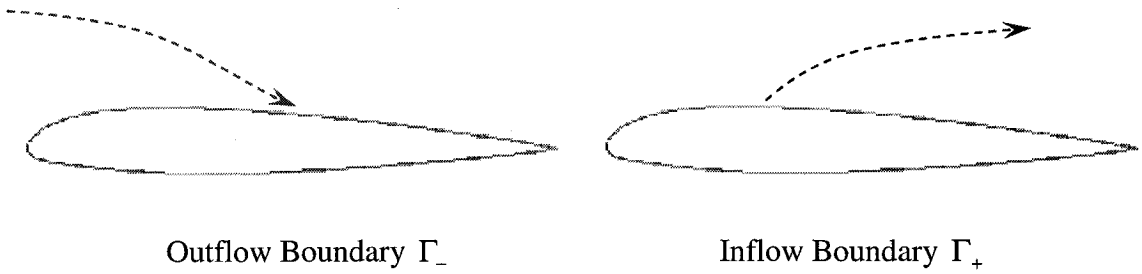


**Figure 4-2: Conflict of System Characteristics on Impingement Surfaces**

In order to alleviate the resulting conflict between incoming and outgoing system characteristics, two systems of partial differential equations would be required to model the effects of droplet-wall collisions: the system of Equations (9) and (19) to describe the propagation of incident droplet mass and an analogous system to describe the propagation of secondary droplet mass based on empirically correlated initial conditions. While it is principally feasible to meaningfully couple the two systems, the required specification of Dirichlet boundary conditions on impact surfaces will impede the re-impingement behavior of secondary droplet fragments and lead to an unphysical accumulation of mass in the vicinity of solid boundaries. Hence, droplet impingement limits and local collection efficiencies cannot be properly resolved by this approach.

### 4.2.1.4 Modification of Governing Equations

As an alteration of boundary conditions on impingement surfaces is deemed unfeasible, a modification of the equations governing continuity and momentum becomes necessary in order to fully account for the three dimensional effects of droplet-wall interactions in an Eulerian frame of reference. Due to its fundamental nature, the continuity equation must apply in its stated form (9), irrespective of a particular interaction mechanism's applicability, and hence the effects of collisions must be incorporated in the relations governing droplet momentum.

During any impingement process, a droplet's kinetic energy is imparted on the target surface in the form of an impulse. According to Newton's Third Law, an equal and opposite impulse will be imparted by the surface on the droplet, leading to a change in droplet momentum. The magnitude of the momentum change depends on a particular interaction mechanism: in case of the stick and spread mechanisms defined in Section 3.2.1, it merely suffices to arrest an impinging droplet on the target surface, while the momentum change resulting from bounce and splash mechanisms allows an impinging droplet to leave the target surface following impact.

Hence, a relation between the empirical information describing a particular interaction mechanism and the associated change in droplet momentum must be established. As demonstrated in Section 2.2.3, the droplet momentum equations describe the effects of drag, gravity and buoyancy forces on droplet trajectories. This suggests an interpretation of the droplet-wall interaction process in terms of a body force applicable at solid boundaries, as illustrated schematically in Figure 4-3.

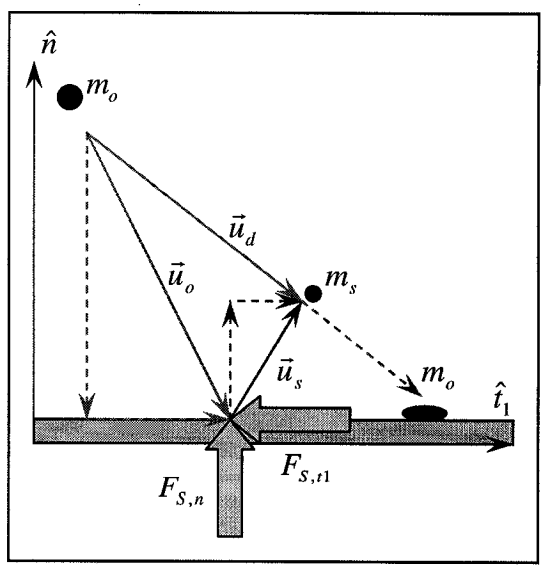


**Figure 4-3: Body Force Interpretation**

### 4.2.2 Source Term Formulation

Based on the foregoing discussion of conceptual solution methodologies, a modification of the equations governing droplet momentum is deemed the most physically comprehensive approach to the introduction of droplet-wall interactions in the current mathematical formulation. In addition to augmenting the droplet impingement velocities and local collection efficiencies, this approach accounts for the propagation of mass reintroduced into the computational domain due to droplet bouncing and splashing during impact. Thus, the effects of droplet-wall interactions on locations located downstream of primary impingement locations are addressed as well.

A formulation of the droplet-wall interaction process in terms of a body force $\vec{F}_S$ would facilitate a relatively straightforward extension of the method used to derive the droplet momentum equations in Section 2.2.3:

$$\frac{D\vec{u}_d}{Dt} = \frac{\partial \vec{u}_d}{\partial t} + \vec{u}_d \cdot \nabla \vec{u}_d = \frac{1}{m_o}\left[\vec{F}_D + \vec{F}_B + \vec{F}_G + \vec{F}_S\right] \tag{105}$$

As established in Section 3.2.2, the current form of the droplet momentum equations (19) suffices to model the stick and spread mechanisms in as far as droplet trajectories terminate at solid boundaries following impact. Therefore, the body force associated with the change in droplet momentum due to impingement phenomena merely needs to account for the effects of droplet bouncing and splashing.

According to the particular interpretation presented in Figure 4-3, $\vec{F}_S$ should be based on the momentum change introduced by the translation of secondary droplet mass following impingement:

$$\vec{F}_S = \left.\frac{d(m_d \vec{u}_d)}{dt}\right|_S = m_s \left.\frac{d\vec{u}_d}{dt}\right|_S \tag{106}$$

Strictly speaking, the time derivative in Equation (106) represents the instantaneous change in momentum incurred by the secondary droplet mass at the time of impact due to the impulse delivered by the target surface. To the knowledge of the author, however, the published literature reveals no information regarding the magnitude of such an impulse.

The proposed formulation hence approximates the exact time derivative by a linear variation between pre- and post-impact velocities over an associated time interval $\Delta T_S$ defined as the collision contact time:

$$\vec{F}_S \approx m_s \left.\frac{\Delta \vec{u}_d}{\Delta t}\right|_S = m_s \left(\frac{\vec{u}_s - \vec{u}_o}{\Delta T_S}\right) \tag{107}$$

Within the context of Equation (107), the contact time may be considered as the time span required for a droplet to decelerate from its initial impingement velocity upon approaching a surface, come to a temporary rest on the surface and accelerate to the post-impact velocity predicted by the applicable empirical description.

In order to accommodate the functionality of the empirical correlations as denoted in Equation (102), a recast of Equation (107) becomes necessary:

$$\vec{F}_S = m_o \left(\frac{m_s}{m_o}\right)\left[\frac{\vec{u}_o}{\Delta T_S}\left(\frac{\vec{u}_s}{\vec{u}_o} - 1\right)\right] = \frac{m_o \vec{u}_o}{\Delta T_S}\left(\frac{m_s}{m_o}\right)\left(\frac{\vec{u}_s}{\vec{u}_o} - 1\right) = \frac{m_o \vec{u}_o}{\Delta T_S} f_m \left(f_u - 1\right) \tag{108}$$

Although the functions $f_m$ and $f_u$ are provided by either Bai and Gosman [26] or Trujillo and Lee [39], their particular form depends on the applicability of either droplet splashing or bouncing mechanisms and more importantly on the choice between local and global coordinate systems. As the chosen empirical correlations are formulated in terms of the local impingement coordinate system defined in Figure 3-3, Equation (108) must be expressed in the global Cartesian coordinate system prior to its inclusion in the droplet momentum equations.

### 4.2.3 Transformation of Coordinate System

The empirical correlations provided by either Bai and Gosman [26] or Trujillo and Lee [39] may be restated in terms of the functions $f_m$ and $f_u$ in the local impingement coordinate system. The distinction between droplet bouncing ($R_1$) and spreading regimes is based on a combination of the ranges of critical Weber numbers proposed by Bai and Gosman [26], as well as Stanton and Rutland [34], while the transition between spreading and splashing ($R_2$) regimes is based on the critical value of the Cossali parameter identified by Trujillo and Lee [39]:

$$\begin{Bmatrix} R_1 \\ R_2 \end{Bmatrix} \equiv \begin{Bmatrix} 10 \le We_{s,c} \le 1320La^{-0.18} \\ K_C \ge 540R^{-0.35} \end{Bmatrix} \tag{109}$$

$$f_m = \frac{m_s}{m_o} = \begin{Bmatrix} 1.0 & R_1 \\ 0.8\left[1.0 - e^{-0.85(K_Y'-17)}\right] & R_2 \end{Bmatrix} \tag{110}$$

An inspection of the constituent parameters of Equation (109) reveals that $f_m$ depends on the normal component of the impingement velocity. The empirical information regarding secondary droplet velocities is presented in terms of tangential and normal components, respectively denoted as $f_{u,t}$ and $f_{u,n}$. While the normal component of the bouncing model proposed by Bai and Gosman [26] is adopted in the proposed formulation, its tangential component is based on the splashing model proposed by Trujillo and Lee [39] in order to account for variations in incidence:

$$f_{u,t} = \frac{u_{t,s}}{u_{t,o}} = +\begin{Bmatrix} 0.8500 + 0.0025\theta_o & R1 \\ 0.8500 + 0.0025\theta_o & R_2 \end{Bmatrix} \tag{111}$$

$$f_{u,n} = \frac{u_{n,s}}{u_{n,o}} = -\begin{Bmatrix} 0.9930 - 0.0307\bar{\theta}_o + 0.0272\bar{\theta}_o^{\,2} - 0.0086\bar{\theta}_o^{\,3} & R1 \\ 0.1200 + 0.0020\theta_o & R_2 \end{Bmatrix} \tag{112}$$

where the parameter $\bar{\theta}_0$ represents the conjugate incidence angle, i.e. $\bar{\theta}_0 = 90^\circ - \theta_0$.

In order to facilitate an inclusion of Equations (110) through (112) in the extended droplet momentum Equations (105), a connection between the local and global coordinate systems must be established:

$$\left(\hat{n},\hat{t}_1,\hat{t}_2\right) \Leftrightarrow \left(\hat{i},\hat{j},\hat{k}\right) \tag{113}$$

The pre-impact droplet velocity may be decomposed into a component normal to the target surface and a complementary tangential component:

$$\vec{u}_o = \begin{Bmatrix} u_o \\ v_o \\ w_o \end{Bmatrix} \begin{Bmatrix} \hat{i} \\ \hat{j} \\ \hat{k} \end{Bmatrix} = \vec{u}_{n,o} + \vec{u}_{t,o} \tag{114}$$

The normal component may be obtained by projecting the incident velocity vector on the surface normal vector at the point of impingement:

$$\vec{u}_{n,o} = \left(\vec{u}_o \cdot \hat{n}\right)\hat{n} = \left(u_o n_x + v_o n_y + w_o n_z\right)\hat{n} = \left|\vec{u}_{n,o}\right| \begin{Bmatrix} n_x \\ n_y \\ n_z \end{Bmatrix} \begin{Bmatrix} \hat{i} \\ \hat{j} \\ \hat{k} \end{Bmatrix} \tag{115}$$

The tangential component follows from a combination of Equations (114) and (115):

$$\vec{u}_{t,o} = \vec{u}_o - \vec{u}_{n,o} = \begin{Bmatrix} u_o - n_x\left|\vec{u}_{n,o}\right| \\ v_o - n_y\left|\vec{u}_{n,o}\right| \\ w_o - n_z\left|\vec{u}_{n,o}\right| \end{Bmatrix} \begin{Bmatrix} \hat{i} \\ \hat{j} \\ \hat{k} \end{Bmatrix} \tag{116}$$

The unit vector $\hat{t}_1$ denoting the primary surface tangential direction of the droplet impingement trajectory may be obtained from normalization of the tangential velocity component:

$$\hat{t}_1 = \frac{\vec{u}_{t,o}}{\left|\vec{u}_{t,o}\right|} = \begin{Bmatrix} t_{1,x} \\ t_{1,y} \\ t_{1,z} \end{Bmatrix} \begin{Bmatrix} \hat{i} \\ \hat{j} \\ \hat{k} \end{Bmatrix} = \frac{1}{\left|\vec{u}_{t,o}\right|} \begin{Bmatrix} u_o - n_x\left|\vec{u}_{n,o}\right| \\ v_o - n_y\left|\vec{u}_{n,o}\right| \\ w_o - n_z\left|\vec{u}_{n,o}\right| \end{Bmatrix} \begin{Bmatrix} \hat{i} \\ \hat{j} \\ \hat{k} \end{Bmatrix} \tag{117}$$

The unit vector $\hat{t}_2$ denoting the secondary surface tangential direction of the droplet impingement trajectory may be obtained from the vector cross product of $\hat{t}_1$ and $\hat{n}$:

$$\hat{t}_2 = \hat{n} \otimes \hat{t}_1 = \begin{Bmatrix} t_{2,x} \\ t_{2,y} \\ t_{2,z} \end{Bmatrix} \begin{Bmatrix} \hat{i} \\ \hat{j} \\ \hat{k} \end{Bmatrix} = \begin{Bmatrix} n_y t_{1,z} - n_z t_{1,y} \\ n_z t_{1,x} - n_x t_{1,z} \\ n_x t_{1,y} - n_y t_{1,x} \end{Bmatrix} \begin{Bmatrix} \hat{i} \\ \hat{j} \\ \hat{k} \end{Bmatrix} \tag{118}$$

Having established the required connection between local and global coordinate systems, a transformation of secondary droplet velocities as prescribed by Equations (111) and (112) may be facilitated:

$$\vec{u}_s = \begin{Bmatrix} u_{n,s} \\ u_{t1,s} \\ u_{t2,s} \end{Bmatrix} \begin{Bmatrix} \hat{n} \\ \hat{t}_1 \\ \hat{t}_2 \end{Bmatrix} = \begin{Bmatrix} f_{u,n} \left| \vec{u}_{n,o} \right| \\ f_{u,t} \left| \vec{u}_{t,o} \right| \cos \varphi_s \\ f_{u,t} \left| \vec{u}_{t,o} \right| \sin \varphi_s \end{Bmatrix} \begin{Bmatrix} \hat{n} \\ \hat{t}_1 \\ \hat{t}_2 \end{Bmatrix} \tag{119}$$

As defined by Equation (94) and illustrated in Figure 3-3, Trujillo and Lee [39] define an azimuthal reflection angle $\varphi_s$ to accommodate an arbitrary variation in post-impact droplet velocity in a surface tangential plane. The definition of $\varphi_s$ as a truly randomly varying parameter has a rather peculiar implication in an Eulerian frame of reference: the average of the $\varphi_s$ values arbitrarily assigned to all droplets impinging at a given location over a given time frame tends to zero in the limit of an infinite number of individual droplets.

Therefore, an azimuthal reflection angle of $\varphi_s = 0$ is used in the proposed formulation, permitting a simplification of the secondary droplet velocity vector:

$$\vec{u}_s = \begin{Bmatrix} u_{n,s} \\ u_{t1,s} \\ u_{t2,s} \end{Bmatrix} \begin{Bmatrix} \hat{n} \\ \hat{t}_1 \\ \hat{t}_2 \end{Bmatrix} = \begin{Bmatrix} f_{u,n} \left| \vec{u}_{n,o} \right| \\ f_{u,t} \left| \vec{u}_{t,o} \right| \\ 0 \end{Bmatrix} \begin{Bmatrix} \hat{n} \\ \hat{t}_1 \\ \hat{t}_2 \end{Bmatrix} \tag{120}$$

Describing $(\hat{n},\hat{t}_1,\hat{t}_2)$ in terms of their $(\hat{i},\hat{j},\hat{k})$ equivalents, an expression for the secondary velocity components is obtained in the global Cartesian coordinate system:

$$\vec{u}_s = f_{u,n}\left|\vec{u}_{n,o}\right|\left(n_x\hat{i}+n_y\hat{j}+n_z\hat{k}\right)+f_{u,t}\left|\vec{u}_{t,o}\right|\left(t_{1,x}\hat{i}+t_{1,y}\hat{j}+t_{1,z}\hat{k}\right) \tag{121}$$

$$\vec{u}_s = \begin{Bmatrix} f_{u,n}\left|\vec{u}_{n,o}\right|n_x + f_{u,t}\left|\vec{u}_{t,o}\right|t_{1,x} \\ f_{u,n}\left|\vec{u}_{n,o}\right|n_y + f_{u,t}\left|\vec{u}_{t,o}\right|t_{1,y} \\ f_{u,n}\left|\vec{u}_{n,o}\right|n_z + f_{u,t}\left|\vec{u}_{t,o}\right|t_{1,z} \end{Bmatrix} \begin{Bmatrix} \hat{i} \\ \hat{j} \\ \hat{k} \end{Bmatrix} = \begin{Bmatrix} u_s \\ v_s \\ w_s \end{Bmatrix} \begin{Bmatrix} \hat{i} \\ \hat{j} \\ \hat{k} \end{Bmatrix} \tag{122}$$

The secondary droplet velocity may now be substituted into the expression for the body force accounting for droplet-wall interactions:

$$\vec{F}_S = \frac{m_o f_m}{\Delta T_S} \begin{Bmatrix} u_s - u_o \\ v_s - v_o \\ w_s - w_o \end{Bmatrix} \begin{Bmatrix} \hat{i} \\ \hat{j} \\ \hat{k} \end{Bmatrix} = \frac{m_o f_m}{\Delta T_S}\left(\vec{u}_{d,s} - \vec{u}_{d,o}\right) \tag{123}$$

## 4.2.4 Momentum Equations

At this point, Equation (123) may be substituted for $\vec{F}_S$ in Equation (105), resulting in a set of droplet momentum equations that account for the presence of droplet-wall interactions:

$$\frac{D\vec{u}_d}{Dt} = \frac{\partial \vec{u}_d}{\partial t} + \vec{u}_d \cdot \nabla \vec{u}_d = \frac{C_D \,\mathrm{Re}_d}{24K}\left(\vec{u}_a - \vec{u}_{d,o}\right) + \left(1 - \frac{\rho_a}{\rho_d}\right)\frac{\hat{g}}{Fr^2} + \frac{f_m}{\Delta T_S}\left(\vec{u}_{d,s} - \vec{u}_{d,o}\right) \tag{124}$$

As the surface normal vector is only defined at solid boundaries, it follows from an inspection of Equations (122) and (123) that the body force accounting for droplet-wall interactions is identically zero throughout the computational domain with the exception of computational nodes located on solid boundaries featuring impingement characteristics within the bouncing and splashing regimes defined by Equation (109).

## 4.2.5 Continuity Equation

As briefly mentioned in Section 2.2.1, the mathematical formulation of DROP3D$^{TM}$ neglects the physical phenomena of droplet-droplet interactions such as collisions and coalescence for the sake of computational feasibility. Consequently, there exists no physical means of communication between individual droplets even though they are assumed to constitute a continuous phase throughout the computational domain. A true continuum, however, is characterized by the ability to communicate external disturbances throughout the physical space occupied by its constituent particles by means of inter-particle collisions. In the case of gases, the stochastic average of the forces experienced in inter-molecular collisions resulting from the application of an external disturbance gives rise to the concept of pressure.

The absence of a pressure equivalent source term in the droplet momentum equations implies that external disturbances associated with solid system boundaries cannot be communicated into the computational domain. Contrary to the behavior of the constituent molecules of a truly continuous gas phase resulting in a flow tangency condition at solid boundaries, droplets strike an impingement surface without any prior knowledge of the imminent impact. Figure 4-4 provides a schematic illustration of the velocity profiles resulting near a solid boundary in the presence or absence of a pressure equivalent source term in the equations governing droplet momentum.

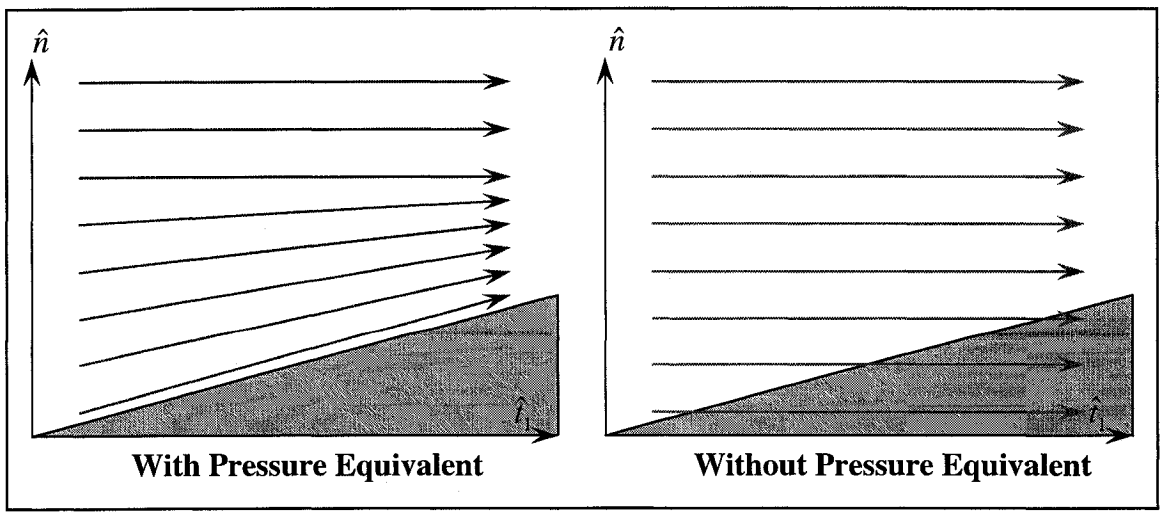


**Figure 4-4: Velocity Profiles in the Vicinity of a Solid Boundary**

In the absence of droplet-wall interactions, either velocity profile is continuous irrespective of flow tangency, resulting in a local velocity divergence that tends to zero in the limit of numerical convergence. However, the introduction of a body force $\vec{F}_S$ at a solid boundary results in an augmentation of the near wall velocity vector, which cannot be communicated into the computational domain in the absence of a pressure equivalent source term, resulting in a locally discontinuous velocity profile and hence a local velocity divergence which does not tend to zero in the limit of numerical convergence. As the velocity divergence may be considered as an explicit source term in the equation governing droplet continuity, a discontinuous velocity field in the vicinity of solid boundaries inherently affects the evolution of the volumetric fraction of liquid at such locations. More specifically, the locally non-zero velocity divergence term leads to an unphysical accumulation of liquid mass in elements adjacent to solid boundaries in the limit of numerical convergence. In order to overcome this deficiency of the mathematical model, the droplet continuity equation is recast in the following form:

$$\frac{\partial \alpha}{\partial t} + \vec{u}_d \cdot \nabla \alpha = \begin{Bmatrix} -\nabla \cdot \vec{u}_d & \vec{F}_S = 0 \\ 0 & \vec{F}_S \neq 0 \end{Bmatrix} \tag{125}$$

## 4.2.6 Droplet Breakup

The effects of droplet splashing and bouncing on droplet diameter may be accounted for by a straightforward modification of the minimum stable diameter and the breakup time span employed by the existing droplet breakup model introduced in Section 2.2.7:

$$d_{stab,s} = \begin{Bmatrix} 1 & R_1 \\ \left\{ 17.6\left[1.0 - e^{-0.85(K_Y - 17)}\right]\left\{ 0.0437\left[ K_C \left( \frac{|\vec{u}_o|}{u_{n,o}} \right)^2 - K_{C,dry} \right] - 44.92 \right\}^{-1} \right\}^{\frac{1}{3}} & R_2 \end{Bmatrix} \tag{126}$$

$$\frac{Dd}{Dt} = \frac{\partial d}{\partial t} + \vec{u}_d \cdot \nabla d = \frac{\min\left(d_{stab,s}, d_{stab}\right) - d_o}{\min\left(\Delta T_S, T\right)} \tag{127}$$

# 4.3 Solution Algorithm

A revision of the numerical solution algorithm is necessary to accommodate the proposed modifications as an initial solution ($I_M = 0$) of the equations governing droplet behavior in the absence of droplet-wall interactions is required in order to enable an accurate estimate of droplet impingement regimes. Figure 4-5 illustrates the resulting algorithmic disparity between the original (solid) and proposed (dashed) solution methodologies.

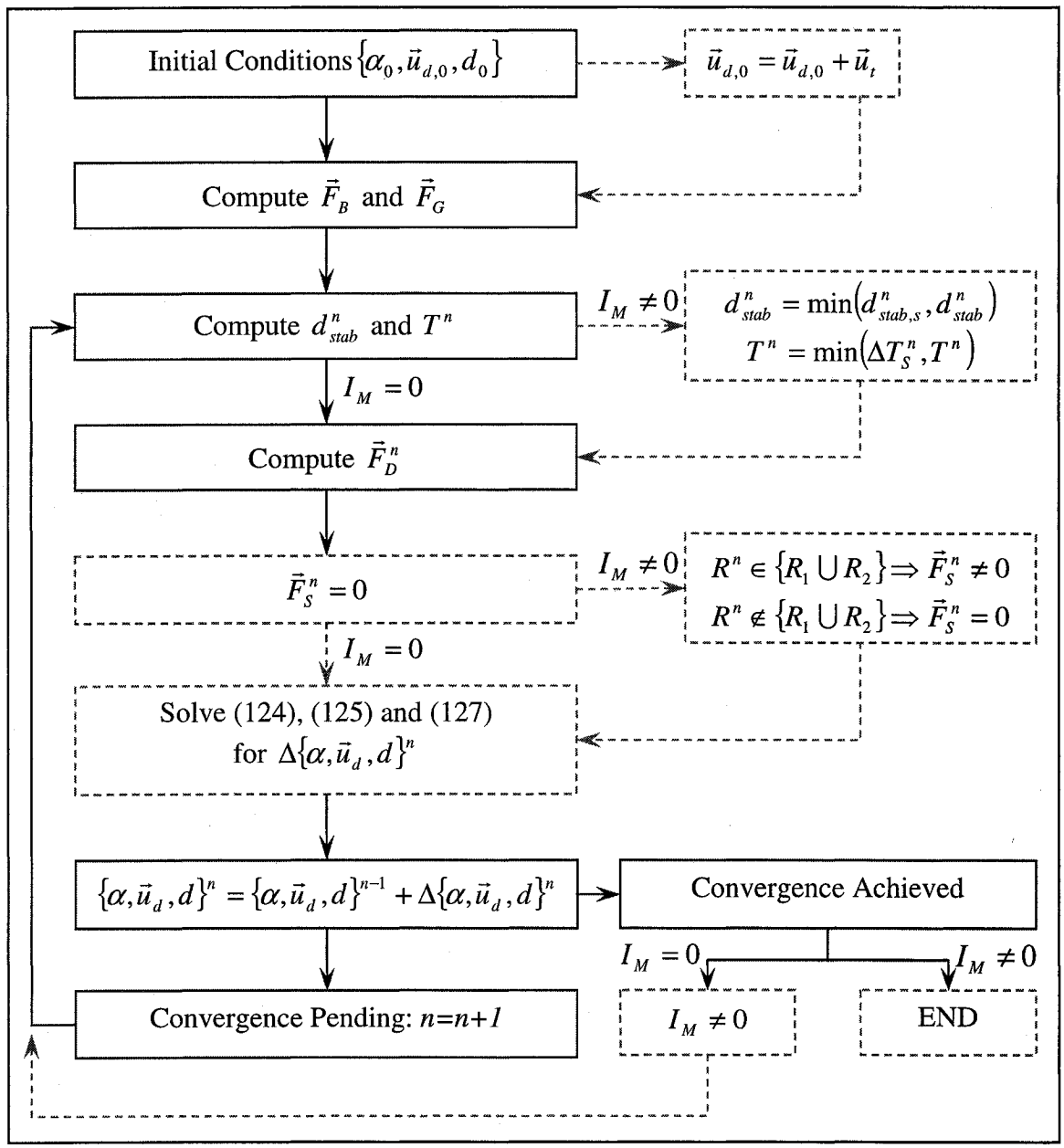


**Figure 4-5: Comparison of Original and Proposed Solution Algorithms**

The introduction of a source term accounting for droplet-wall interactions has a pronounced effect on the overall amount of liquid water accumulating on an impact surface as illustrated in Figure 4-6 in terms of a total collection efficiency. A sufficiently converged initial solution ($I_M = 0$) of the equations governing droplet behavior in the absence of droplet-wall interactions is obtained after approximately 200 solver iterations, at which point the extended solution methodology ($I_M \neq 0$) is invoked.

Since the proposed form of the governing equations accounts for the effects of droplet-wall interactions, the overall amount of liquid water accumulation decreases and a sharp reduction in the total collection efficiency may be observed. Following minor oscillations, the numerical solution converges monotonically to a value of the total collection efficiency denoting the amount of liquid water accumulating on a given impact surface under the influence of droplet-wall interactions. Figure 4-6 thus serves to demonstrate continued mathematical well-posedness and numerical robustness following the introduction of a source term in the equations governing droplet momentum.

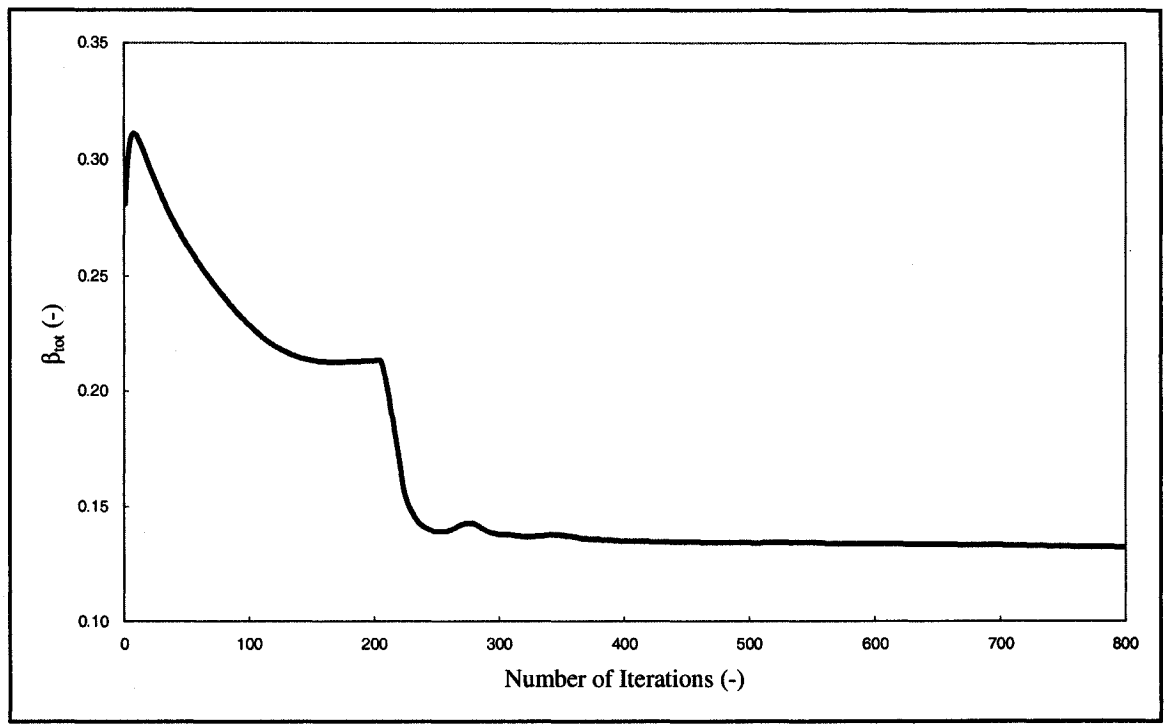


**Figure 4-6: Convergence History of DROP3D Based on Proposed Solution Algorithm**

# 5 MODEL CALIBRATION

While suitable expressions have been formulated to account for the effects of droplet-wall interactions on droplet volume fraction, velocity and diameter, a precise definition of the collision contact time and its potential for variation with droplet impingement characteristics remains to be established at this point.

The collision contact time is defined in Section 4.2.2 as the time span required for a droplet to decelerate from its pre-impact velocity upon approaching a surface, interact with the surface and subsequently accelerate to its post-impact velocity. Hypothetically, the contact time may be expressed as a function of the droplet pre- and post-impact velocity components normal to the impingement plane:

$$\Delta T_S = H_n \left[ \frac{1}{|\vec{u}_{n,o}|} + \frac{1}{|\vec{u}_{n,s}|} \right] \tag{128}$$

The parameter $H_n$ denotes the perpendicular distance between the impingement plane and the locations at which the pre- and post-impact velocities are referenced. Clearly, the collision contact time is a direct function of the proximity between the impingement plane and the reference locations and a physically accurate value may only be obtained in the limit as $H_n$ approaches zero.

As the finite element method discretizes a physical space into a finite number of computational sub spaces or elements, the droplet velocity is only available at a finite number of locations within the computational domain. Since the droplet velocity at nodes located on the impingement plane cannot simultaneously be equal to its pre- and post-impact values, the optimal value of $H_n$ is limited to the perpendicular distance between the impingement plane and the first layer of nodes off the impingement plane.

In addition to making potentially crude approximations regarding a representative value of $H_n$, the definition of the collision contact time as a function of pre- and post-impact

droplet velocities is inherently grid dependent. As such a formulation is considered inappropriate for the intended application, a suitable empirical model based on impact characteristics is required. However, the published literature reveals little information pertaining to the contact time involved in droplet-wall collisions, especially at impact velocities representative of aircraft icing conditions, and hence only the most relevant model is introduced. In a recent study, Okumura et al [43] relate the maximal deformation $\Delta d$ experienced by a droplet undergoing a fully elastic collision with a solid surface to its pre-impingement normal velocity component:

$$\Delta d \sim u_{n.o}\sqrt{\frac{\rho_d d_o^3}{8\sigma}} \tag{129}$$

An order of magnitude estimate for the collision contact time may be deduced based on the assumption that $\Delta T_S \sim \Delta d/u_{n,o}$ :

$$\Delta T_S \sim \sqrt{\frac{\rho_d d_o^3}{8\sigma}} \tag{130}$$

The functionality of Equation (130) as proposed by Okumura et al [43] suggests that the collision contact time increases with increasing droplet size, that is large droplets tend to remain in contact with the impact surface for a longer period of time than small droplets. Consequently, the body force accounting for droplet-wall interactions as defined by Equation (123) decreases with increasing droplet size, suggesting that large droplets featuring high impact velocities are subject to relatively low collision forces while small droplets featuring low impact velocities are subject to relatively high collision forces.

While Okumura et al [43] empirically confirm the analytically derived functionality of Equation (130) near the elastic collision limit of $We_s \approx 1$, the proposed tendency may be considered unphysical due to the decidedly inelastic character of droplet-wall collisions at impact velocities exceeding the experimental limit of $u_{n,o} \leq 1 m/s$. Hence a calibration of the collision contact time's variation with droplet diameter against experimental data is required prior to its inclusion in the proposed mathematical formulation of the droplet-wall interaction process.

# 5.1 Calibration Test Case

The most physically comprehensive collection of experimental data pertaining to SLD specific droplet-wall interactions originates from a recent study performed by Papadakis et al [44] at NASA Glenn's Icing Research Tunnel. Published in 2004, this detailed set of experimental data facilitates a systematic approach to the calibration of the proposed mathematical model over a large range of artificially generated droplet size distributions featuring MVDs of 20 $\mu$m, 52 $\mu$m, 111 $\mu$m, 154 $\mu$m and 236 $\mu$m.

The experimental test geometry consists of a NACA 23012 airfoil of 0.9144 m chord and 1.8288 m span, which is mounted vertically in a wind tunnel of 1.8288 m height and 2.7432 m width. Rather than meshing the experimental geometry in its entirety for numerical simulation purposes, merely the airfoil geometry is surrounded by a hexahedral C-Grid as illustrated in Figure 5-1. Comprised of 53504 hexahedral elements and 108208 nodes, the mesh may appear excessively dense for the purpose of droplet impingement simulations. However, in keeping with the previously introduced modular simulation methodology, the mesh is also used for the solution of the Navier-Stokes equations by FENSAP$^{TM}$, requiring a sufficiently fine spatial resolution in the vicinity of the airfoil contour in order to accurately capture the aerodynamic boundary layer.

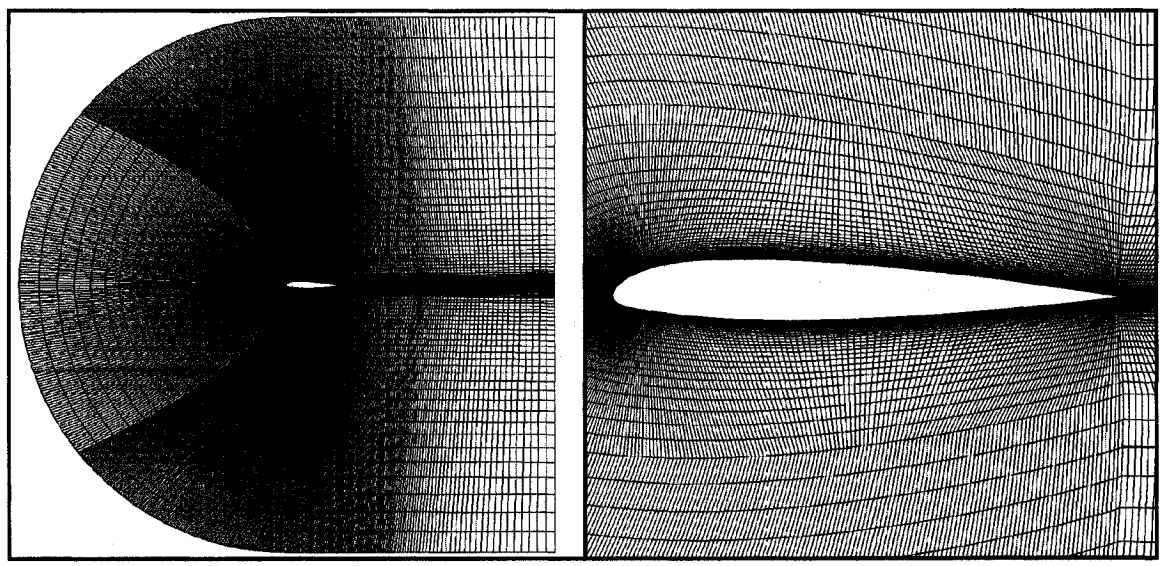

**Figure 5-1: Hexahedral C-Grid Surrounding NACA 23012 Airfoil**

## 5.2 Experimental Conditions

Papadakis et al [44] identify the following set of aerodynamic boundary conditions to characterize the mainstream flow around the NACA 23012 airfoil contour:

- Free stream velocity: $U_\infty$ = 78.23 m/s
- Free stream temperature: $T_\infty$ = 299.00 K
- Free stream pressure: $p_\infty$ = 101.33 kPa
- Geometric angle of attack: $AoA$ = 2.50 °
- Gravitational acceleration: $\vec{g}$ = {0,0,-9.81} $m/s^2$

Due to the airfoil's vertical orientation within the wind tunnel, the gravitational acceleration vector is oriented along the airfoil's spanwise direction. Based on these inlet conditions, a chordwise Reynolds number of approximately 4.80e6 is obtained within the test section of the icing research tunnel. The droplet diameters and associated volumetric fractions corresponding to 10 and 27 bin approximations of the experimental droplet size distributions are listed in Table 5-1 and Table 5-2, respectively.

**Table 5-1: 10 Bin Approximations of Experimental Droplet Size Distributions [44]**

| I | $P_I$ (%) | DROPLET DIAMETER ($\mu$m) | | | | |
|---|---|---|---|---|---|---|
| | | MVD 20 | MVD 52 | MVD 111 | MVD 154 | MVD 236 |
| 1 | 5.0 | 3.85 | 6.69 | 11.05 | 13.88 | 16.25 |
| 2 | 10.0 | 9.39 | 16.88 | 27.48 | 44.45 | 63.65 |
| 3 | 20.0 | 13.80 | 25.44 | 56.48 | 90.28 | 135.48 |
| 4 | 30.0 | 19.60 | 59.17 | 111.10 | 154.16 | 298.51 |
| 5 | 20.0 | 25.48 | 131.25 | 170.81 | 218.32 | 508.45 |
| 6 | 10.0 | 30.73 | 192.75 | 212.76 | 284.45 | 645.46 |
| 7 | 3.0 | 35.19 | 216.57 | 235.00 | 343.71 | 715.86 |
| 8 | 1.0 | 38.32 | 224.98 | 257.70 | 380.26 | 747.39 |
| 9 | 0.5 | 40.66 | 229.00 | 279.54 | 400.92 | 763.24 |
| 10 | 0.5 | 44.36 | 253.92 | 312.59 | 425.06 | 1046.76 |

**Table 5-2: 27 Bin Approximations of Experimental Droplet Size Distributions [44]**

| I | $P_I$ (%) | DROPLET DIAMETER ($\mu$m) | | | | |
|---|---|---|---|---|---|---|
| | | MVD 20 | MVD 52 | MVD 111 | MVD 154 | MVD 236 |
| 1 | 4.75 | 3.77 | 6.54 | 10.86 | 13.63 | 15.90 |
| 2 | 4.75 | 8.42 | 15.16 | 24.51 | 32.00 | 45.33 |
| 3 | 4.75 | 10.07 | 18.61 | 29.64 | 47.12 | 74.84 |
| 4 | 4.75 | 11.55 | 21.20 | 34.95 | 67.20 | 102.03 |
| 5 | 4.75 | 12.97 | 23.57 | 44.73 | 84.29 | 122.55 |
| 6 | 4.75 | 14.30 | 25.88 | 58.34 | 98.09 | 141.62 |
| 7 | 4.75 | 15.50 | 28.27 | 70.67 | 110.15 | 160.53 |
| 8 | 4.75 | 16.65 | 30.93 | 81.29 | 120.74 | 178.44 |
| 9 | 4.75 | 17.67 | 34.45 | 91.19 | 131.19 | 197.68 |
| 10 | 4.75 | 18.60 | 40.80 | 100.93 | 142.48 | 217.96 |
| 11 | 4.75 | 19.54 | 51.35 | 110.59 | 153.96 | 240.79 |
| 12 | 4.75 | 20.50 | 63.07 | 119.49 | 164.88 | 271.02 |
| 13 | 4.75 | 21.50 | 73.98 | 128.82 | 175.55 | 320.02 |
| 14 | 4.75 | 22.50 | 85.72 | 140.10 | 187.07 | 393.53 |
| 15 | 4.75 | 23.58 | 99.79 | 152.83 | 199.57 | 455.54 |
| 16 | 4.75 | 24.73 | 115.90 | 165.86 | 211.88 | 494.62 |
| 17 | 4.75 | 25.98 | 138.79 | 179.35 | 223.90 | 534.10 |
| 18 | 4.75 | 27.47 | 164.98 | 193.73 | 240.14 | 577.95 |
| 19 | 4.75 | 29.32 | 185.62 | 207.19 | 263.97 | 624.01 |
| 20 | 4.75 | 31.84 | 202.74 | 219.67 | 299.42 | 670.92 |
| 21 | 1.00 | 33.81 | 212.41 | 227.39 | 327.20 | 701.14 |
| 22 | 1.00 | 34.83 | 215.58 | 230.13 | 341.68 | 713.62 |
| 23 | 1.00 | 36.21 | 219.73 | 237.75 | 358.19 | 728.34 |
| 24 | 0.50 | 37.46 | 223.64 | 250.52 | 375.09 | 742.10 |
| 25 | 0.50 | 38.74 | 226.32 | 264.23 | 389.05 | 752.67 |
| 26 | 0.50 | 40.66 | 229.00 | 279.54 | 400.92 | 763.24 |
| 27 | 0.50 | 44.36 | 253.92 | 312.58 | 425.05 | 1046.76 |

# 5.3 Aerodynamics

The hexahedral mesh depicted in Figure 5-1 neglects the physical presence of the icing research tunnel's sidewalls and hence the associated aerodynamic influence on the flow field surrounding the NACA 23012 airfoil. Consequently, a numerical simulation of the flow based on a geometric angle of attack equal to 2.50° yields pressure and velocity distributions around the airfoil that differ from experimental conditions. In order to alleviate this discrepancy, the aerodynamic effects of the wind tunnel may be addressed by means of an effective angle of attack, determined through numerical experimentation so as to match the empirically established pressure coefficient distribution on the airfoil. Figure 5-2 demonstrates a good agreement between the experimentally observed pressure coefficient distribution and the numerical equivalent obtained from a FENSAP$^{TM}$ simulation at an effective angle of attack equal to 3.00°.

Please refer to Figures 5-3 and 5-4 for an illustration of the pressure and Mach number contours around the NACA 23012 airfoil at a geometric angle of attack of 2.50°.

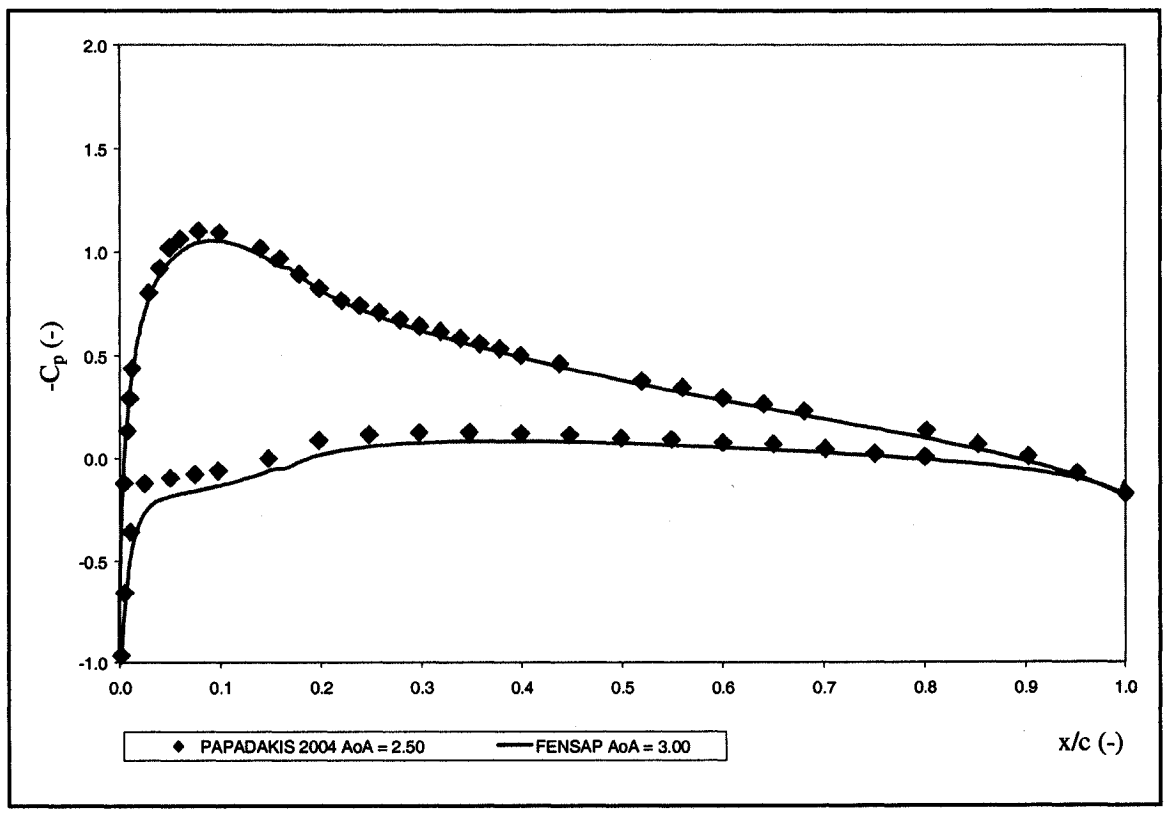


**Figure 5-2: Pressure Coefficient Distribution for NACA 23012 Airfoil at AoA=2.50°**

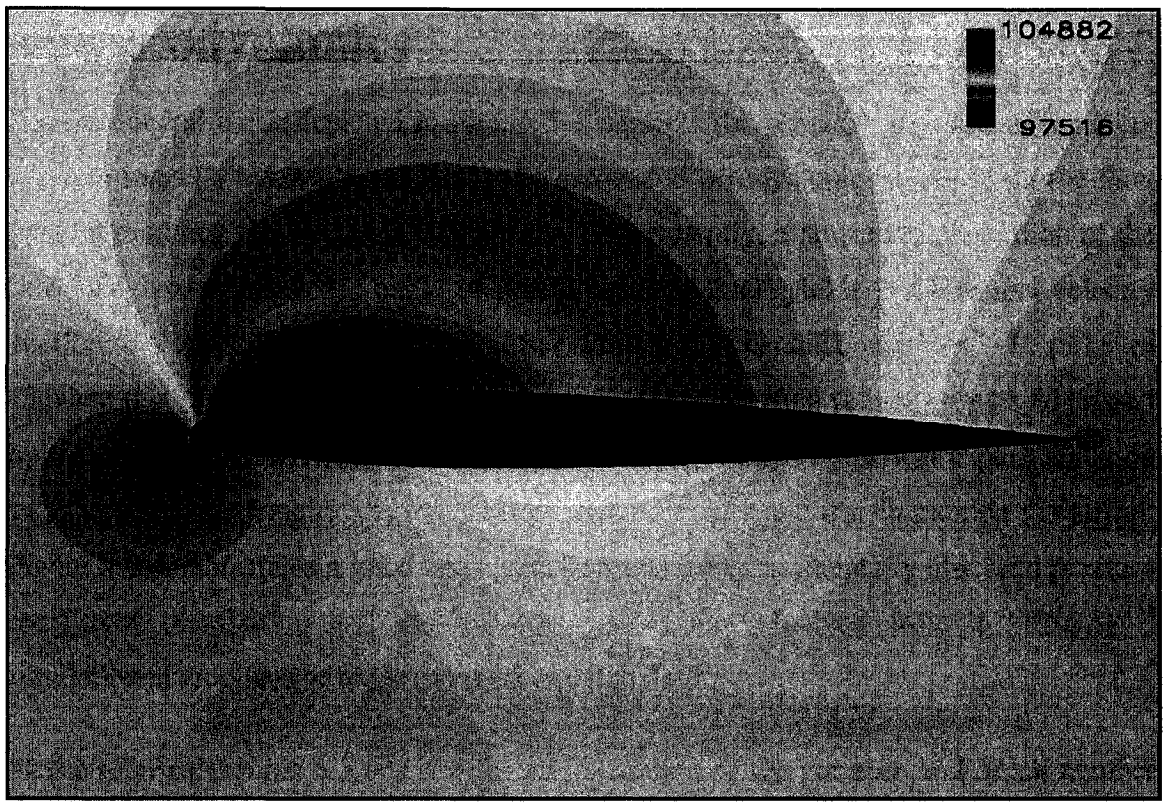


**Figure 5-3: Pressure Contours for NACA 23012 Airfoil at AoA=2.50°**

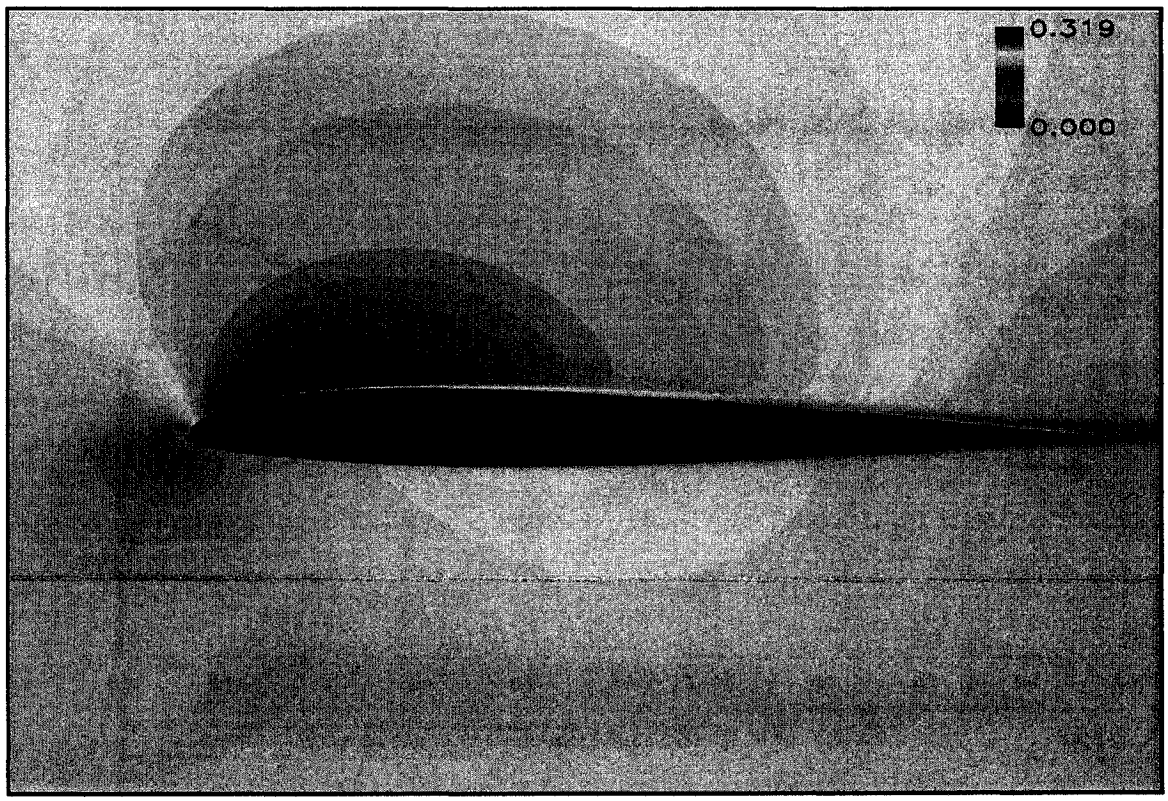


**Figure 5-4: Mach Number Contours for NACA 23012 Airfoil at AoA=2.50°**

# 5.4 Droplet Impingement

Having identified the need to calibrate the functionality of the variation of collision contact time with incident droplet diameter, a systematic approach is taken so as to render the proposed mathematical model applicable over the wide range of droplet sizes employed by Papadakis et al [44]. An initial estimate for the desired functionality may be made based on the arbitrary assumption that the collision contact time approaches a constant value for droplets larger than a certain critical droplet size $d_{ref}$, while the collision contact time increases super linearly with incident droplet diameter up to $d_{ref}$. Furthermore, it is reasonable to assume that droplets smaller than a certain critical size $d_{min}$ will not be subject to the effects of droplet-wall interactions, generally accepted to be the case for droplet size distributions within the extents of the Appendix C envelope. The resulting functionality may thus be expressed as follows:

$$\Delta T_S = K_T \left[ \frac{\rho_d d_{ref}^3}{8\sigma} \right]^{\frac{1}{2}} \left[ \frac{d_{ref}}{d_o} \right]^n \Rightarrow n = \begin{Bmatrix} 3.0 & d_{\min} \le d_o < d_{ref} \\ 0.0 & d_o \ge d_{ref} \end{Bmatrix} \tag{131}$$

Considering the experimental range of mean volumetric diameters from 20 $\mu$m to 236 $\mu$m, the value of $d_{ref}$ is chosen to equal 120 $\mu$m as this value corresponds to the approximate median of the empirical range of droplet size distributions while the value of $d_{min}$ is chosen to equal 30 $\mu$m. Furthermore, preliminary numerical experimentation suggests the following values for $K_T$:

$$K_T = \begin{Bmatrix} 6.5 & R_1 \\ 6.0 & R_2 \end{Bmatrix} \tag{132}$$

At this point, a numerical simulation of the droplet impingement process based on the proposed mathematical model of droplet-wall interactions may be facilitated. In order to demonstrate the applicability and importance of the droplet bouncing and splashing mechanisms, numerically simulated collection efficiency distributions based on a consideration of droplet splashing (DROP3D 2005 A) are compared to numerical results based on a consideration of both splashing and bouncing (DROP3D 2005 B) as well as numerical results obtained in the absence of droplet-wall interactions (DROP3D 2004) and experimental results (PAPADAKIS 2004) in Figures 5-5 through 5-8.

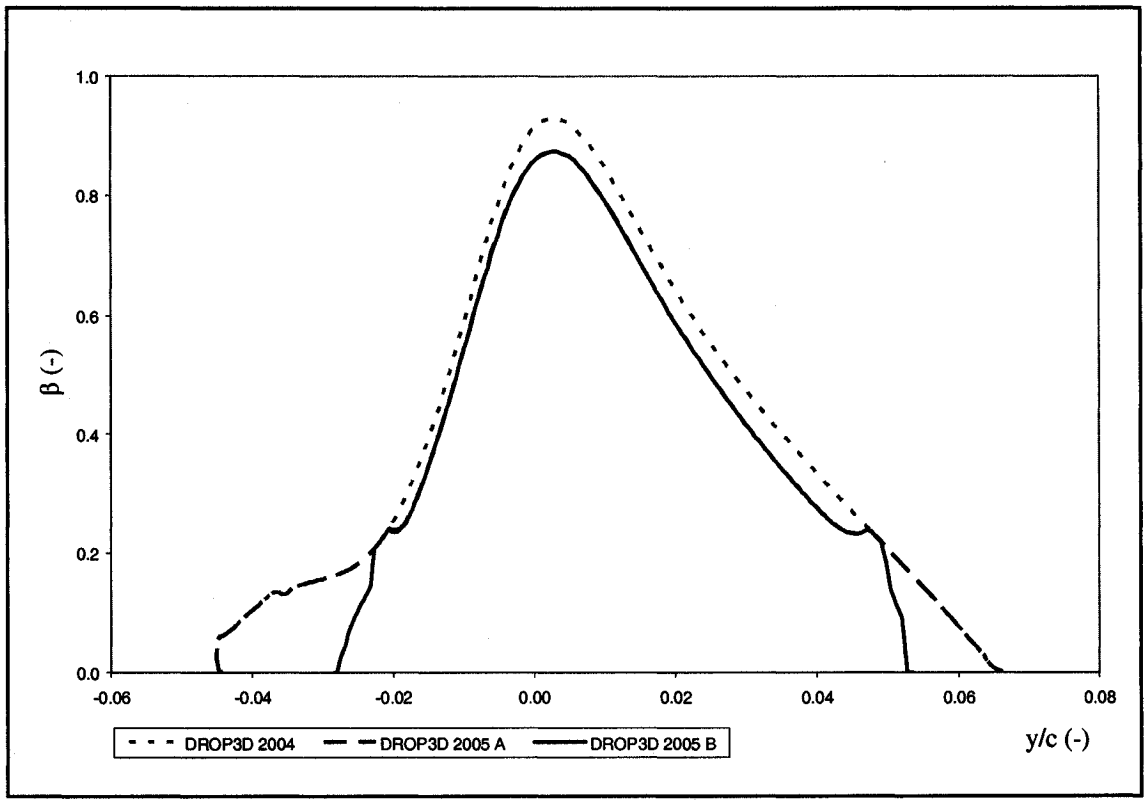


**Figure 5-5: Collection Efficiency for NACA 23012 Airfoil at $d_o$=111 μm**

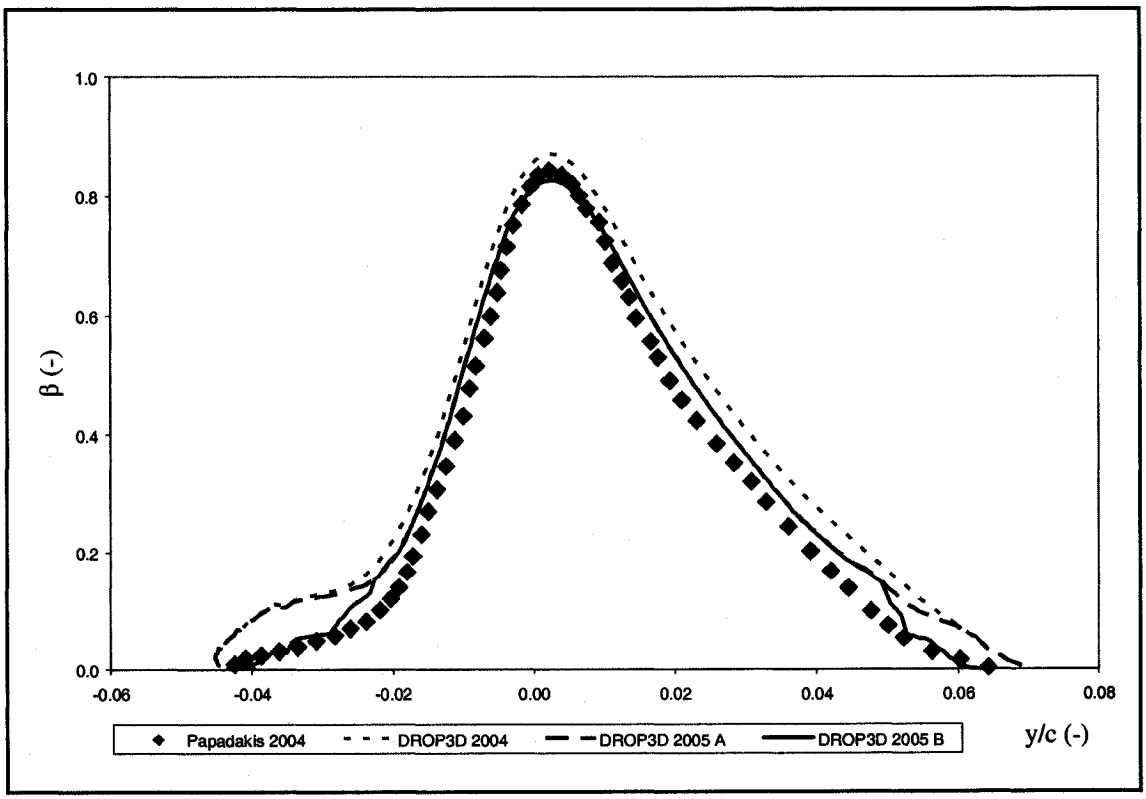


**Figure 5-6: Collection Efficiency for NACA 23012 Airfoil at MVD=111 μm, 10 Bin Distribution**

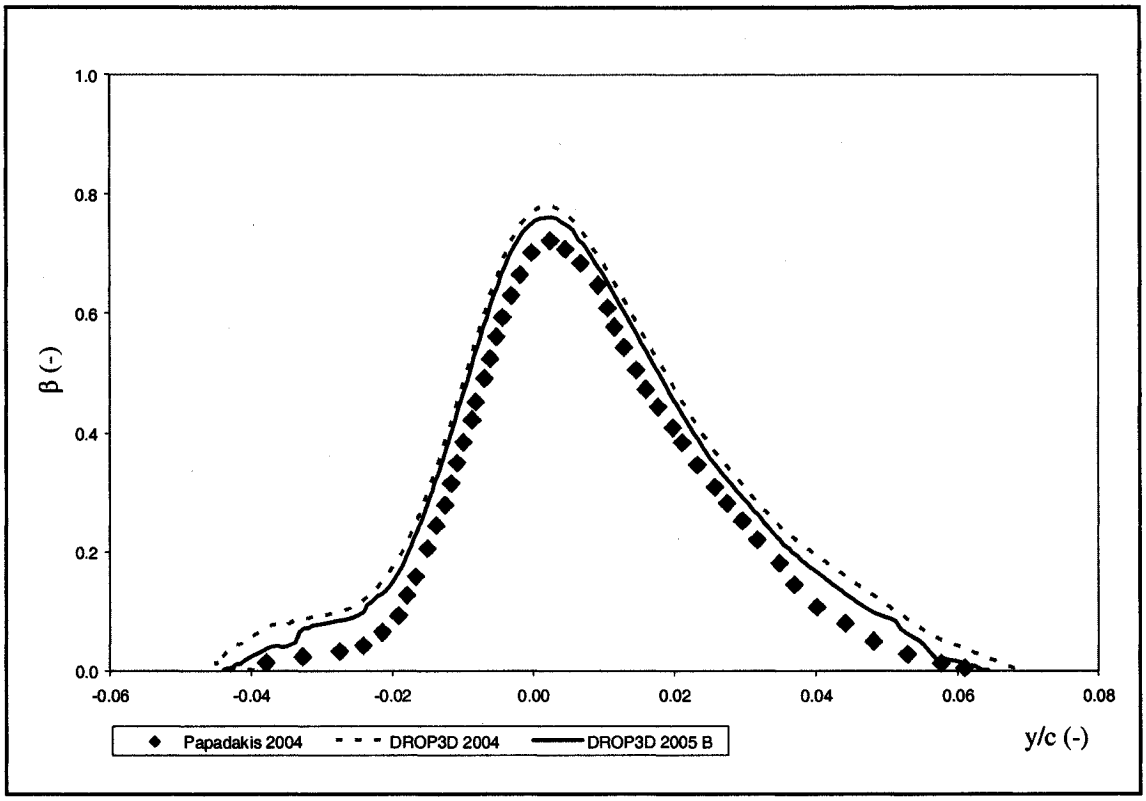


**Figure 5-7: Collection Efficiency for NACA 23012 Airfoil at MVD=52 μm, 10 Bin Distribution**

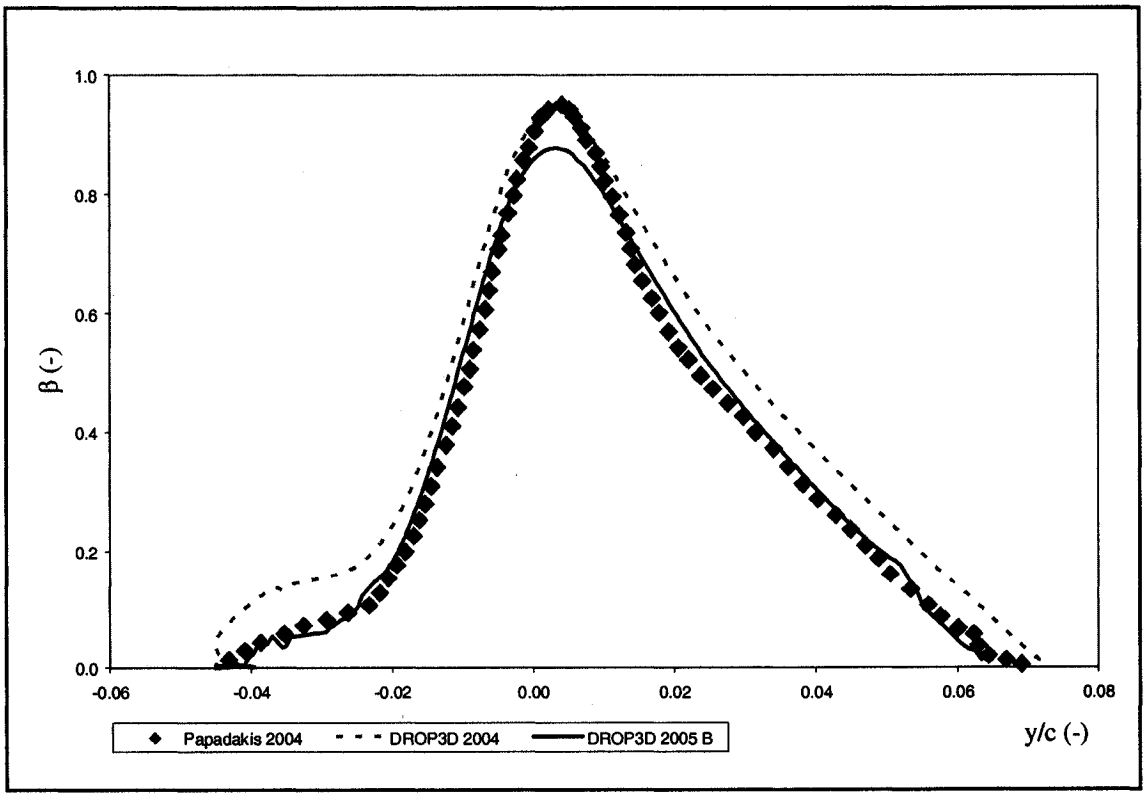


**Figure 5-8: Collection Efficiency for NACA 23012 Airfoil at MVD=236 μm, 10 Bin Distribution**

A comparison of the collection efficiency distributions presented in Figure 5-6 reveals an important aspect regarding the proposed mathematical model's ability to simulate the effects of droplet-wall interactions. While delivering more physically accurate results than the original mathematical model, a consideration of droplet splashing alone merely suffices to describe the mass loss incurred near the airfoil's leading edge. An increasing deviation between numerical and experimental results may be observed as the impingement limits are approached, strongly suggesting the consideration of droplet bouncing in addition to droplet splashing in order to comply with experimental results. The collection efficiency distributions depicted in Figure 5-5 are based on a single droplet size equal to 111 $\mu$m rather than being based on a 10 bin droplet size distribution around an MVD of 111 $\mu$m as is the case for the numerical results presented in Figure 5-6. While a comparison to experimental results cannot be made for a single droplet size due to the multi-dispersed nature of the empirical droplet distributions, Figure 5-5 serves well to demonstrate the considerable amount of mass loss attributable to droplet bouncing near the impingement limits.

Having considered numerical results based on an MVD in the vicinity of the median value of the empirical droplet size range, an analysis of numerical results based on extreme MVD values becomes necessary. An inspection of the collection efficiency distributions based on an MVD of 52 $\mu$m as presented in Figure 5-7 reveals insufficient mass loss throughout the impingement region. In contrast, an analysis of the collection efficiency distributions based on an MVD of 236 $\mu$m as presented in Figure 5-8 suggests excessive mass loss near the airfoil leading edge while good agreement between numerical and experimental results is observed throughout the remainder of the impingement region. As may be appreciated, a resolution of these deficiencies by means of a simple recalibration of the collision contact time is not obvious. While an increase in mass loss throughout the impingement region alleviates the discrepancy between numerical and experimental results currently observed at an MVD of 52 $\mu$m, it aggravates the excessive mass loss due to splashing incurred near the airfoil leading edge currently observed at an MVD of 236 $\mu$m and vice versa. Therefore, the need to regulate the extent of mass loss due to splashing is addressed prior to a further calibration of the

collision contact time. A possible means to govern the mass loss due to splashing presents itself in the explicit availability of the splashed to incident mass ratio $f_m$ in the proposed mathematical model. However, a simple adjustment of the coefficients in Equation (110) does not alleviate the deficiency at hand as an overall change in the splashed mass ratio inherently affects the mass loss incurred throughout the impingement region. Therefore, a modification of the functionality of the splashed to incident mass ratio is proposed to address the excessive mass loss observed at high impact locations:

$$f_m = \frac{m_s}{m_o} = \begin{Bmatrix} 1.0 & R_1 \\ 3.8\left[1.0 - e^{-0.85(K_Y' - 17)}\right] / \left[K_Y'\right]^{0.5} & R_2 \end{Bmatrix} \tag{133}$$

Figures 5-9 through 5-11 compare collection efficiency distributions based on the consideration of Equation (133) rather than Equation (110) in the proposed mathematical model (DROP3D 2005 C) with numerical results based on the original mathematical model (DROP3D 2004) as well as experimental results (PAPADAKIS 2004).

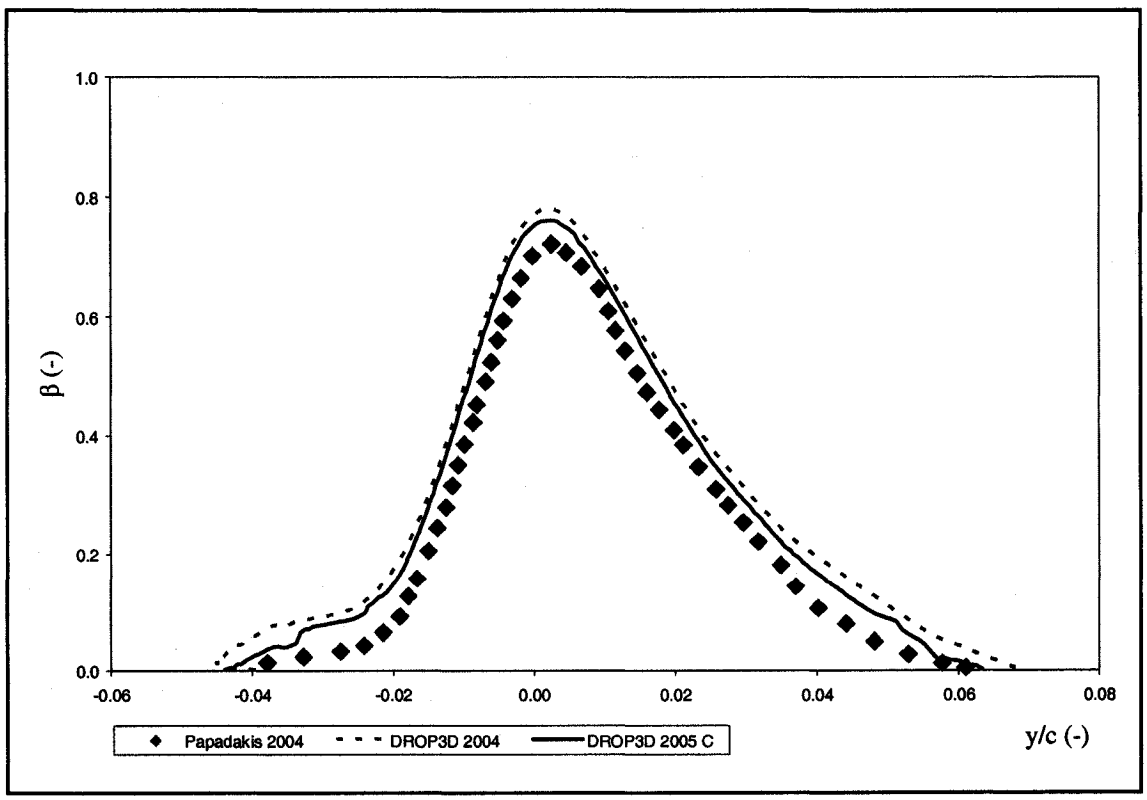


**Figure 5-9: Collection Efficiency for NACA 23012 Airfoil at MVD=52 μm, 10 Bin Distribution**

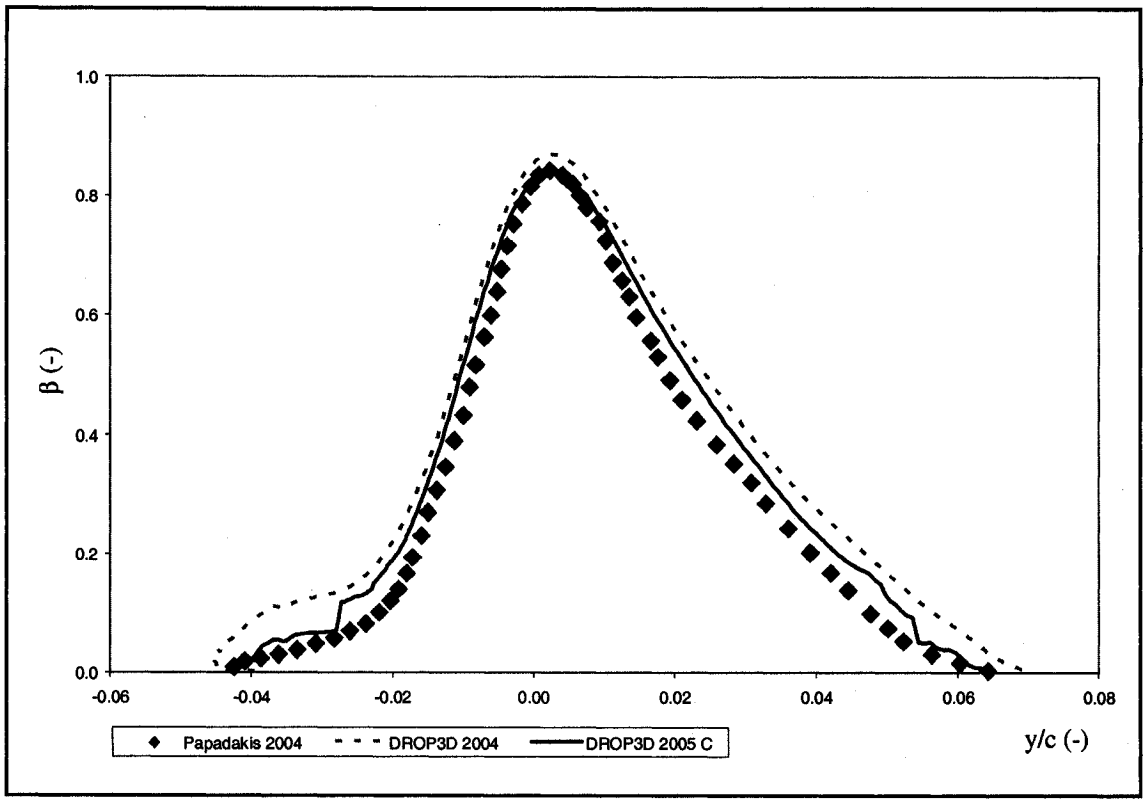


**Figure 5-10: Collection Efficiency for NACA 23012 Airfoil at MVD=111 μm, 10 Bin Distribution**

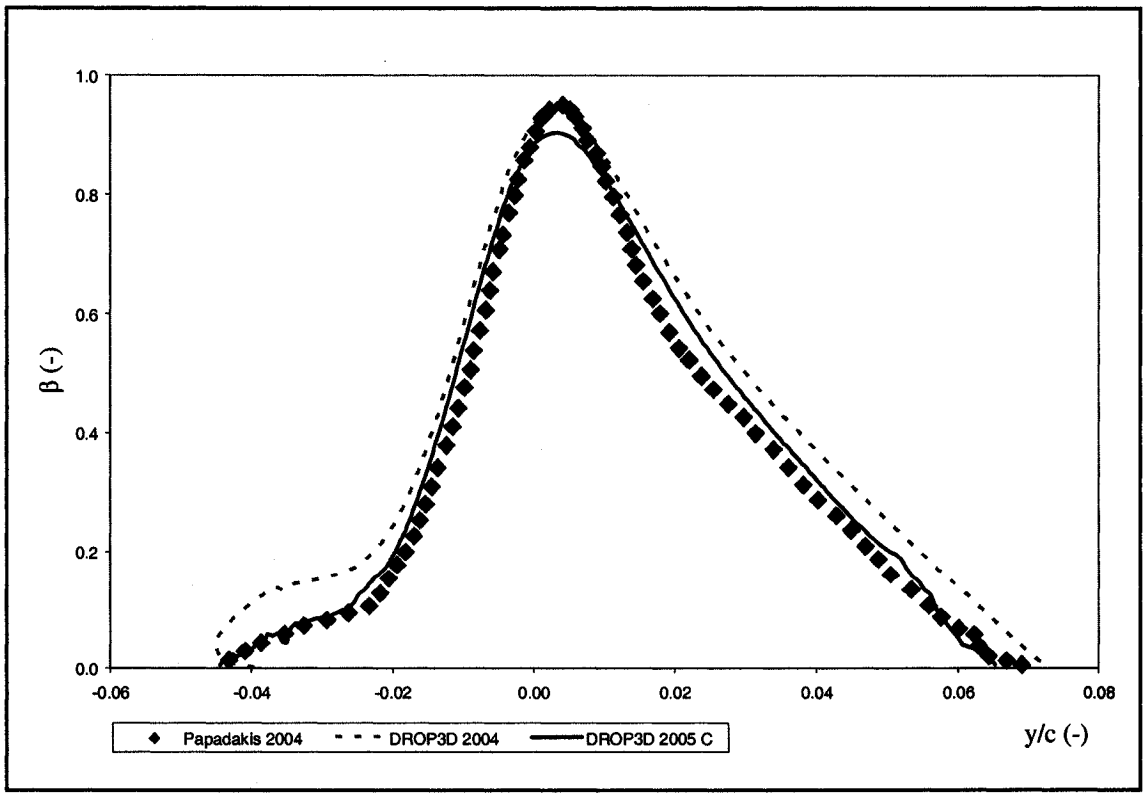


**Figure 5-11: Collection Efficiency for NACA 23012 Airfoil at MVD=236 μm, 10 Bin Distribution**

A comparison of Figures 5-9 and 5-7 as well as Figures 5-10 and 5-6 reveals virtually unaltered collection efficiency distributions at MVDs of 52 μm and 111 μm, irrespective of the particular functionality of $f_m$. However, a comparison of Figures 5-11 and 5-8 reveals the desired reduction in mass loss in the vicinity of the airfoil leading edge while the collection efficiency throughout the remainder of the impingement region remains unaltered. Even though the accomplished reduction in mass loss does not suffice to provide numerical results in complete agreement with experimental data, it is considered reasonable. Furthermore, it should be noted that the maximum collection efficiency observed in the experiment exceeds the maximum collection efficiency obtained from numerical simulations in the absence of droplet-wall interactions. At this point it is unclear whether this discrepancy is attributable to the original mathematical model or a deficiency in the experimental measurement methods, which produce fluctuations in the value of the maximum collection efficiency by up to 10% as reported by Papadakis et al [44]. In any case, it would appear sensible that the maximum collection efficiency obtained under consideration of droplet-wall interactions should not exceed the value obtained without the consideration of mass loss. As such, the proposed mathematical model may be considered mathematically consistent and physically representative.

Having resolved the issue of excessive leading edge mass loss incurred by large droplets, the deficiency of generally insufficient mass loss observed for small droplets must be addressed through a modification of the proposed functionality of the collision contact time. The previous assumption regarding the super linear variation of the collision contact time with incident droplet diameters smaller than $d_{ref}$ may be considered unjustified, and detailed numerical experimentation suggests the following functionality:

$$\Delta T_S = K_T \left[ \frac{\rho_d d_{ref}^3}{8\sigma} \right]^{\frac{1}{2}} \left[ \frac{d_{ref}}{d_o} \right]^n \Rightarrow n = \begin{Bmatrix} 0.2 & d_{\min} \le d_o < d_{ref} \\ 0.0 & d_o \ge d_{ref} \end{Bmatrix} \tag{134}$$

Figures 5-12 through 5-14 compare collection efficiency distributions based on the consideration of Equation (134) rather than Equation (131) in the proposed mathematical model (DROP3D 2005) with numerical results based on the original mathematical model (DROP3D 2004) as well as experimental results (PAPADAKIS 2004).

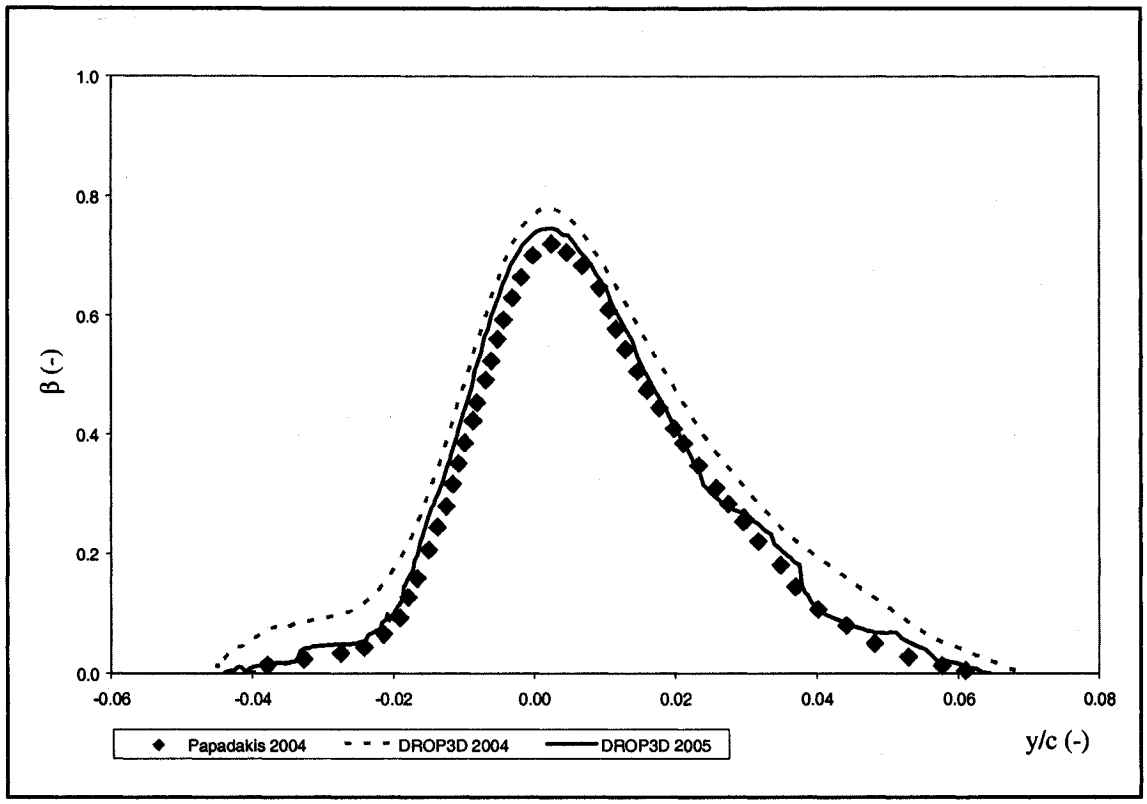


**Figure 5-12: Collection Efficiency for NACA 23012 Airfoil at MVD=52 μm, 10 Bin Distribution**

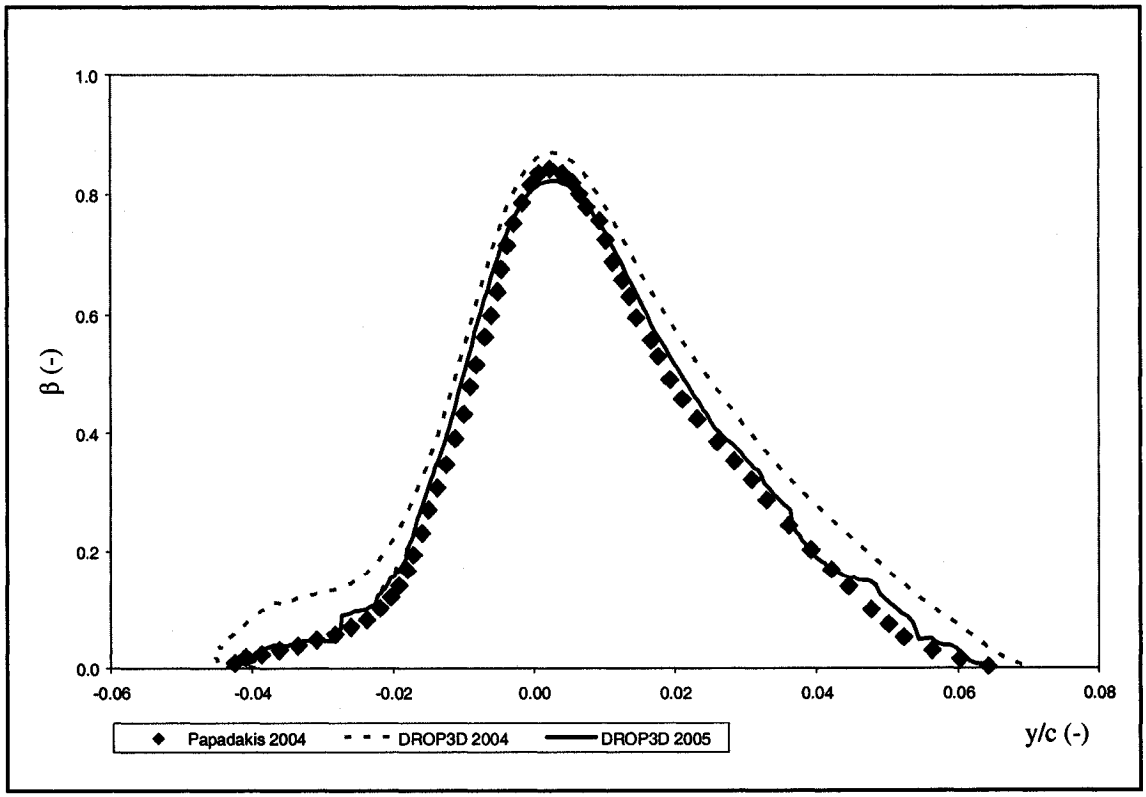


**Figure 5-13: Collection Efficiency for NACA 23012 Airfoil at MVD=111 μm, 10 Bin Distribution**

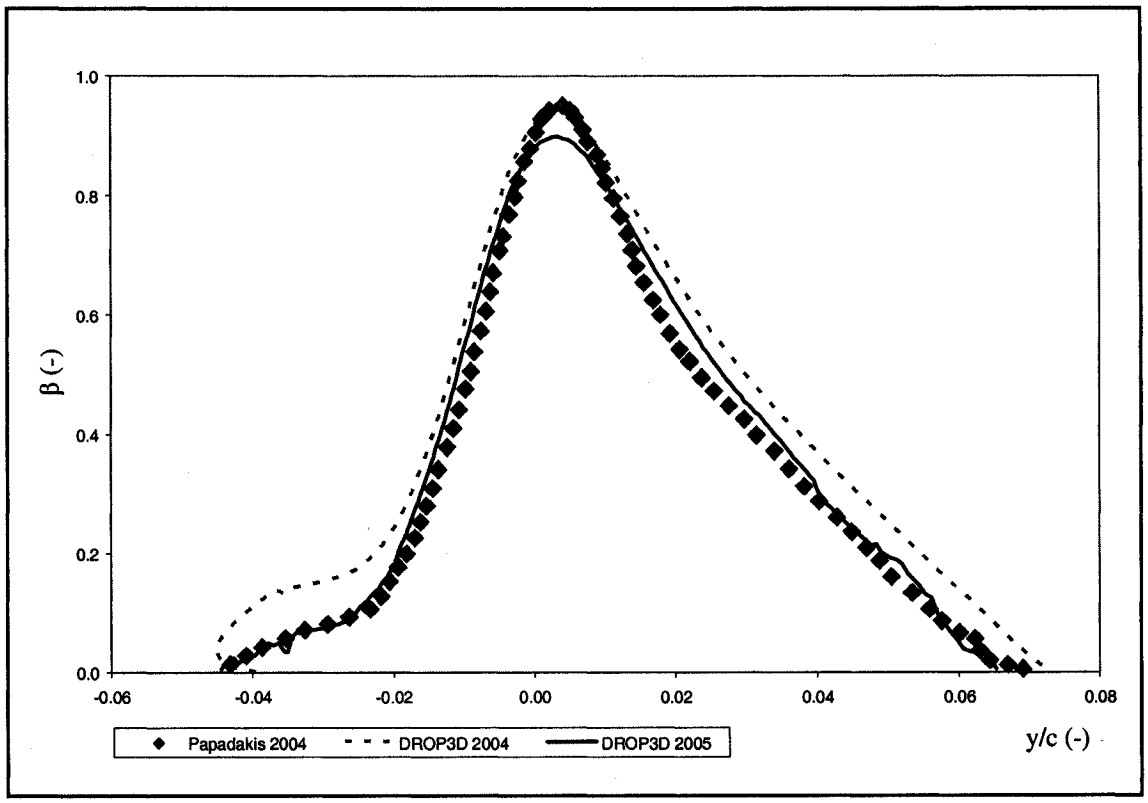


**Figure 5-14: Collection Efficiency for NACA 23012 Airfoil at MVD=236 μm, 10 Bin Distribution**

An inspection of Figures 5-12 through 5-14 reveals a generally good agreement between numerical and experimental results for the given empirical droplet size distributions. However, the collection efficiency distributions feature slight profile irregularities which may be attributable to the discontinuous mass loss gradient observed in the region between droplet splashing and bouncing regimes as previously illustrated in Figure 5-5. In the case of a 10 bin approximation of the empirical droplet distribution around and MVD of 52 μm, the onset of droplet bouncing occurs between bins 3 and 4, respectively representing 20% and 30% of the total droplet phase. Based on a 27 bin approximation, however, the onset of droplet bouncing occurs between bins 7 and 8, each representing only 4.75% of the total droplet phase.

Hence, numerical simulations based on 27 bin approximations are likely to provide a more regular collection efficiency profile than those based on 10 bin approximations of the corresponding empirical droplet distribution, as illustrated in Figures 5-15 through 5-19 for the full range of droplet sizes investigated by Papadakis et al [44].

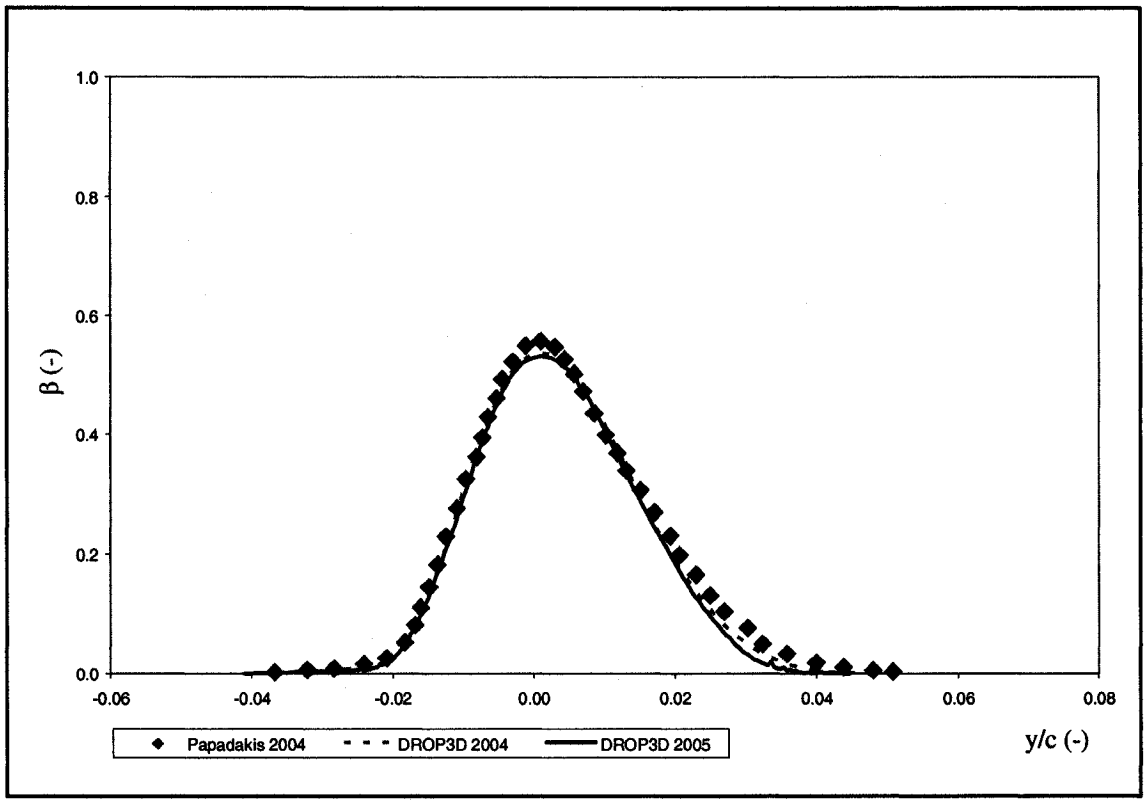


**Figure 5-15: Collection Efficiency for NACA 23012 Airfoil at MVD=20 μm, 27 Bin Distribution**

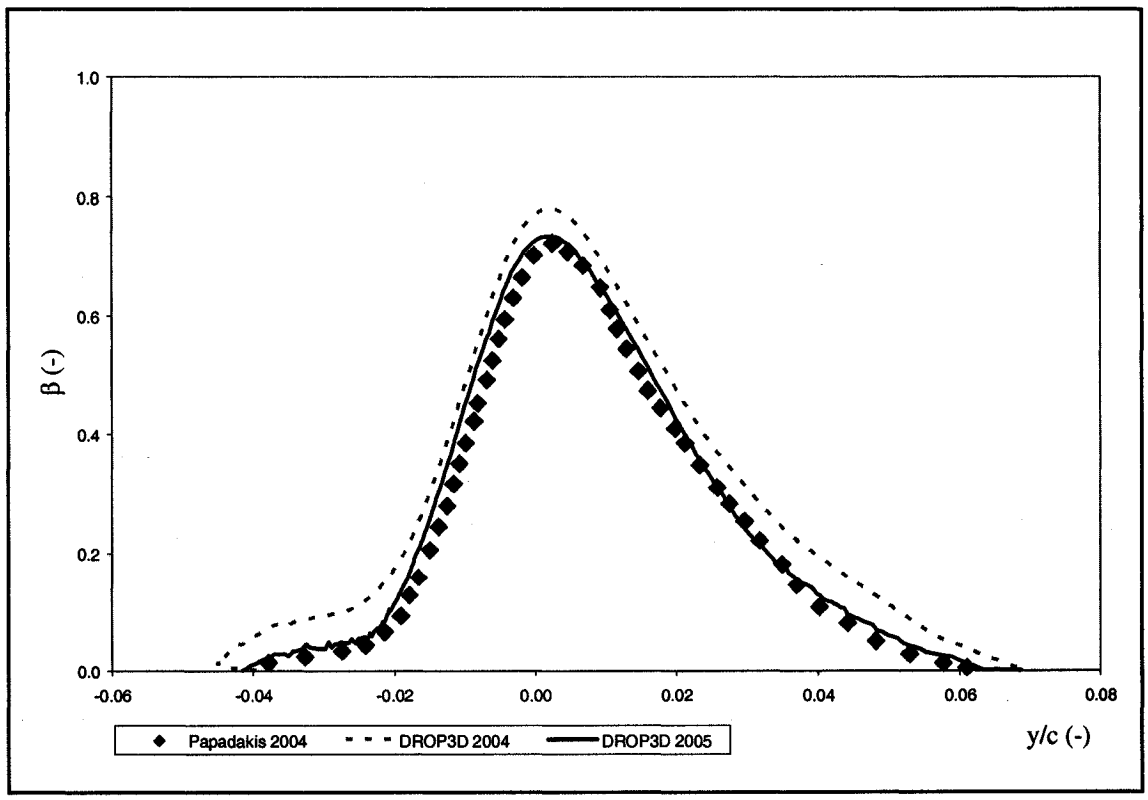


**Figure 5-16: Collection Efficiency for NACA 23012 Airfoil at MVD=52 μm, 27 Bin Distribution**

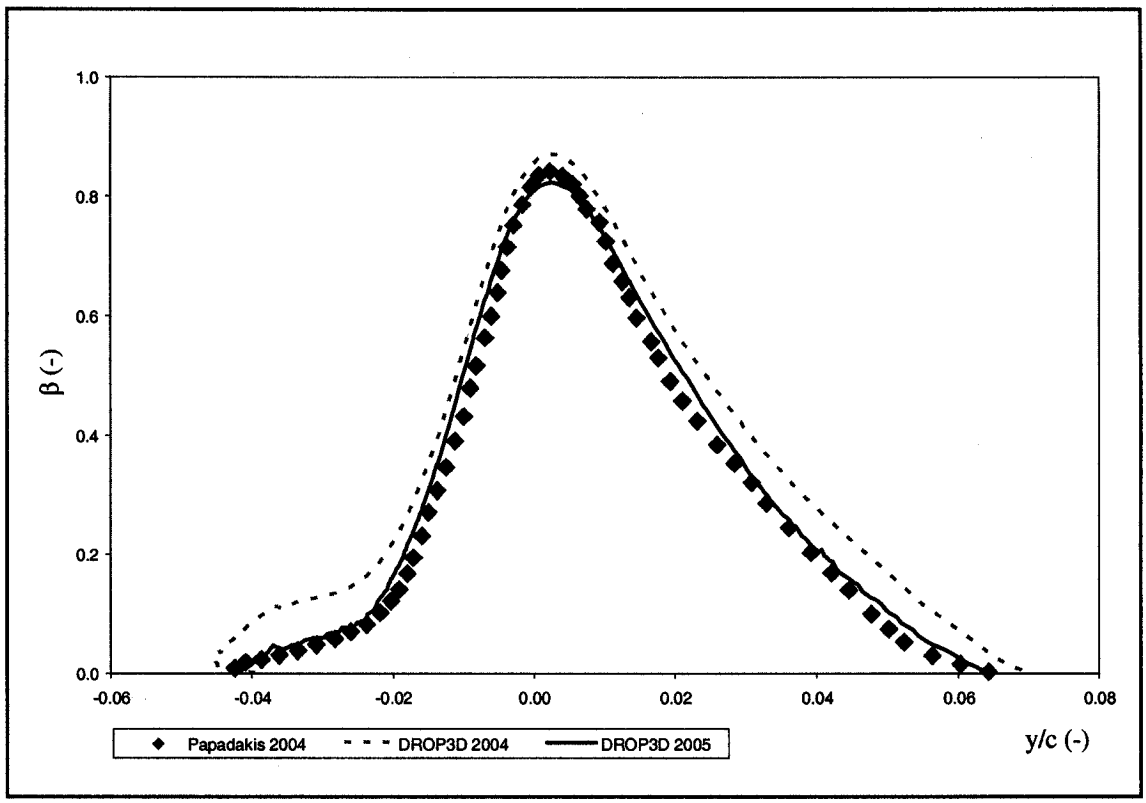


**Figure 5-17: Collection Efficiency for NACA 23012 Airfoil at MVD=111 μm, 27 Bin Distribution**

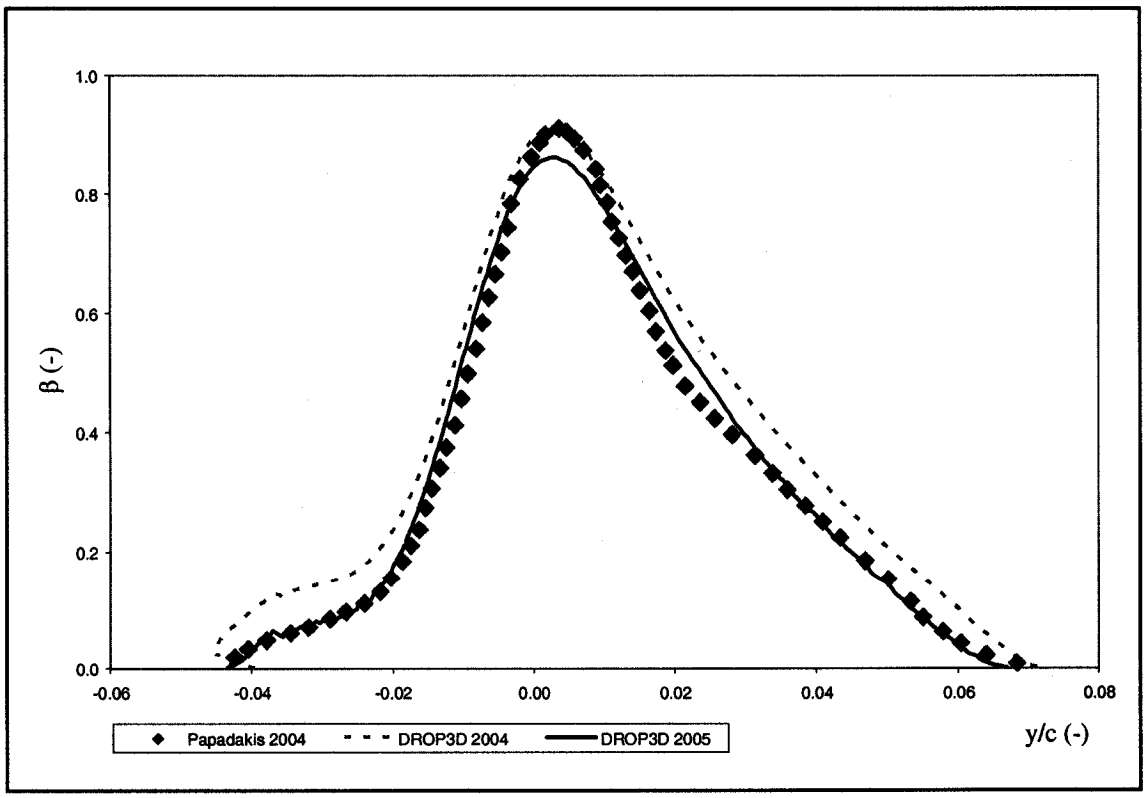


**Figure 5-18: Collection Efficiency for NACA 23012 Airfoil at MVD=154 μm, 27 Bin Distribution**

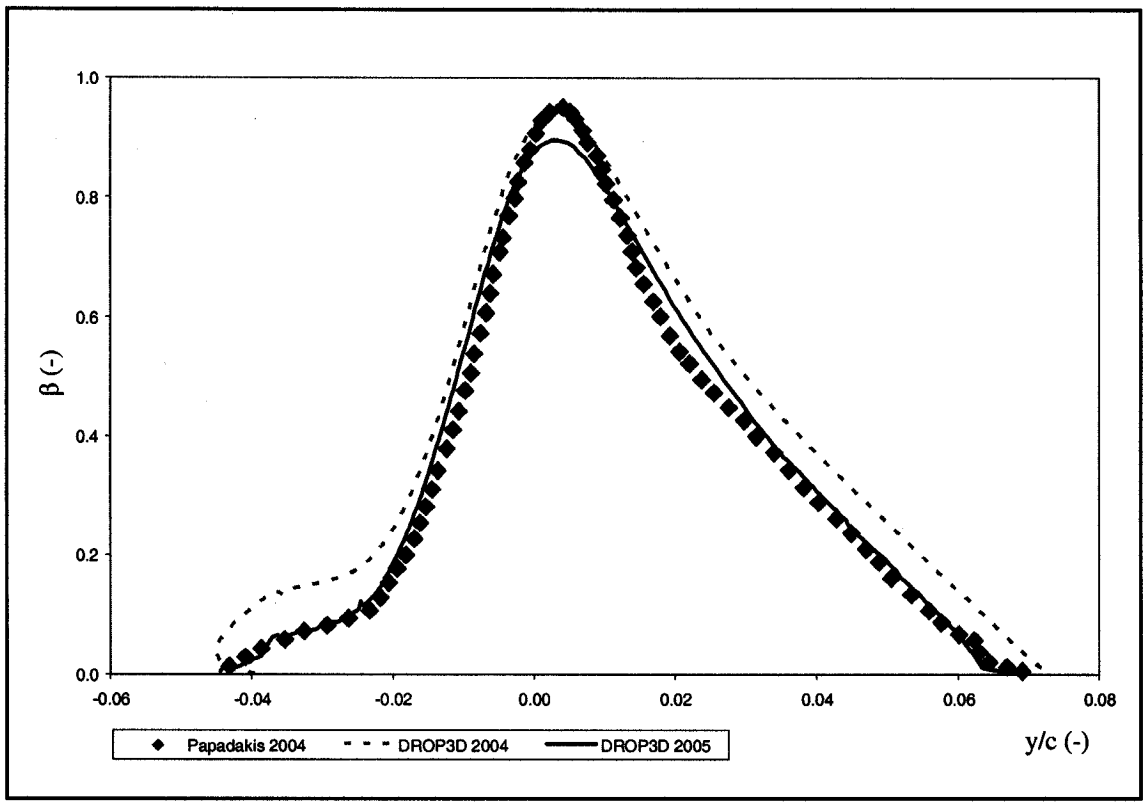


**Figure 5-19: Collection Efficiency for NACA 23012 Airfoil at MVD=236 μm, 27 Bin Distribution**

A review of Figures 5-15 through 5-19 confirms the expected improvement in quality associated with numerical results based on a more accurate approximation of the experimental droplet distributions. Excellent agreement between numerical and experimental collection efficiency distributions is observed throughout the droplet impingement region at MVDs of 20 μm, 52 μm and 111 μm, while the previously discussed deviation from experimental data within the vicinity of the airfoil leading edge becomes increasingly apparent at elevated MVDs of 154 μm and 236 μm. Considering the overall quality of the numerical results, however, the calibration of the proposed mathematical model of droplet-wall interactions may be deemed complete at this point.

While the preceding quantitative analysis of collection efficiency distributions serves well to verify the proposed formulation's modeling capabilities, a qualitative investigation of the liquid water content around the airfoil as presented in Figures 5-20 through 5-29 aids in the demonstration of the effects of droplet splashing and bouncing on aircraft surfaces located downstream of a droplet's primary impingement location.

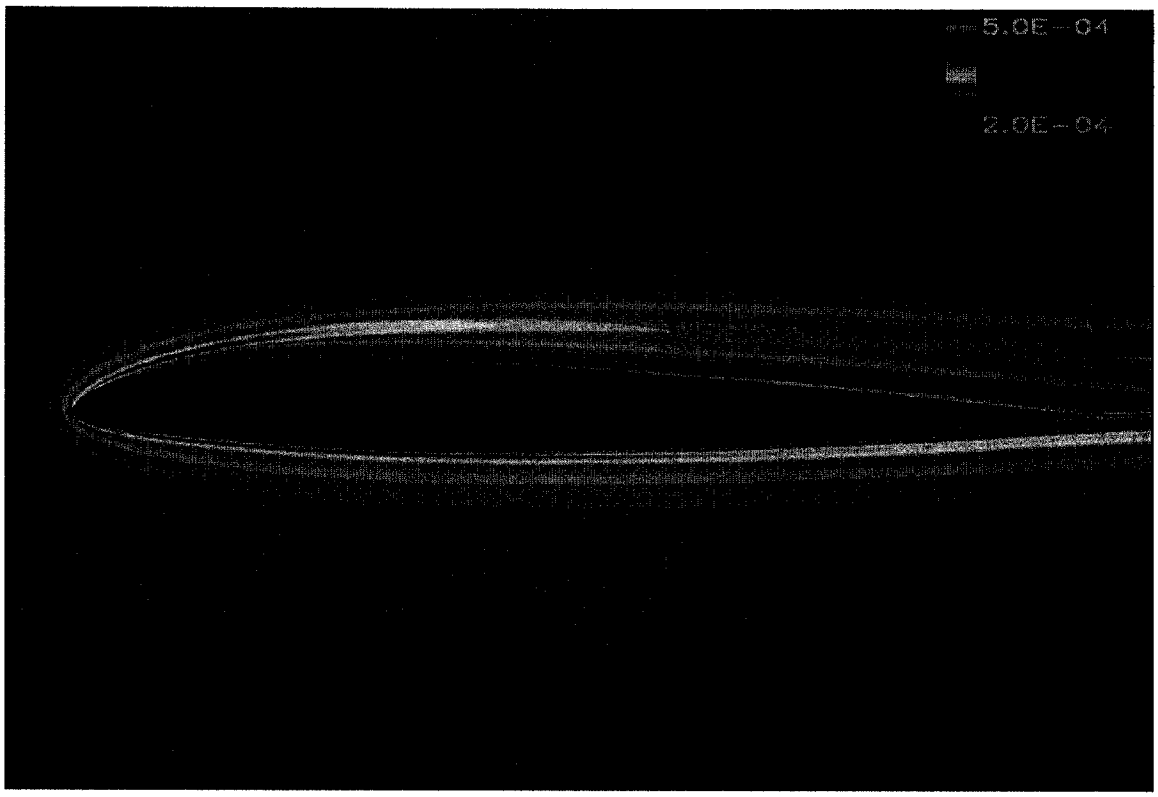


**Figure 5-20: LWC Distribution for NACA 23012 Airfoil at MVD=20 μm, DROP3D 2004**

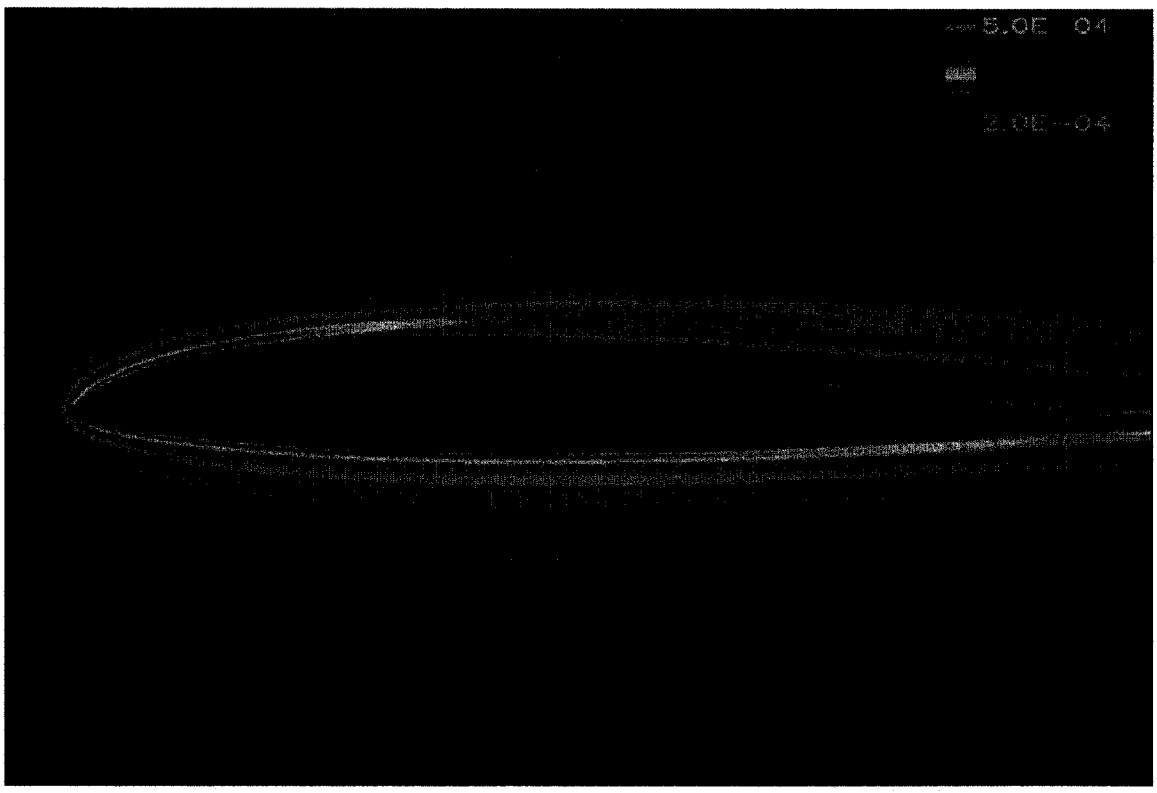


**Figure 5-21: LWC Distribution for NACA 23012 Airfoil at MVD=20 μm, DROP3D 2005**

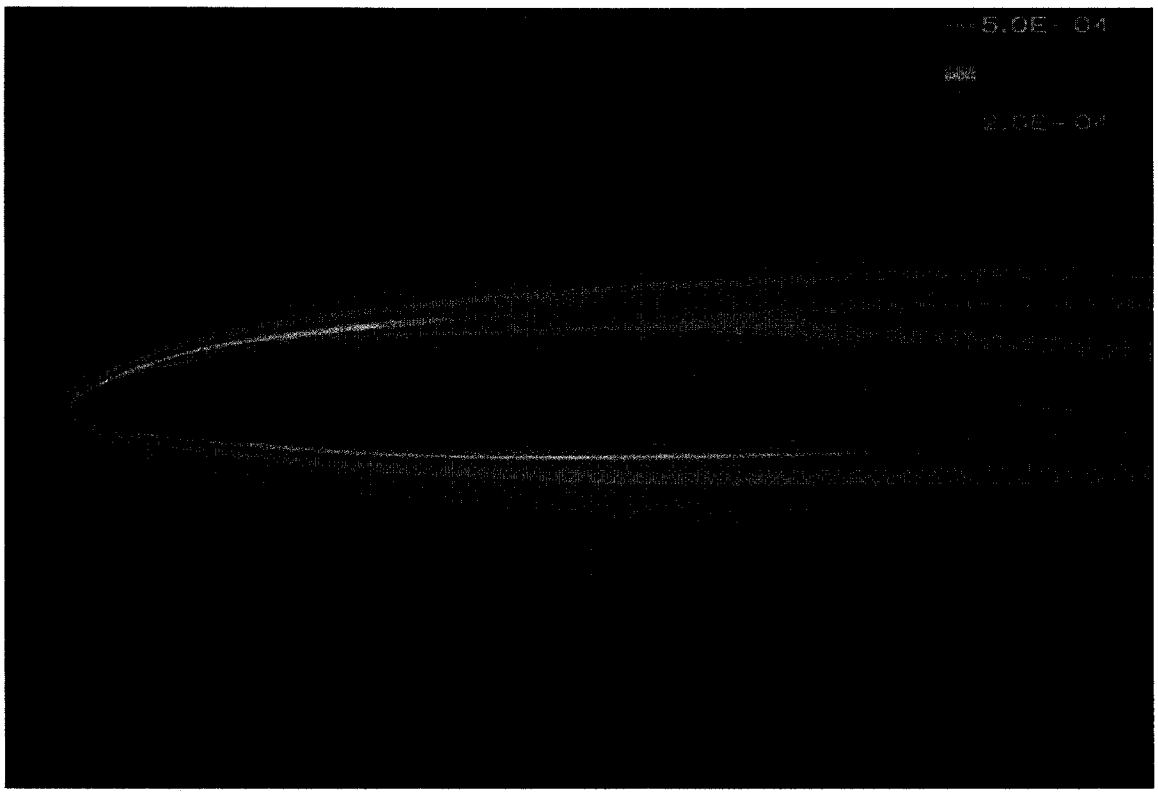

**Figure 5-22: LWC Distribution for NACA 23012 Airfoil at MVD=52 μm, DROP3D 2004**

**Figure 5-23: LWC Distribution for NACA 23012 Airfoil at MVD=52 μm, DROP3D 2005**

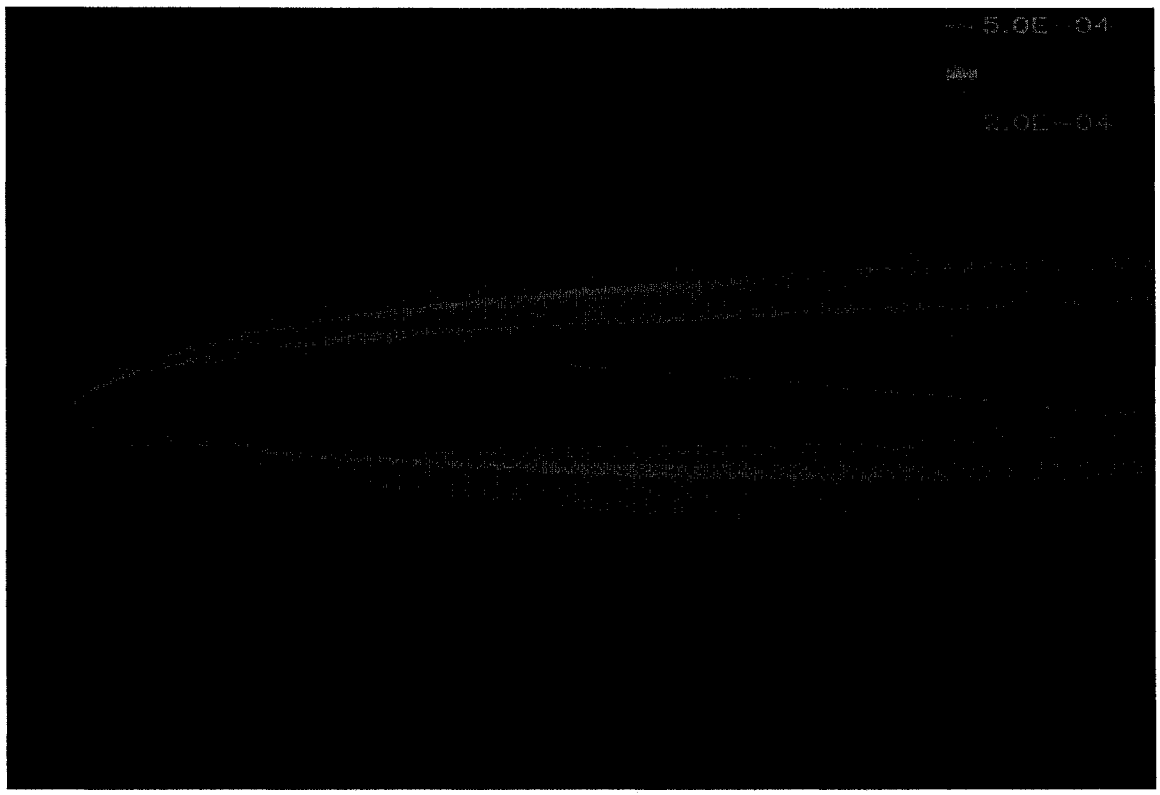


**Figure 5-24: LWC Distribution for NACA 23012 Airfoil at MVD=111 μm, DROP3D 2004**

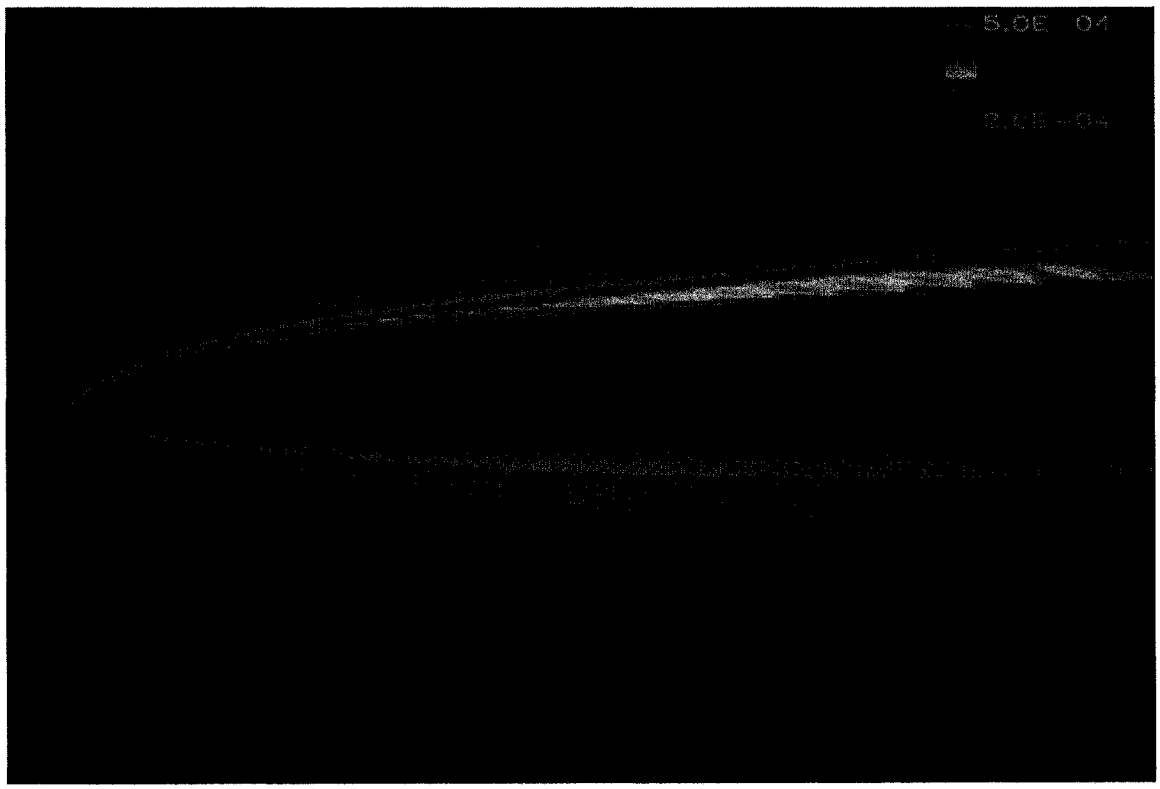


**Figure 5-25: LWC Distribution for NACA 23012 Airfoil at MVD=111 μm, DROP3D 2005**

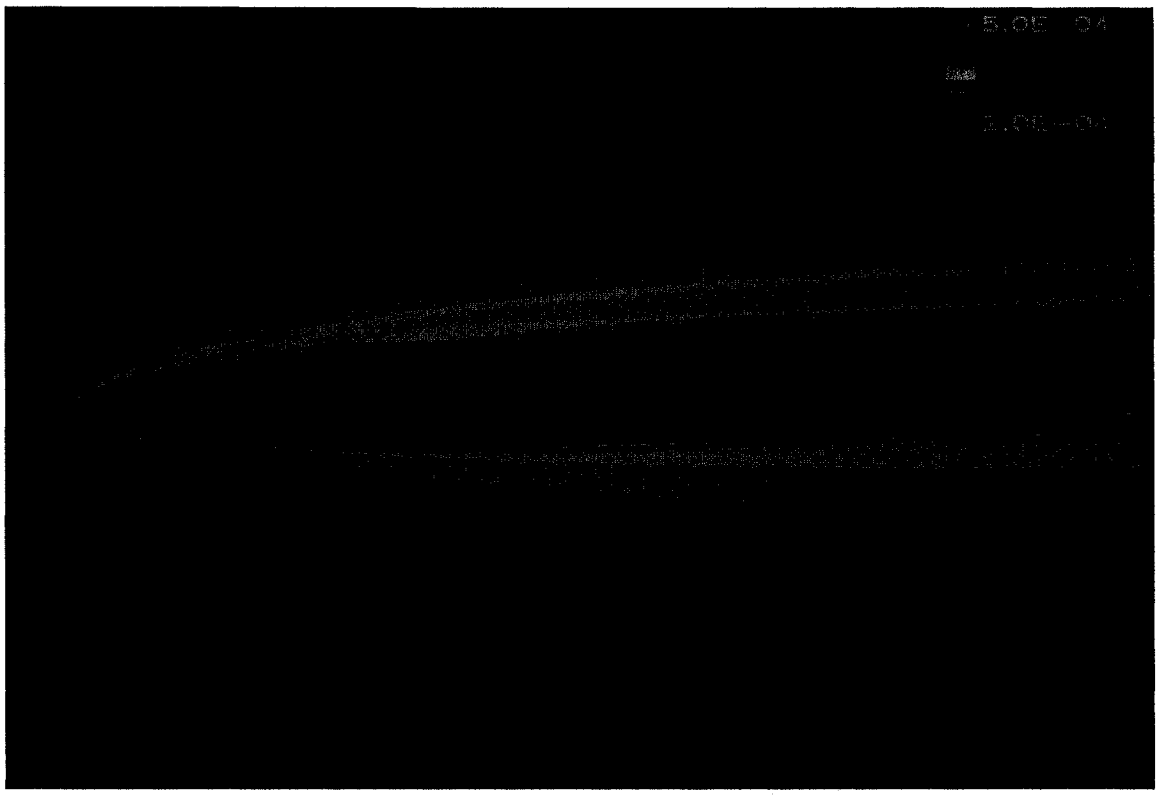

**Figure 5-26: LWC Distribution for NACA 23012 Airfoil at MVD=154 μm, DROP3D 2004**

**Figure 5-27: LWC Distribution for NACA 23012 Airfoil at MVD=154 μm, DROP3D 2005**

**Figure 5-28: LWC Distribution for NACA 23012 Airfoil at MVD=236 μm, DROP3D 2004**

**Figure 5-29: LWC Distribution for NACA 23012 Airfoil at MVD=236 μm, DROP3D 2005**

A comparison of the liquid water content distributions surrounding the NACA 23012 airfoil contour obtained from the proposed mathematical model (DROP3D 2005) to the distributions obtained from the original mathematical model (DROP3D 2004), clearly illustrates the concept of liquid mass being reintroduced into the computational domain following impingement on the airfoil surface. As expected from physical considerations regarding droplet behavior, both the overall mass of liquid deposited on the airfoil contour and the proportion of liquid mass reintroduced into the mainstream flow are shown to increase with incident droplet diameter.

The effects of droplet splashing and bouncing on aircraft surfaces located downstream of primary impingement locations is most evident from a comparison of Figures 5-24 and 5-25, as the liquid mass reintroduced into the computational domain leads to an increase in local liquid water content on the order of 15% in the airfoil's wake. As may be appreciated, an unexpected increase in incident liquid mass by 15% may easily exceed the design conditions of an in-flight anti-icing system intended to protect critical aircraft control surfaces, potentially causing subsequent system failure.

Figures 5-15 through 5-29 clearly demonstrate the proposed mathematical model's capability to appropriately model the evolution of a dispersed liquid phase under consideration of droplet-wall interactions occurring in the vicinity of solid systems boundaries. More specifically, the model provides an empirically calibrated mathematical formulation of droplet splashing and bouncing processes in an Eulerian frame of reference, producing collection efficiency distributions and impingement velocities representative of detailed experimental observations in addition to a meaningful description of droplet behavior following impact. Hence, the physical requirements regarding subsequent ice accretion simulations as identified in Section 2.3 have been satisfied.

At this point, the proposed mathematical model may be validated against an unrelated set of experimental data in order to establish the model's applicability to arbitrary geometries, flow conditions and droplet size distributions.

# 6 MODEL VALIDATION

## 6.1 Validation Test Case

As reliable experimental data pertaining to SLD specific droplet-wall interactions is rarely available at this point in time, the proposed mathematical formulation is validated against a set of data originating from a previous study performed by Papadakis et al [45] at NASA Glenn's Icing Research Tunnel. Recorded in 1997, this set of experimental data is limited to a small range of artificially generated droplet size distributions featuring MVDs of 21 $\mu$m and 92 $\mu$m.

The experimental test geometry consists of an MS317 airfoil of 0.9144 m chord and 1.8288 m span, which is mounted vertically in a wind tunnel of 1.8288 m height and 2.7432 m width. Analogous to the strategy employed in the numerical simulation of the calibration test case, merely the airfoil geometry is surrounded by a hexahedral C-grid as illustrated in Figure 6-1 rather than meshing the experimental geometry in its entirety. The resulting computational grid is comprised of 53504 hexahedral elements and 108208 nodes, providing a sufficiently fine spatial resolution in the vicinity of the airfoil contour to facilitate an accurate capture of the aerodynamic boundary layer.

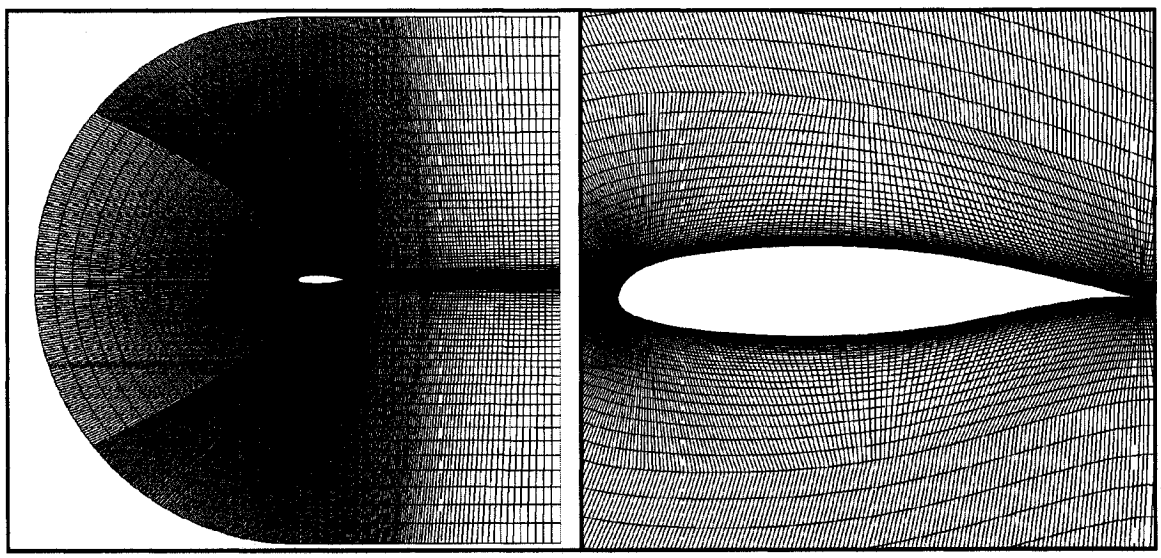

**Figure 6-1: Hexahedral C-Grid Surrounding MS317 Airfoil**

# 6.2 Experimental Conditions

Papadakis et al [45] identify the following set of aerodynamic boundary conditions to characterize the mainstream flow around the MS317 airfoil contour:

- Free stream velocity: $U_\infty$ = 78.68 m/s
- Free stream temperature: $T_\infty$ = 281.00 K
- Free stream pressure: $p_\infty$ = 94.67 kPa
- Geometric angle of attack: $AoA$ = 0.00, 8.00 °
- Gravitational acceleration: $\vec{g}$ = {0,0,-9.81} $m/s^2$

Due to the airfoil's vertical orientation within the wind tunnel, the gravitational acceleration vector is oriented along the airfoil's spanwise direction. The droplet diameters and associated volumetric fractions corresponding to 7 bin approximations of the experimental droplet size distributions are listed in Table 6-1. While the available experimental data is limited to only one droplet distribution subject to significant droplet-wall interactions, the consideration of two geometric angles of attack provides an opportunity to test the mathematical model in diverse flow conditions. Furthermore, the numerical results obtained from the proposed mathematical model may be directly compared to those based on the NASA LEWICE [10] impingement simulation code.

**Table 6-1: 7 Bin Approximations of Experimental Droplet Size Distributions [45]**

| I | $P_I$ (%) | DROPLET DIAMETER ($\mu$m) | |
|---|---|---|---|
| | | MVD 20 | MVD 92 |
| 1 | 5.0 | 6.51 | 28.52 |
| 2 | 10.0 | 10.92 | 47.84 |
| 3 | 20.0 | 14.91 | 65.32 |
| 4 | 30.0 | 21.00 | 92.00 |
| 5 | 20.0 | 28.77 | 126.04 |
| 6 | 10.0 | 36.54 | 160.08 |
| 7 | 5.0 | 46.62 | 204.24 |

# 6.3 Aerodynamics

The computational domain depicted in Figure 6-1 neglects the physical presence of the icing research tunnel and hence the associated aerodynamic influence on the flow field surrounding the MS317 airfoil. Analogous to the strategy employed in the numerical simulation of the NACA 23012 airfoil, the aerodynamic effects of the wind tunnel are addressed by means of effective angles of attack. Figures 6-2 and 6-5 demonstrate good agreement between the experimentally observed pressure coefficient distributions and their numerical equivalent obtained from FENSAP$^{TM}$ simulations at effective angles of attack equal to -1.00° and 8.00°, respectively.

Please refer to Figures 6-3 and 6-4 for illustrations of the pressure and Mach number contours around the MS317 airfoil at a geometric angle of attack of 0.00° as well as Figures 6-6 and 6-7 for illustrations of the pressure and Mach number contours corresponding to a geometric angle of attack of 8.00°.

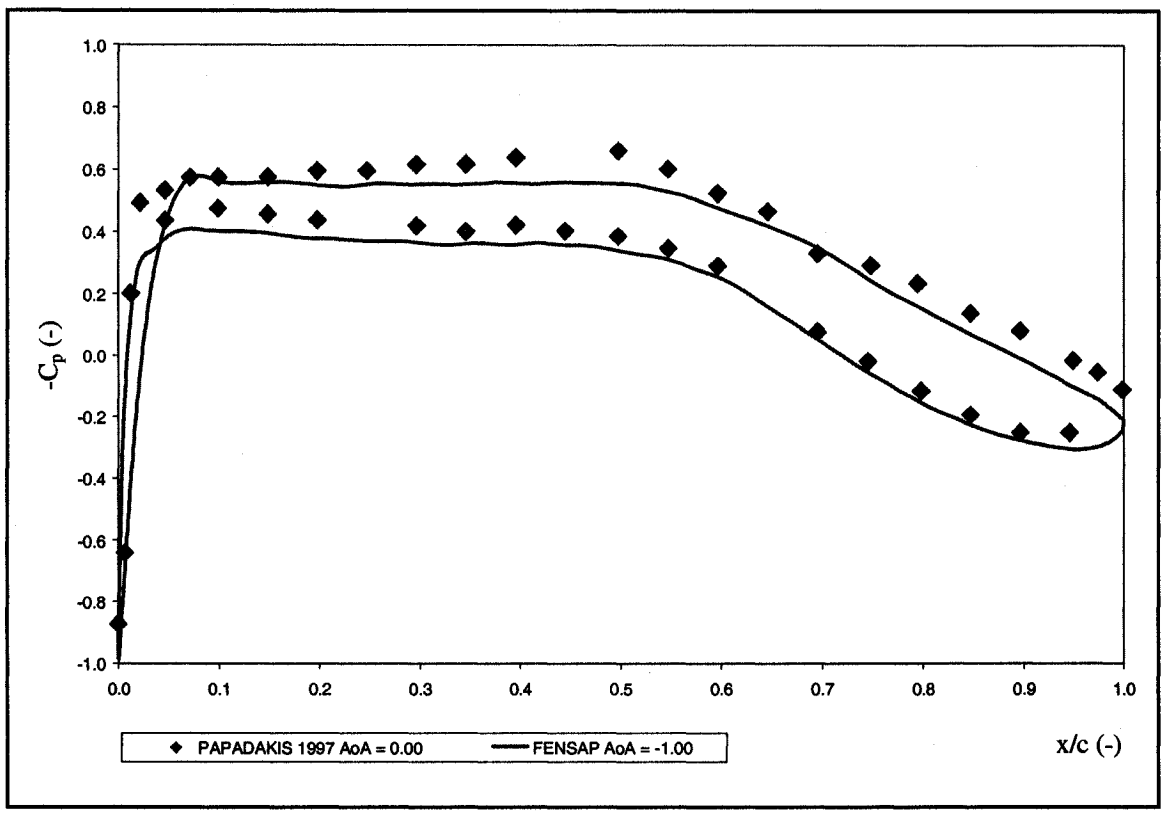


**Figure 6-2: Pressure Coefficient Distribution for MS317 Airfoil at AoA=0.00°**

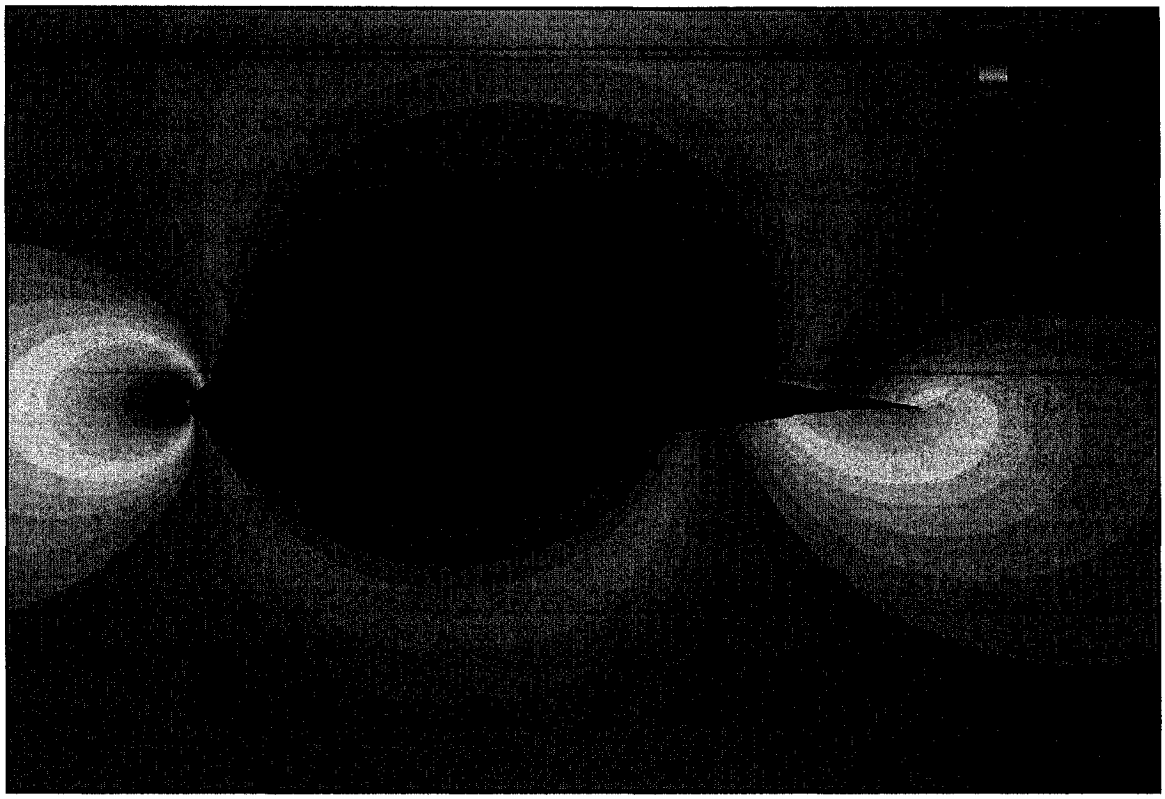

**Figure 6-3: Pressure Contours for MS317 Airfoil at AoA=0.00°**

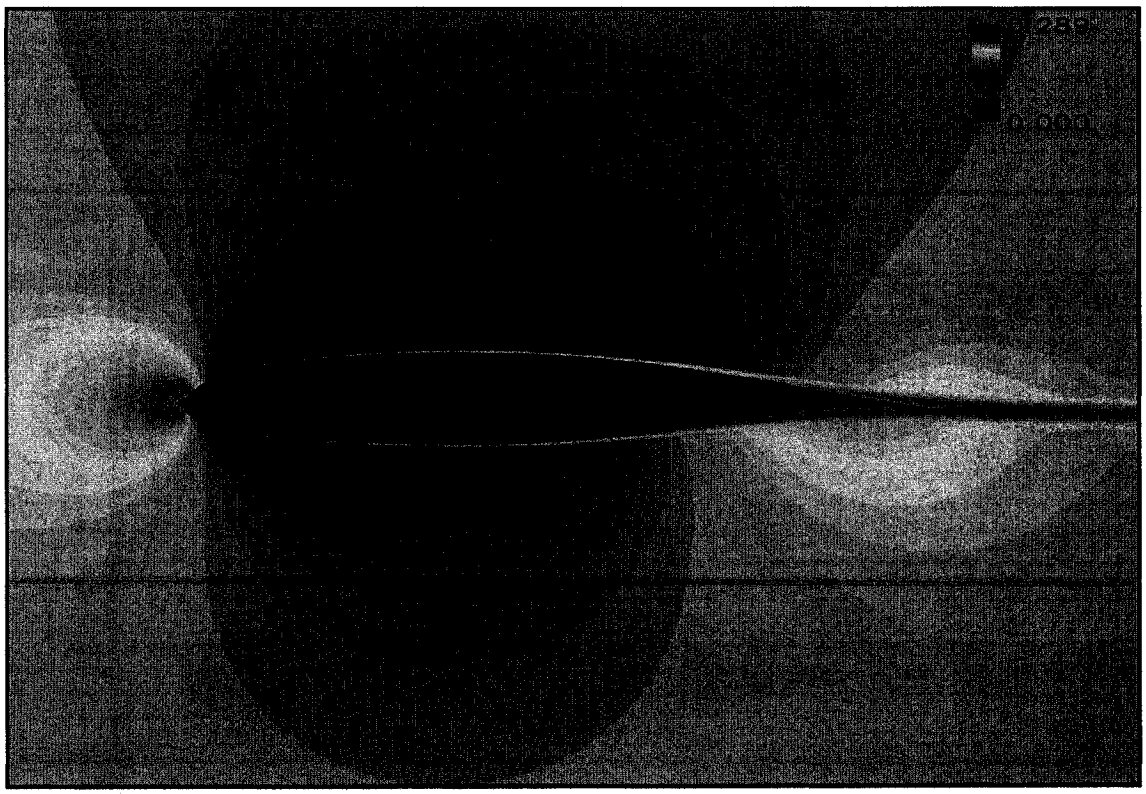

**Figure 6-4: Mach Number Contours for MS317 Airfoil at AoA=0.00°**

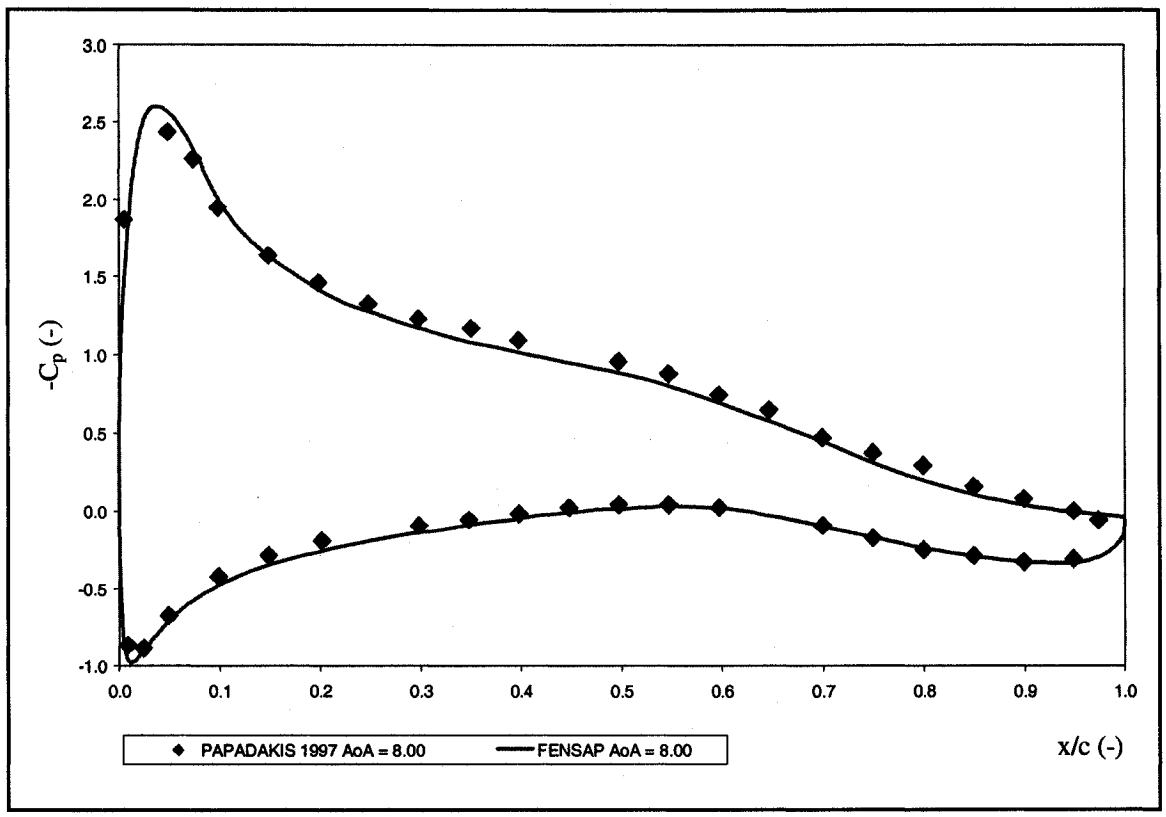


**Figure 6-5: Pressure Coefficient Distribution for MS317 Airfoil at AoA=8.00°**

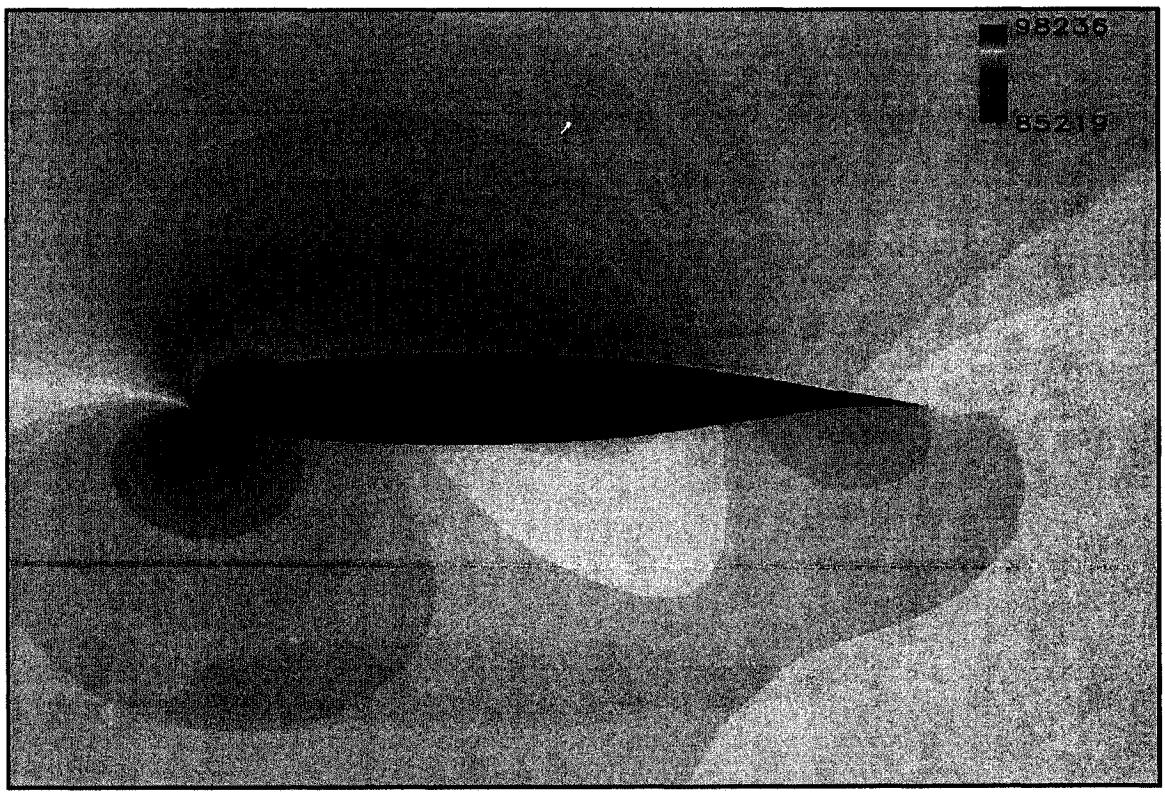


**Figure 6-6: Pressure Contours for MS317 Airfoil at AoA=8.00°**

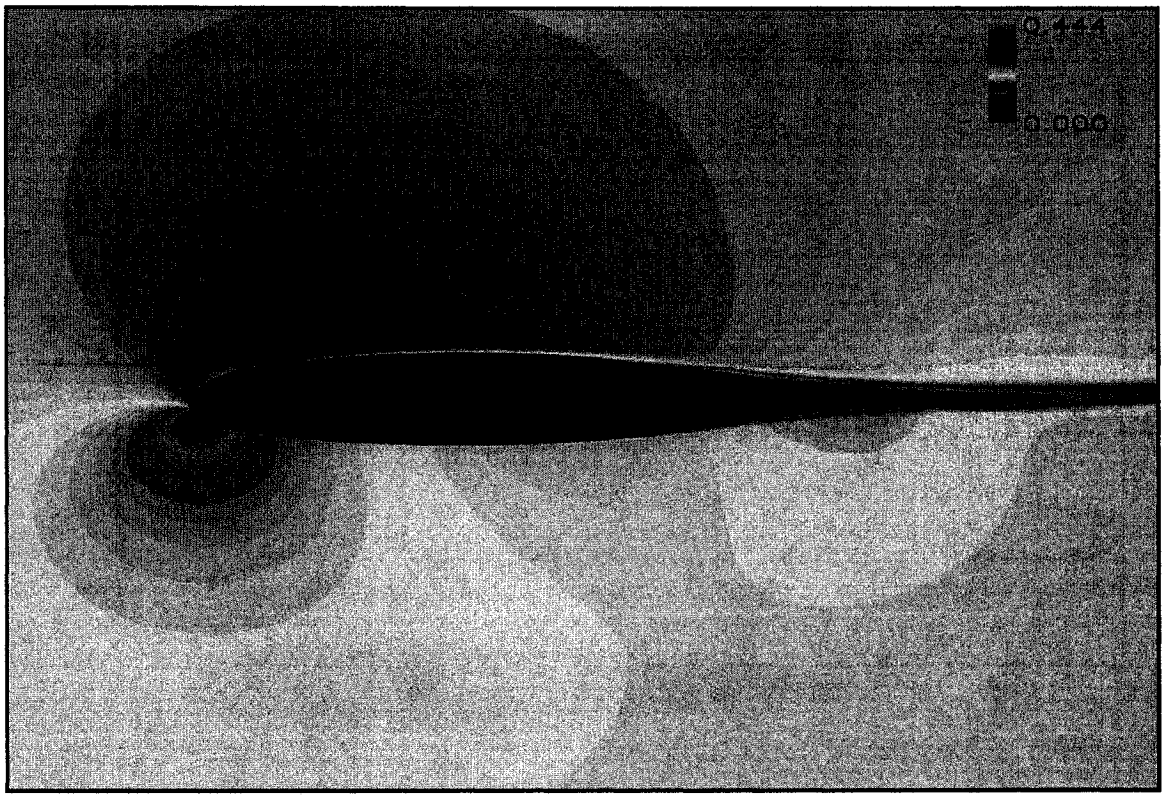

**Figure 6-7: Mach Number Contours for MS317 Airfoil at AoA=8.00°**

# 6.4 Droplet Impingement

Analogous to the calibration test case, the distributions of collection efficiencies obtained from the proposed mathematical model (DROP3D 2005) are compared to numerical results based on the original mathematical model (DROP3D 2004) as well as experimental data (PAPADAKIS 1997). An additional comparison may be made to numerical results published in 2004 by Wright and Potapczuk [42], obtained from droplet impingement simulations based on NASA's LEWICE [10] code. Traditionally, LEWICE is based on a purely Lagrangian formulation of the droplet impingement process and facilitates an estimate of droplet impingement characteristics in the absence of droplet-wall interactions (LEWICE 2.0). However, a recent adoption of the impingement model proposed by Trujillo and Lee [39] considers the effects of droplet splashing, while the concept of droplet bouncing is not addressed by the extended mathematical model (LEWICE 3.0). Figures 6-8 through 6-11 and Figures 6-12 through 6-15 present a comparison of collection efficiencies at respective angles of attack of 0.00° and 8.00°.

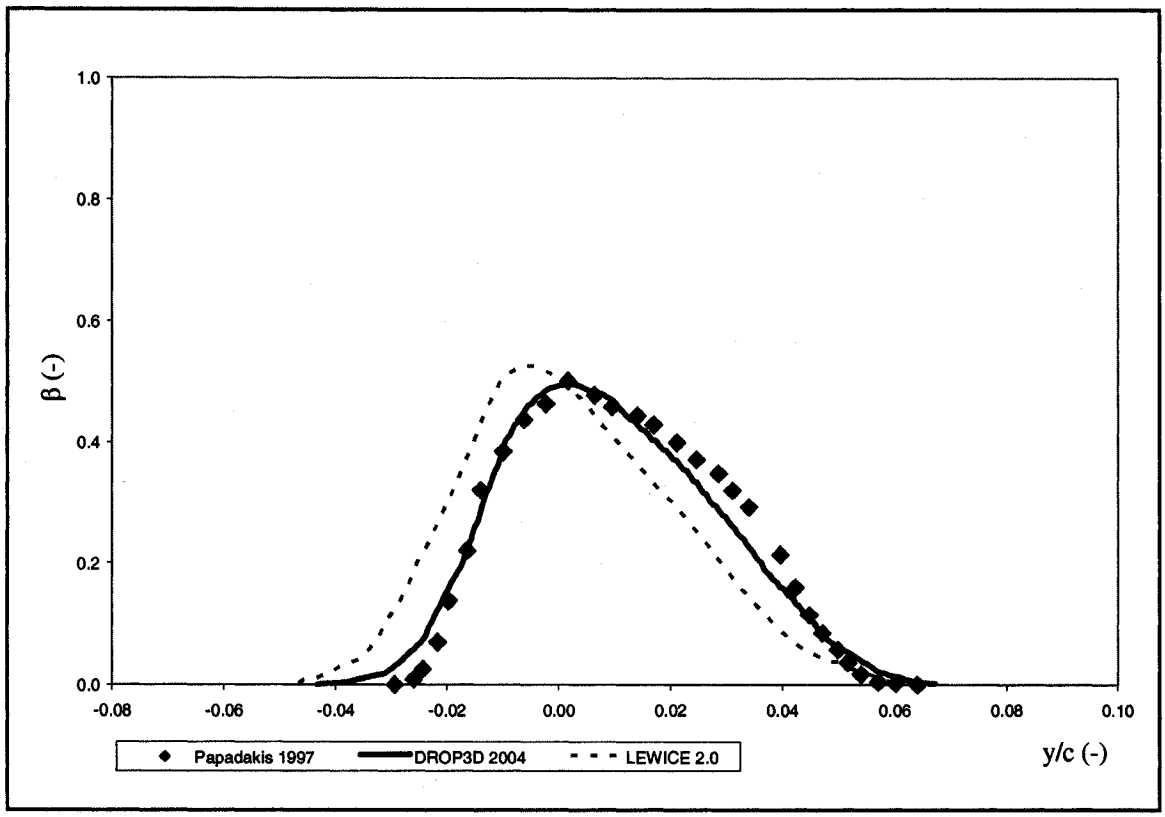


**Figure 6-8: Collection Efficiency for MS317 Airfoil at AoA = 0.00° and MVD = 21 μm, $F_S = 0$**

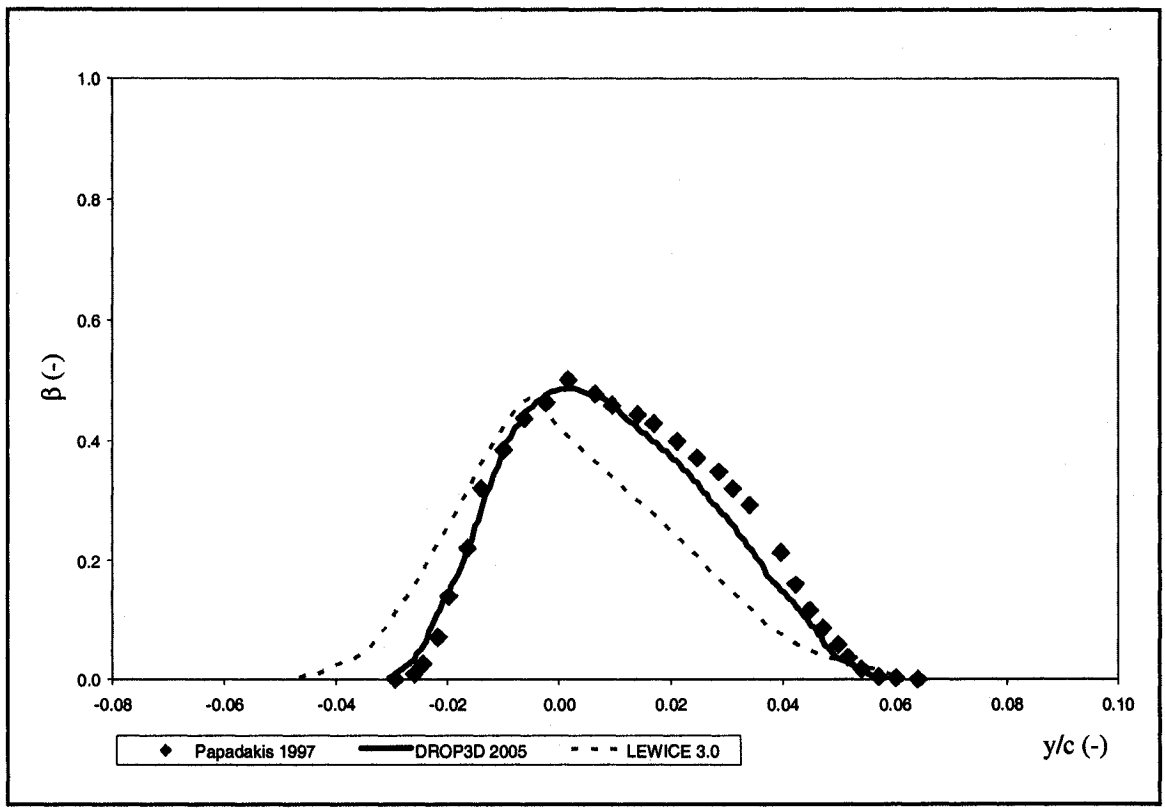


**Figure 6-9: Collection Efficiency for MS317 Airfoil at AoA = 0.00° and MVD = 21 μm, $F_S \neq 0$**

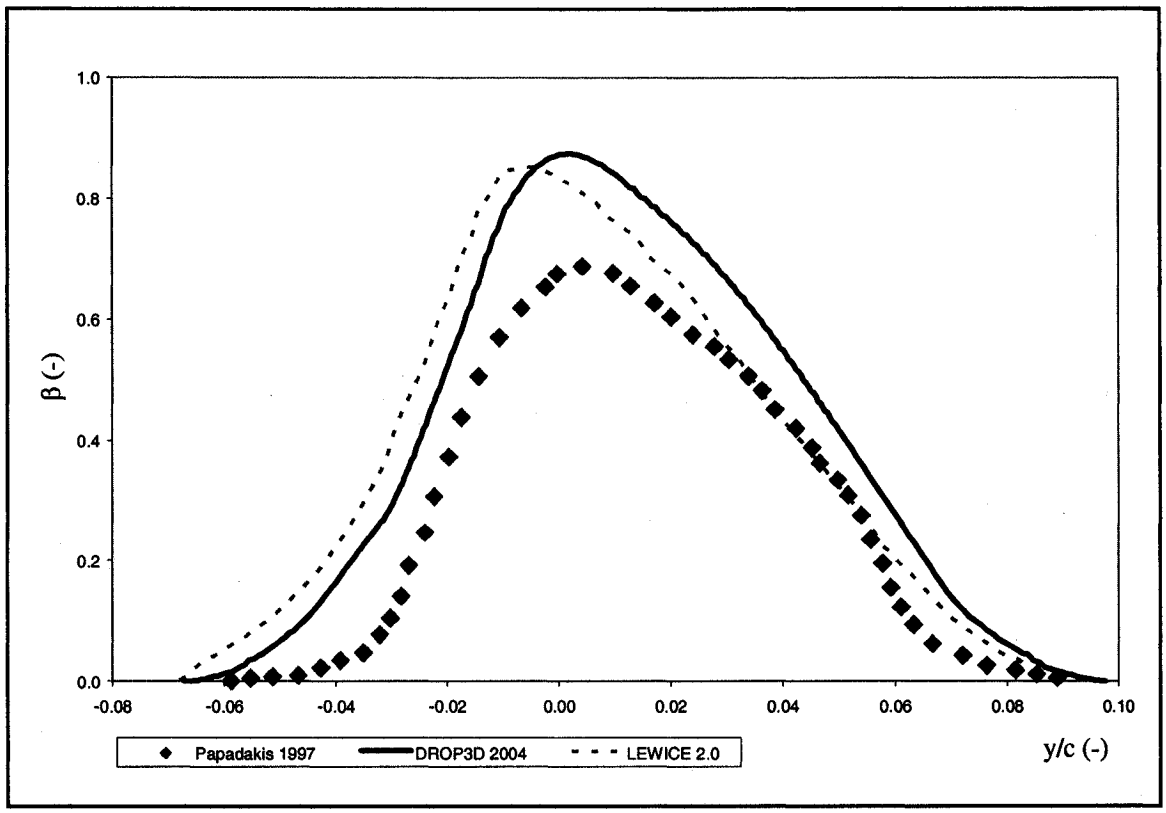


**Figure 6-10: Collection Efficiency for MS317 Airfoil at AoA = 0.00° and MVD = 92 μm, $F_S = 0$**

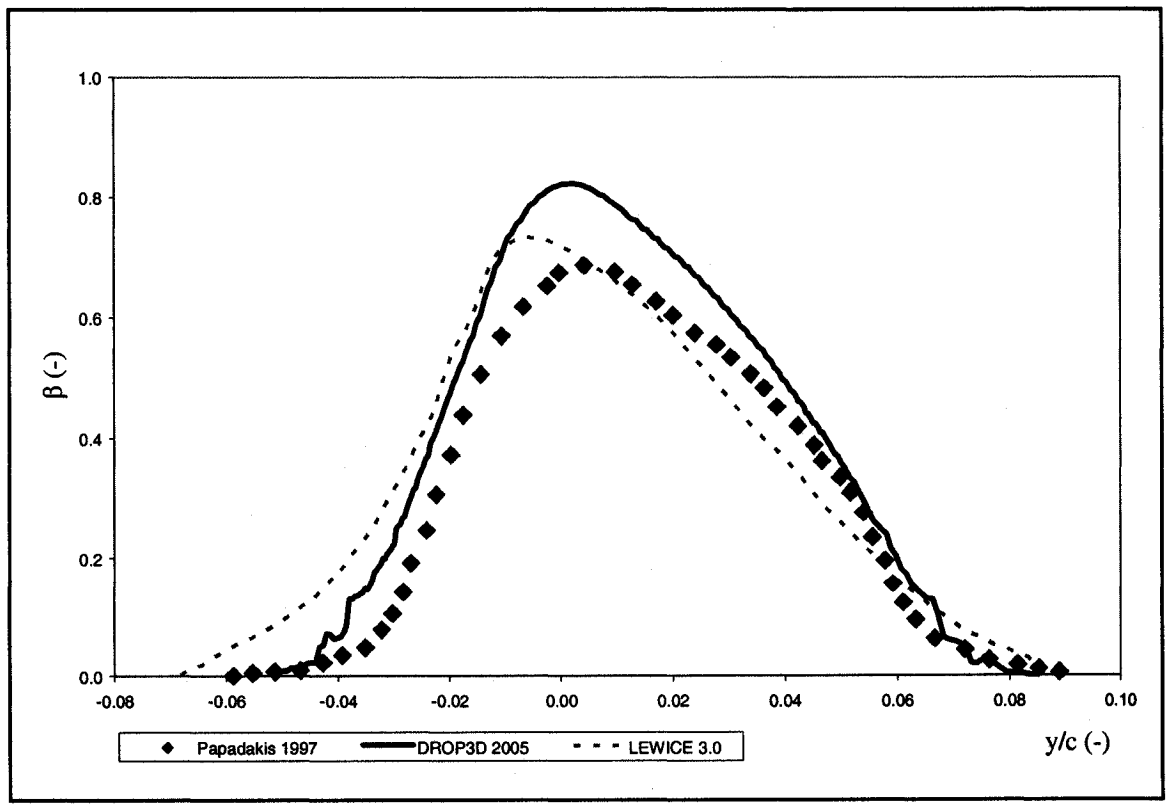


**Figure 6-11: Collection Efficiency for MS317 Airfoil at AoA = 0.00° and MVD = 92 μm, $F_S \neq 0$**

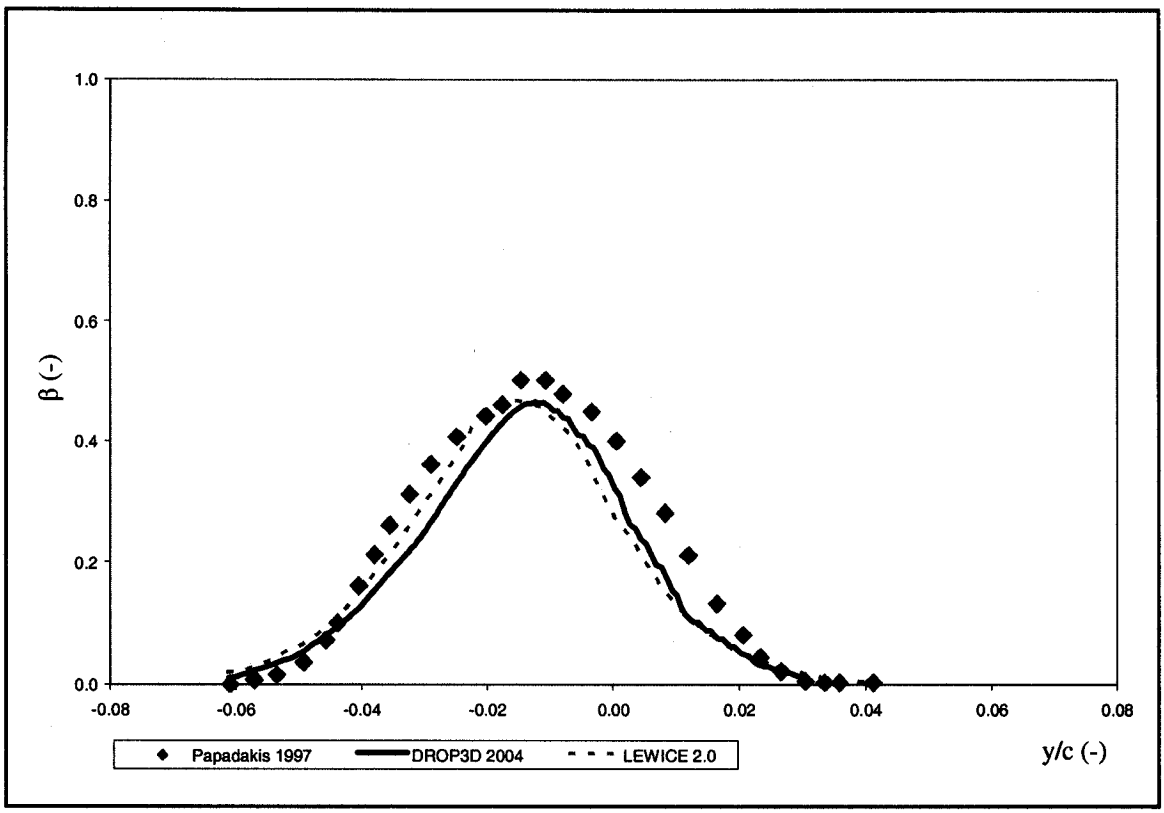


**Figure 6-12: Collection Efficiency for MS317 Airfoil at AoA=8.00° and MVD=21 μm, $F_S = 0$**

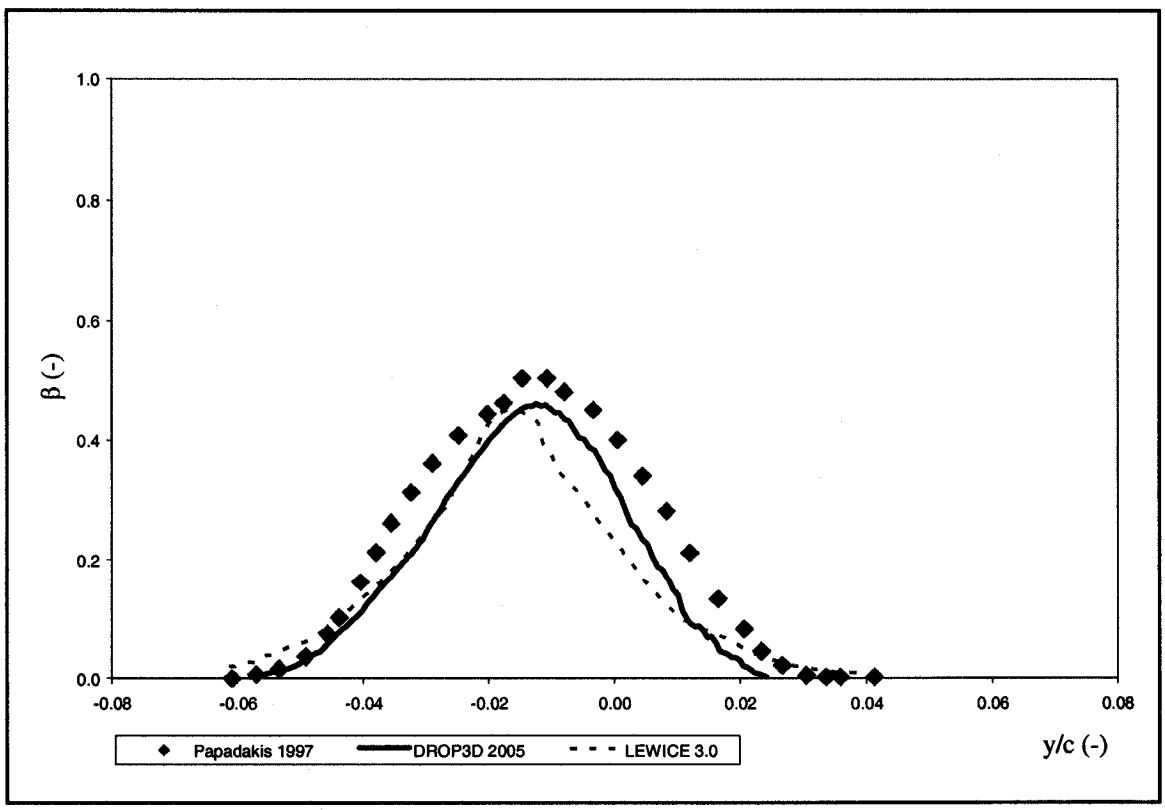


**Figure 6-13: Collection Efficiency for MS317 Airfoil at AoA=8.00° and MVD=21 μm, $F_S \neq 0$**

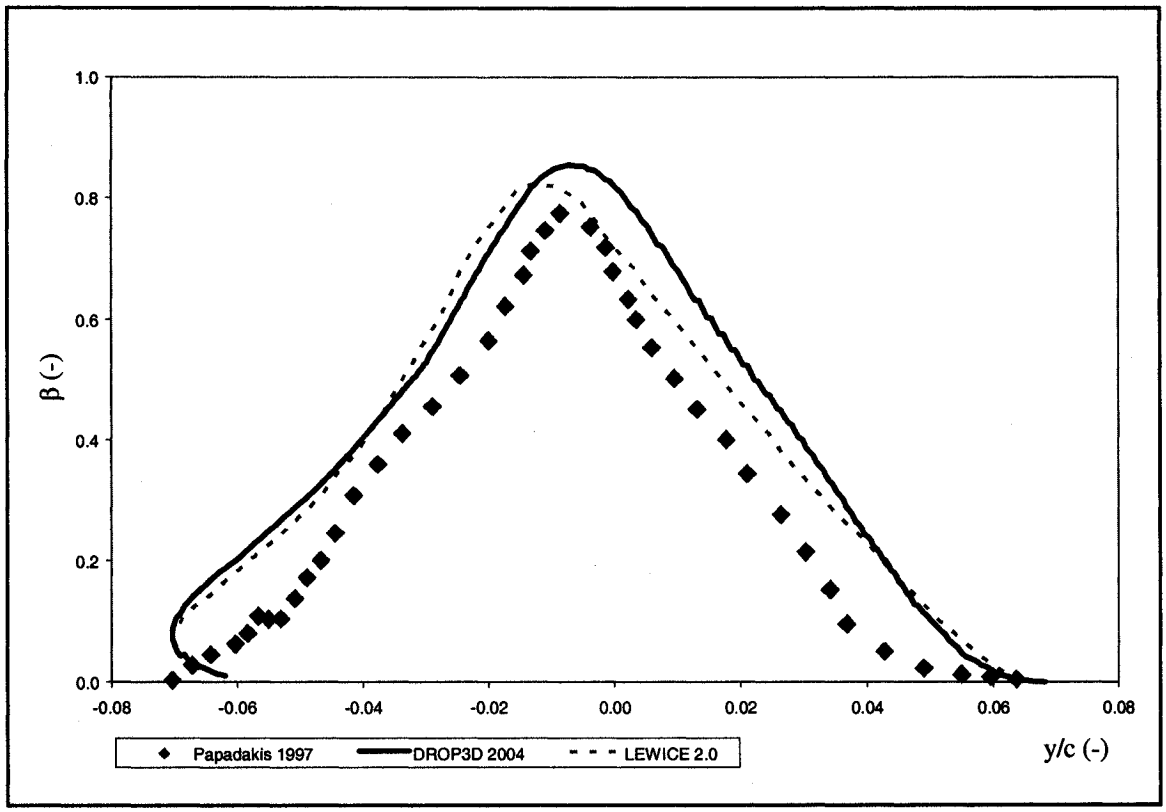


**Figure 6-14: Collection Efficiency for MS317 Airfoil at AoA=8.00° and MVD=92 μm, $F_S = 0$**

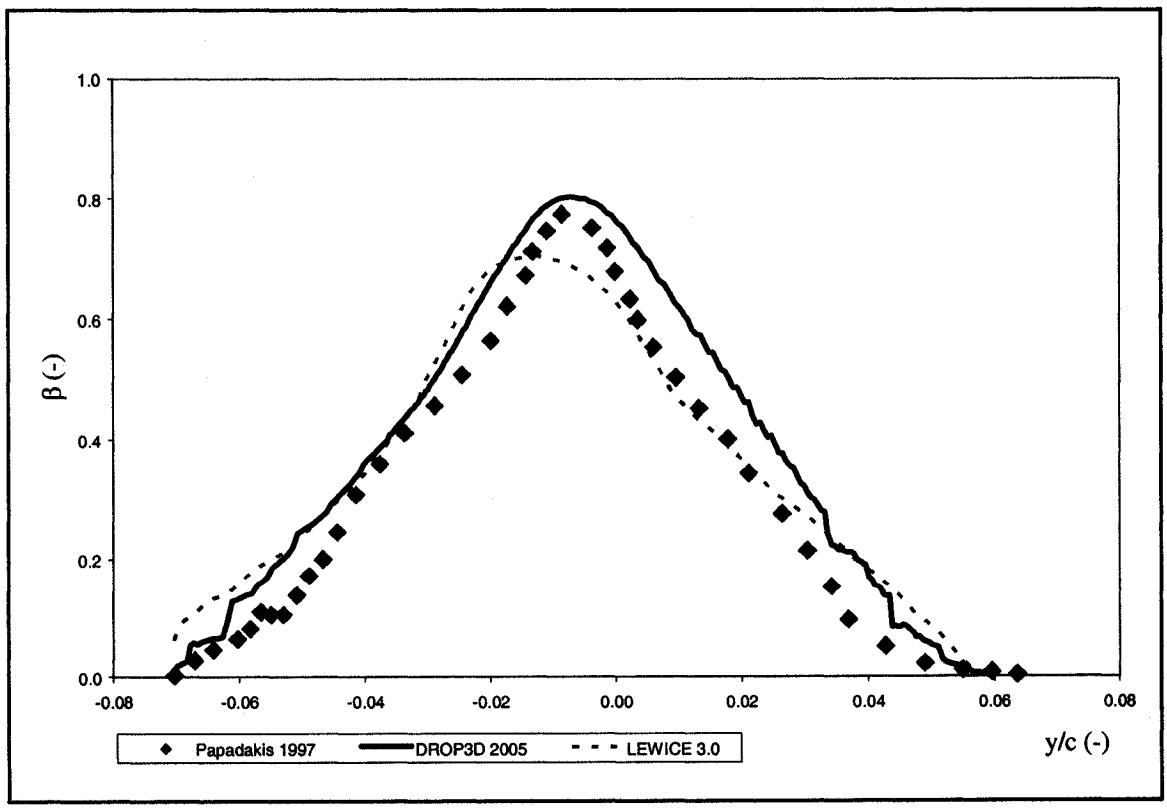


**Figure 6-15: Collection Efficiency for MS317 Airfoil at AoA=8.00° and MVD=92 μm, $F_S \neq 0$**

An inspection of the collection efficiency distributions corresponding to a geometric angle of attack of 0.00° as presented in Figures 6-8 through 6-11 reveals significant discrepancies between the numerical results predicted by LEWICE and DROP3D™, irrespective of the consideration of droplet-wall interactions. More precisely, the collection efficiency distributions obtained from LEWICE feature a consistent shift toward the airfoil's pressure side with respect to the numerical results obtained from DROP3D™ as well as the experimental reference data. As this shift is not observed at a geometric angle of attack of 8.00°, the author suspects the LEWICE simulations of droplet impingement at a geometric angle of attack of 0.00° to be based on an incorrectly simulated aerodynamic flow field. Therefore, the following discussion of numerical results will not address this particular discrepancy in further detail.

A comparison of Figures 6-8 and 6-9 as well as Figures 6-12 and 6-13 discloses the tendency of LEWICE to predict significant mass loss due to splashing in the vicinity of the airfoil leading edge, a surprising result for droplet distributions featuring a mean volumetric diameter of 21 $\mu$m, irrespective of the aerodynamic angle of attack. In contrast, DROP3D™ predicts negligible mass loss near the airfoil leading edge as expected, attributing only a slight amount of mass loss to droplets bouncing off the airfoil near the impingement limits. As a consequence, the proposed mathematical model predicts collection efficiency distributions in close agreement with experimental observations at a mean volumetric diameter of 21 $\mu$m, while numerical results obtained from LEWICE exhibit unjustified deviations from experimental reference data.

The pronounced differences regarding the location and extent of mass loss as predicted by LEWICE and DROP3D™ become more apparent in the simulation of droplet distributions featuring a larger MVD of 92 $\mu$m, as may be appreciated from an inspection of Figures 6-10 and 6-11 as well as Figures 6-14 and 6-15. While the significant mass loss near the airfoil leading edge as predicted by LEWICE is physically justifiable and generally serves to improve the quality of the numerical results, the deviation from experimental reference data becomes increasingly pronounced as the impingement limits are approached. Wright and Potapczuk [42] wrongfully attribute this deviation to a failure of the splashing model proposed by Trujillo and Lee [39] associated with the

pronounced decrease in the impingement velocity's magnitude observed in the limit of flow tangency. However, as convincingly demonstrated in Figure 5-5, the droplet splashing model ceases to be applicable at such locations and the deviation reported by Wright and Potapczuk [42] is caused by the complete negligence of a droplet bouncing model in the mathematical formulation of LEWICE.

The collection efficiency distributions predicted by DROP3D$^{TM}$ support this conclusion as a substantial amount of mass loss due to droplet bouncing is observed in the vicinity of the impingement limits, resulting in acceptably close agreement with experimental reference data at both aerodynamic angles of attack. While the mass loss incurred near the airfoil leading edge is reasonably well simulated at an angle of attack of 8.00°, it is rather ill predicted at 0.00°. A similar observation may be made regarding the quality of the numerical results obtained from LEWICE as the leading edge mass loss is insufficient at 0.00° while it is excessive at 8.00°. A more detailed inspection of Figures 6-10 and 6-11 as well as Figures 6-14 and 6-15 reveals that both LEWICE and DROP3D$^{TM}$ predict mass losses due to splashing which are of comparable extent at both aerodynamic angles of attack. However, the discrepancy between numerical results obtained without consideration of droplet-wall interactions and experimental data is significantly more pronounced at 0.00° than at 8.00°. Hence, the introduction of a similarly extensive mass loss improves the quality of the numerical results at both angles of attack and since the initial deviation from experimental data is less at 8.00°, the augmented numerical results feature better agreement with experimental data as well. While the deviation from experimental data is generally more pronounced than in the calibration test case, the collection efficiency distributions provided by DROP3D$^{TM}$ consistently tend toward the experimental reference data and hence the proposed mathematical model may be considered applicable to the MS317 test geometry and associated flow conditions.

Figures 6-16 through 6-19 illustrate the liquid water content distributions surrounding the MS317 airfoil contour at an MVD of 92 $\mu$m. As in the calibration test case, a significant increase in liquid mass is observed in the airfoil's wake, further demonstrating the model's capability to simulate the effect of droplet-wall interactions on surfaces located downstream of initial impingement locations.

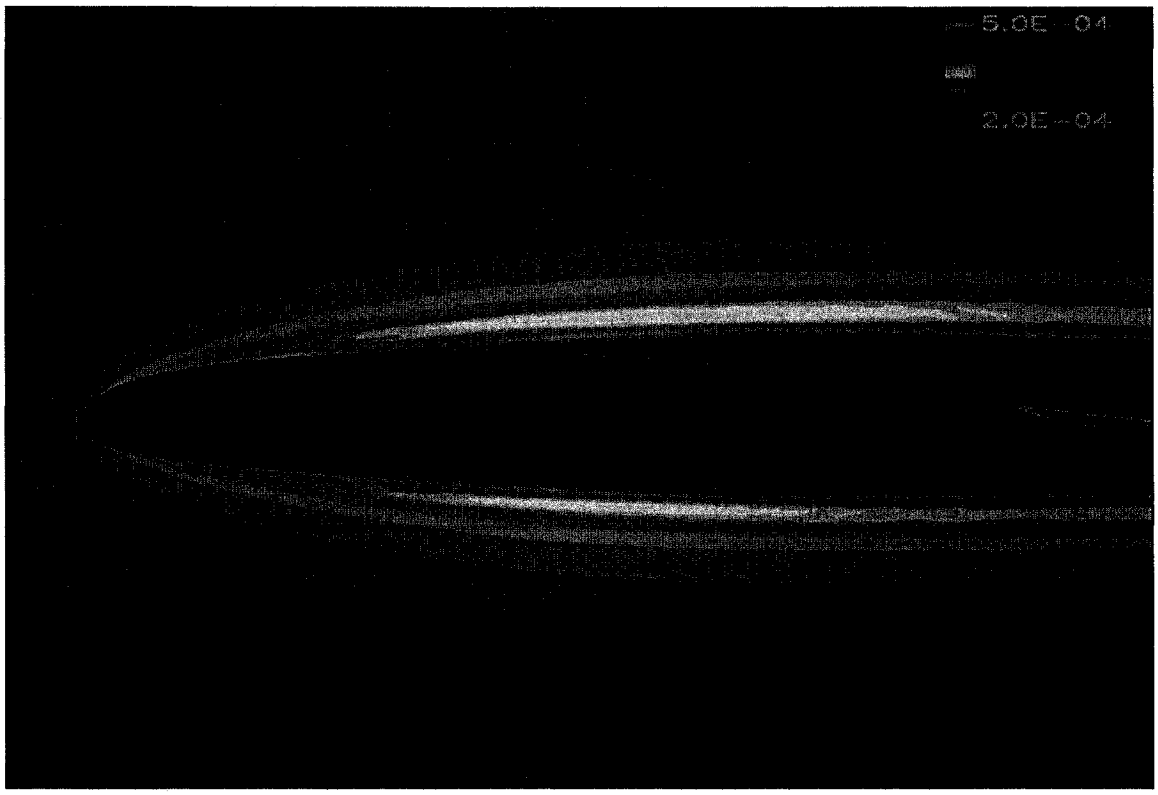


**Figure 6-16: LWC Distribution for MS317 Airfoil at AoA=0.00° and MVD=92 μm, DROP3D 2004**

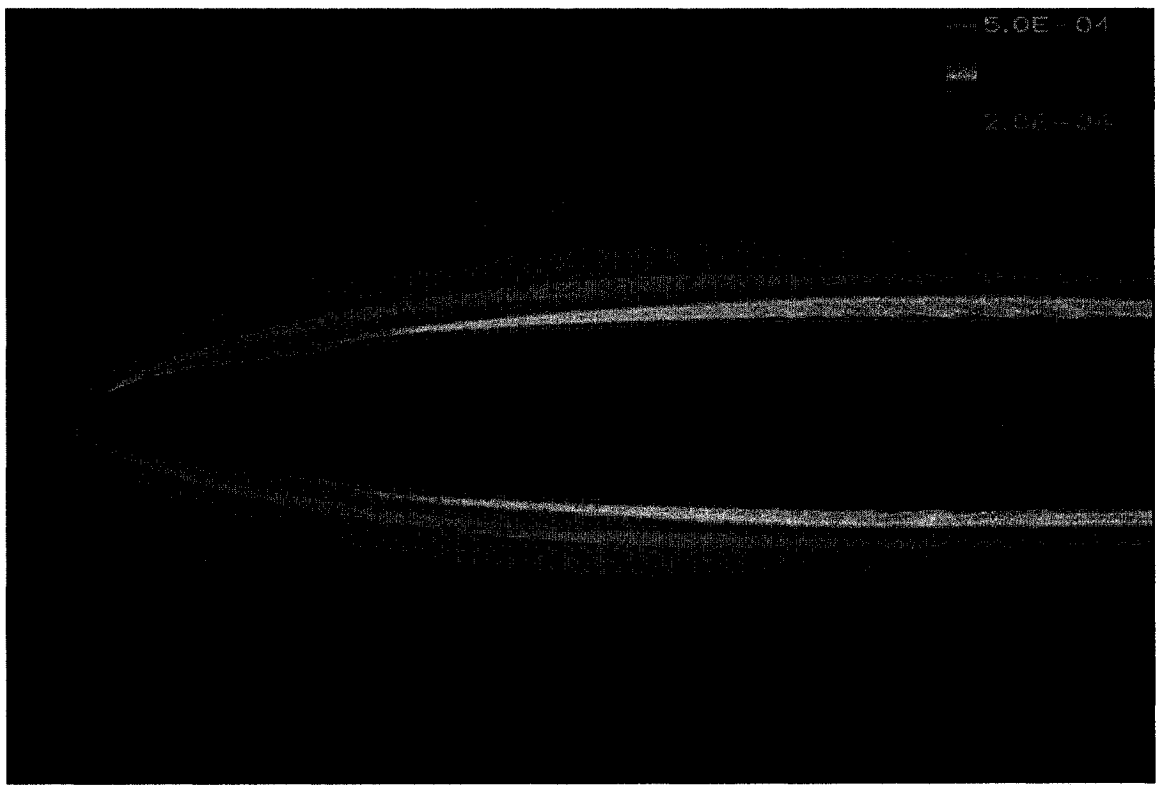


**Figure 6-17: LWC Distribution for MS317 Airfoil at AoA=0.00° and MVD=92 μm, DROP3D 2005**

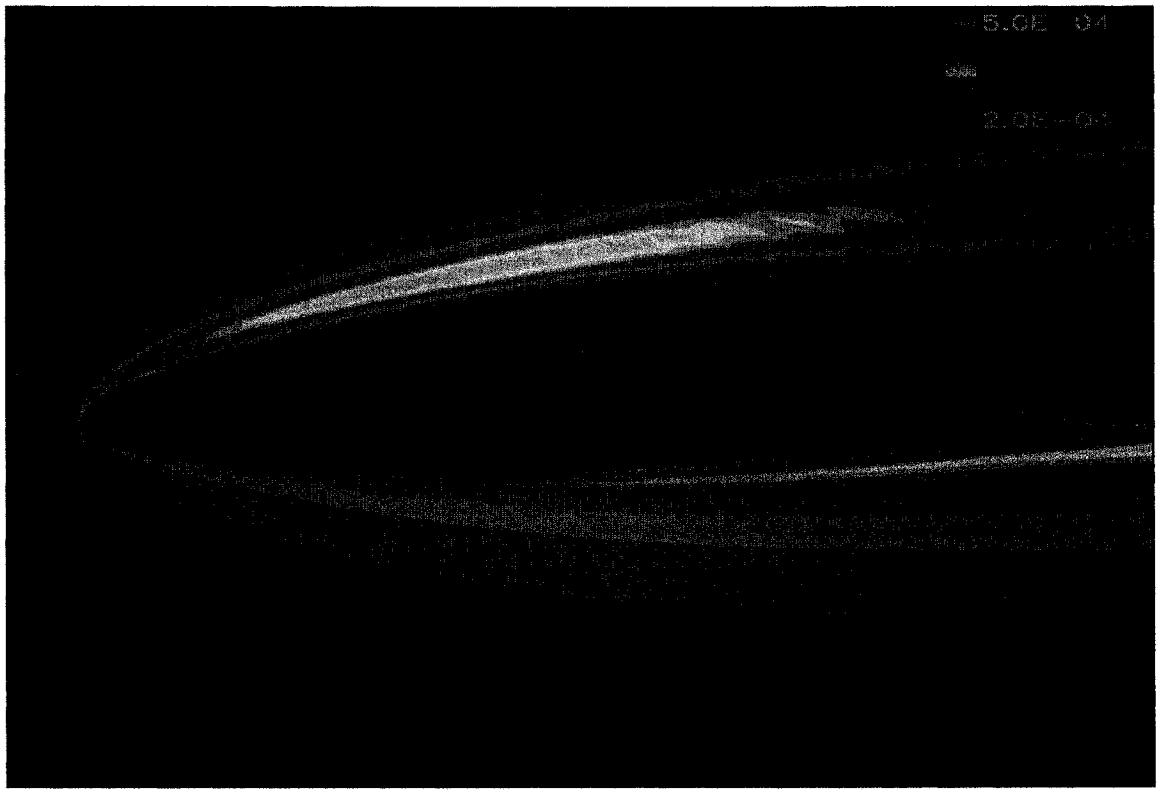

**Figure 6-18: LWC Distribution for MS317 Airfoil at AoA=8.00° and MVD=92 μm, DROP3D 2004**

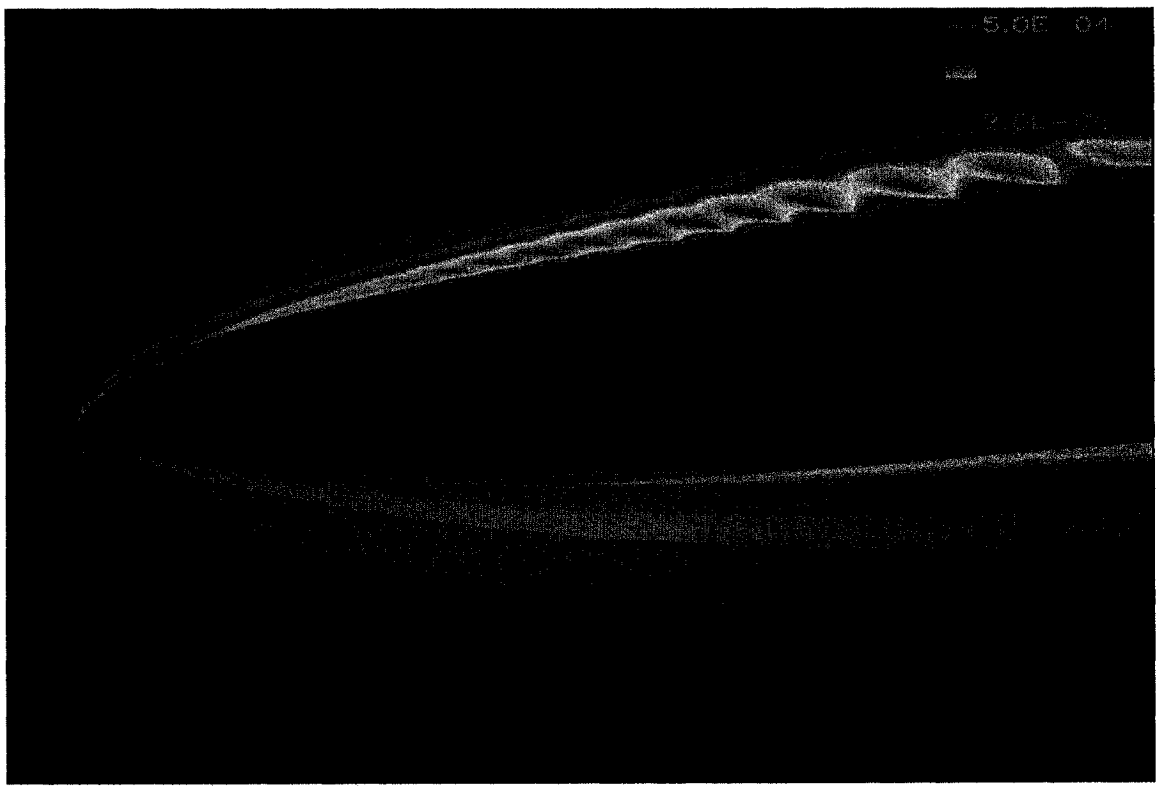

**Figure 6-19: LWC Distribution for MS317 Airfoil at AoA=8.00° and MVD=92 μm, DROP3D 2005**

# 7 CONCLUSIONS AND RECOMMENDATIONS

A suitable mathematical model for the description of droplet-wall interactions in an Eulerian frame of reference has been proposed and successfully calibrated against experimental reference data. The excellent agreement between numerical and experimental data observed in the simulation of the calibration test case serves to demonstrate the proposed mathematical model's general simulation capabilities. In addition to predicting collection efficiency distributions and velocity profiles in close agreement with experimental observations, the evolution of secondary droplet mass following initial impingement is modeled in a physically representative manner.

The deviations from experimental data observed in the simulation of the validation test case may be attributable either to an insufficiently broad calibration of the proposed mathematical model or to a difference in experimental measurement methods. The limited validation data available originates from an experiment conducted in 1997 while the calibration data observed in 2004 represents the results of a systematic empirical approach. As the calibration data observed in 2004 is most likely based on more sophisticated measurement methods, it is deemed more reliable than the validation data. Also, a more refined approximation of experimental droplet size distributions would most likely result in better agreement with experimental data as observed in the simulation of the calibration test case based on 10 and 27 bin approximations.

A continued need for extensive comparison with experimental data may thus be identified in order to verify whether the currently proposed functionality of the expressions governing collision contact time and splashed mass fraction are indeed applicable to arbitrary geometries and flow conditions. However, reliable experimental data pertaining to droplet impingement behavior at SLD conditions is currently limited in availability due to the relatively recent confirmation of SLD droplet existence.

As introduced in Section 4.2.5, the current mathematical formulation of DROP3D$^{TM}$ is unable to communicate external disturbances into the computational domain due to a lack

of a pressure equivalent source term in the equations governing droplet momentum. In order to prevent an unphysical accumulation of liquid mass due to a discontinuous velocity field in the vicinity of a solid boundary, the continuity equation has been modified at computational nodes located on a solid boundary. While an illustration of liquid water content distributions demonstrates physical droplet behavior and hence suggests the numerical deficiency to be of negligible extent, continuity is not mathematically guaranteed within elements adjacent to solid boundaries. Hence, a future need for the formulation of a pressure equivalent source term may be identified in order to identically satisfy droplet continuity at solid boundaries.

In any case, the proposed mathematical model provides physically justifiable and numerically consistent results, presenting a significant improvement over the original formulation of DROP3D$^{TM}$ as well as the current formulation of LEWICE. The conception of a body force equivalent source term accounting for the effects of droplet wall-interactions in the equations governing droplet momentum facilitates a continued exploitation of the advantages associated with an Eulerian formulation as delineated in Section 2.2. Hence, modeling requirements imposed by future FAA certification regulations regarding the physically representative simulation of droplet impingement in the SLD regime of aircraft in-flight icing may be satisfied by the proposed improvement of the mathematical formulation of DROP3D$^{TM}$.

The proposed mathematical model may also be employed in the simulation of a variety of industrial applications involving the propagation of particulate multiphase systems subject to solid system boundaries. The model's underlying physical principles suggest a particular applicability to fuel injection, spray coating and multiphase segregation processes as a detailed consideration of droplet-wall interactions is equally important in a physically accurate numerical simulation of such processes.

# 8 BIBLIOGRAPHY


[1] Beaugendre, H., *A PDE-Based 3D Approach to In-Flight Ice Accretion*, Ph.D. Thesis, McGill University, Montreal, 2003

[2] Bragg, M.B., *Aircraft Aerodynamic Effects due to Large Droplet Ice Accretions*, AIAA-96-0932

[3] Brahimi, M.T., Tran, P., Tezok, F., Paraschivoiu, I., *Aircraft Icing due to Supercooled Large Droplets*, pp. 533-544

[4] Brahimi, M.T., Tran, P., Chocron, D., Tezok, F., Paraschivoiu, I., *Effect of Supercooled Large Droplets on Ice Accretion Characteristics*, AIAA-97-0306

[5] Tan, S.C., Papadakis, M., *General Effects of Large Droplet Dynamics on Ice Accretion Modeling*, AIAA-2003-0392

[6] Wright, W.B., Potapczuk, M.G., *Computational Simulation of Large Droplet Icing*, Proceedings of the FAA International Conference on Aircraft In-Flight Icing, pp. 545-555, 1996

[7] Rutkowski, A., Wright, W.B., Potapczuk, M.G., *Numerical Study of Droplet Splashing and Re-Impingement*, AIAA-2003-0388

[8] Potapczuk, M.G., *Ice Mass Measurements: Implications for the Ice Accretion Process*, AIAA-200-0387

[9] Hedde, T., *Modélisation Tridimensionnelle des Dépôts de Givre sur les Voilures d'Aéronefs*, PhD Thesis, Université Blaise-Pascal, Clermont-Ferrand, 1992

[10] Ruff, G.A, Berkowitz, B.M., *Users Manual for the NASA Lewis Ice Accretion Prediction Code (LEWICE)*, NASA Contractor Report 185129, 1990

[11] Bourgault, Y., Habashi, W.G., Dompierre, J., Baruzzi, G.S., *A Finite Element Method Study of Eulerian Droplets Impingement Models*, Int. Journal for Numerical Methods in Fluids, 1999

[12] Bourgault, Y., Boutanios, Z., Habashi, W.G., *Three-Dimensional Eulerian Approach to Droplet Impingement Simulation Using FENSAP-ICE, Part 1: Model, Algorithm and Validation*, Journal of Aircraft, Vol. 37, No. 1, 2000

[13] Morency, F., Beaugendre, H., Habashi, W.G., *FENSAP-ICE: A Navier-Stokes Eulerian Droplet Impingement Approach for High-Lift Devices*, CASI Conference, 2001

[14] Morency, F., Beaugendre, H., Baruzzi, G.S., Habashi, W.G., *FENSAP-ICE: A Comprehensive 3D Simulation System for In-Flight Icing*, AIAA-2001-2566

[15] Beaugendre, H., Morency, F., Habashi, W.G., FENSAP-ICE's Three-Dimensional In-Flight Ice Accretion Module: ICE3D, Journal of Aircraft, Vol. 40, No. 3, 2003

[16] Baruzzi, G.S., Habashi, W.G., Guèvremont, G., Hafez, M.M., *A Second Order Finite Element Method for the Solution of the Transonic Euler and Navier-Stokes Equations*, International Journal for Numerical Methods in Fluids, Vol. 20, pp. 671-693, 1995

[17] Crowe, C., *Review – Numerical Models for Dilute Gas-Particle Flows*, Trans. ASME Journal of Fluids Engineering, Vol. 104, pp. 297-303, 1982

[18] Durst, F., Milojevic, D., Schönung, B., *Eulerian and Lagrangian Predictions of Particulate Two-Phase Flows: A Numerical Study*, Applied Mathematical Modeling, Vol. 8, pp. 101-115, 1984

[19] Clift, R., Grace, J.R., Weber, M.E., *Bubbles, Drops and Particles*, Academic Press, New York, 1978

[20] Pilch, M., Erdman, C.A., *Use of Breakup Time Data and Velocity History Data to Predict the Maximum Size of Stable Fragments for Acceleration-Induced Breakup of a Liquid Drop*, International Journal of Multiphase Flow, Vol.13, No. 6, pp. 741-757, 1987

[21] Lodej, B., *Étude et Implémentation des Phénomènes d'Éclatement de Gouttes d'Eau dans un Écoulement Diphasique*, Rapport de Stage de Fin d' Étude, Institut Scientifique Polytechnique Galilée, Paris, 2003

[22] Messinger, B.L., *Equilibrium Temperature of an Unheated Icing Surface as a Function of Air Speed*, Journal of the Aeronautical Sciences, Vol. 20, No. 1, pp. 29-42, 1953

[23] Boulahya, F., *Implementation of Splashing Models of Supercooled Large Droplets in DROP3D*, Institut des Sciences et Techniques de l'Ingénieur de Lyon, 2004

[24] Khan, A.R., Richardson, J.F., *The Resistance to Motion of a Solid Sphere in a Fluid*, Chemical Engineering Communication, Vol. 62, pp. 135-150, 1987

[25] Rein, M., *Phenomena of Liquid Drop Impact on Solid and Liquid Surfaces*, Fluid Dynamics Research, Vol. 12, pp. 61-93, 1993

[26] Bai, C., Gosman, A.D., *Development of Methodology for Spray Impingement Simulation*, SAE Technical Report 950283, 1995

[27] Bussman, M., Chandra, S., Mostaghimi, J., *Modeling the Splash of a Droplet Impacting a Solid Surface*, Physics of Fluids, Vol. 12., p. 3121, 2000

[28] Jayaratne, O.W., Mason, B.J., *The Coalescence and Bouncing of Water Drops at an Air/Water Interface*, Proceedings of the Royal Society of London, Vol. A280, pp. 545-565, 1964

[29] Naber, J.D., Reitz, R.D., Modeling Engine/Spray Wall Impingement, SAE Technical Report 880107, 1988

[30] Wang, M, Watkins, A.P., *Numerical Modeling of Diesel Spray Wall Impaction Phenomena*, International Journal of Heat and Fluid Flow, Vol. 14. No. 3, pp. 301-312, 1993

[31] Mundo, C., Sommerfeld., M., Tropea, C., *Droplet-Wall Collisions: Experimental Studies of the Deformation and Breakup Process*, International Journal of Multiphase Flow, Vol. 21, No.2, pp. 151-73, 1995

[32] Mundo, C., Tropea, C., Sommerfeld., M., *Numerical and Experimental Investigation of Spray Characteristics in the Vicinity of a Rigid Wall*, Experimental Thermal and Fluid Science, Vol. 15, pp. 228-237, 1997

[33] Mundo, C., Sommerfeld., M., Tropea, C., *On the Modeling of Liquid Sprays Impinging on Surfaces*, Atomization and Sprays, Vol. 8, pp. 625-652, 1998

[34] Stanton, D., Rutland, C., *Modeling Fuel Film Formation and Wall Interaction in Diesel Engines*, SAE Technical Report 960628, 1996

[35] Yarin, A.L., Weiss, D.A., *Impact of Drops on Solid Surfaces: Self-Similar Capillary Waves and Splashing as a New Type of Kinematic Discontinuity*, Journal of Fluid Mechanics, Vol. 283, pp. 141-173, 1995

[36] Mao, T., Kuhn, D.C.S., Tran, H., *Spread and Rebound of Liquid Droplets Upon Impact on Flat Surfaces*, AIChE Journal, Vol. 43, No. 9, pp. 2169-2179, 1997

[37] Schmehl, R., Rosskamp, H., Willmann, M., Wittig, S., *CFD Analysis of Spray Propagation and Evaporation Including Wall Film Formation and Spray/Film Interactions*, 8th International Conference on Liquid Atomization and Spray Systems, Pasadena, USA, 2000

[38] Samenfink, W., Elsässer A., Dullenkopf, K., Wittig, S., *Droplet Interaction With Shear-Driven Liquid Films: Analysis of Deposition and Secondary Droplet Characteristics*, International Journal of Heat and Fluid Flow, Vol. 20, pp. 462-469, 1999

[39] Trujillo, M.F., Mathews, W.S., Lee, C.F., Peters, J.E., Modeling and Experiment of Impingement and Atomization of a Liquid Spray on a Wall, International Journal of Engine Research, Vol. 1, No. 1, pp. 87-105, 2000

[40] Stow, C.D., Hadfield, M.G., *An Experimental Investigation of Fluid Flow Resulting From the Impact of a Water Drop With an Unyielding Dry Surface*, Proceedings of the Royal Society of London, Vol. A373, pp. 419-441, 1981

[41] Stow. C.D., Stainer, R.D., *The Physical Products of a Splashing Water Drop,* Journal of the Meteorological Society of Japan, Vol. 55, No. 5, pp. 518-532, 1977

[42] Wright, W.B., Potapczuk, M.G., *Semi-Empirical Modeling of SLD Physics*, 42nd AIAA Aerospace Sciences Meeting and Exhibit, Reno, Nevada, 2004

[43] Okumura, K., Chevy, F., Richard, D., Quéré, D., Clanet, C., *Water Spring: A Model for Bouncing Drops*, Europhysics Letters, Vol. 62, No.2, pp. 237-243, 2003

[44] Papadakis, M., Rachman, A., Wong, S.C., Yeong, H.W., Hung, K.E., Bidwell, C.S., *Water Impingement Experiments on a NACA 23012 Airfoil with Simulated Glaze Ice Shapes*, AIAA-2004-0565

[45] Papadakis, M., Hung, E.K., Vu, G.T., Yeong, H.W., Bidwell, C.S., Breer, M.D., Bencic, T.J., *Experimental Investigation of Water Droplet Impingement on Airfoils, Finite Wings and an S-Duct Engine Inlet*, NASA/TM-2002-211700